



National Library
of Canada

Bibliothèque nationale
du Canada

Acquisitions and
Bibliographic Services Branch

Direction des acquisitions et
des services bibliographiques

395 Wellington Street
Ottawa, Ontario
K1A 0N4

395, rue Wellington
Ottawa (Ontario)
K1A 0N4

Your file *Votre référence*

Our file *Notre référence*

NOTICE

The quality of this microform is heavily dependent upon the quality of the original thesis submitted for microfilming. Every effort has been made to ensure the highest quality of reproduction possible.

If pages are missing, contact the university which granted the degree.

Some pages may have indistinct print especially if the original pages were typed with a poor typewriter ribbon or if the university sent us an inferior photocopy.

Reproduction in full or in part of this microform is governed by the Canadian Copyright Act, R.S.C. 1970, c. C-30, and subsequent amendments.

AVIS

La qualité de cette microforme dépend grandement de la qualité de la thèse soumise au microfilmage. Nous avons tout fait pour assurer une qualité supérieure de reproduction.

S'il manque des pages, veuillez communiquer avec l'université qui a conféré le grade.

La qualité d'impression de certaines pages peut laisser à désirer, surtout si les pages originales ont été dactylographiées à l'aide d'un ruban usé ou si l'université nous a fait parvenir une photocopie de qualité inférieure.

La reproduction, même partielle, de cette microforme est soumise à la Loi canadienne sur le droit d'auteur, SRC 1970, c. C-30, et ses amendements subséquents.

Canada

**INFLUENCE OF UPSTREAM
TURBULENCE ON DISCRETE-HOLE FILM
COOLING OF A MODEL BLADE IN
CONFINED CROSS FLOW**

by

Nicholas Stathopoulos

A Thesis Submitted to the Faculty of Graduate Studies and Research
in Partial Fulfillment of the Requirements for a Degree of
Master of Engineering

Department of Mechanical Engineering
McGill University
700 Sherbrooke St. W., Montreal, Quebec, Canada

© N. Stathopoulos, Montreal, Canada, 1994



National Library
of Canada

Acquisitions and
Bibliographic Services Branch

395 Wellington Street
Ottawa, Ontario
K1A 0N4

Bibliothèque nationale
du Canada

Direction des acquisitions et
des services bibliographiques

395, rue Wellington
Ottawa (Ontario)
K1A 0N4

Your file *Votre référence*

Our file *Notre référence*

THE AUTHOR HAS GRANTED AN IRREVOCABLE NON-EXCLUSIVE LICENCE ALLOWING THE NATIONAL LIBRARY OF CANADA TO REPRODUCE, LOAN, DISTRIBUTE OR SELL COPIES OF HIS/HER THESIS BY ANY MEANS AND IN ANY FORM OR FORMAT, MAKING THIS THESIS AVAILABLE TO INTERESTED PERSONS.

L'AUTEUR A ACCORDE UNE LICENCE IRREVOCABLE ET NON EXCLUSIVE PERMETTANT A LA BIBLIOTHEQUE NATIONALE DU CANADA DE REPRODUIRE, PRETER, DISTRIBUER OU VENDRE DES COPIES DE SA THESE DE QUELQUE MANIERE ET SOUS QUELQUE FORME QUE CE SOIT POUR METTRE DES EXEMPLAIRES DE CETTE THESE A LA DISPOSITION DES PERSONNE INTERESSEES.

THE AUTHOR RETAINS OWNERSHIP OF THE COPYRIGHT IN HIS/HER THESIS. NEITHER THE THESIS NOR SUBSTANTIAL EXTRACTS FROM IT MAY BE PRINTED OR OTHERWISE REPRODUCED WITHOUT HIS/HER PERMISSION.

L'AUTEUR CONSERVE LA PROPRIETE DU DROIT D'AUTEUR QUI PROTEGE SA THESE. NI LA THESE NI DES EXTRAITS SUBSTANTIELS DE CELLE-CI NE DOIVENT ETRE IMPRIMES OU AUTREMENT REPRODUITS SANS SON AUTORISATION.

ISBN 0-315-99982-9

Canada

NICHOLAS STATHOPOULOS

**INFLUENCE OF UPSTREAM
TURBULENCE ON DISCRETE-HOLE FILM
COOLING OF A MODEL BLADE IN
CONFINED CROSS FLOW**

**M. Eng.
1994**

Abstract

An experimental investigation of the influence of upstream turbulence on discrete-hole film cooling of a model blade in confined cross flow is presented and discussed. A model blade and test section were designed and constructed. A system for constant-temperature hot-wire anemometry was implemented. A microcomputer-based data acquisition, control, and processing system was designed and implemented. The model blade was a blunt body with a semicircular leading edge, a flat after body, and a tapered trailing edge. Local heat transfer coefficients *without* injection of a secondary fluid were determined using a thin-film technique. In the film cooling studies, two rows of discrete injection holes at $\pm 30^\circ$ from the stagnation line were used. The injection tubes were oriented normal to the surface of the model blade and were coplanar with the primary flow velocity vector.

Nominal turbulence intensities of 0.7%, 9.8%, and 14.4% at a location 1.3 diameters upstream of the stagnation line on the semicircular leading edge of the model blade were investigated. The range of Reynolds number, based on the diameter of the semicircular leading edge and upstream velocity, was 23,000 to 75,000. In the discrete-hole film cooling studies, mass flux ratios in the range $0.6 < M < 2.0$ were considered. The heat transfer results are presented in terms of the distributions of local Nusselt number and a nondimensional temperature on the surface of the blade. The results of the film cooling studies are presented in terms of the distributions of the effectiveness.

Sommaire

Une recherche expérimentale de l'influence de la turbulence du gaz primaire sur l'efficacité de refroidissement à injection du gaz secondaire sur un modèle d'une lame est présentée et évaluée. Un modèle d'une lame et une section expérimentale ont été conçus et construits. Un système d'anémomètre à fil-chaud de température constante a été installé. Un système, branché sur l'ordinateur, pour l'acquisition et l'analyse des données et le contrôle de l'expérience a été conçu et construit. Le modèle d'une lame a une façade circulaire, un corps plat, et à l'extrémité, la surface supérieure rencontre la surface inférieure. Le coefficient local du transfert de chaleur *sans* injection du gaz secondaire a été déterminé en utilisant la technique mince-pellicule. Dans les études de l'efficacité du refroidissement à injection, deux rangées d'orifices à intervalles réguliers à $\pm 30^\circ$ de la ligne de stagnation ont été utilisées. Les tubes à injection sont perpendiculaires à la surface du modèle et sur le même plan que la direction du gaz primaire.

L'intensité nominale de la turbulence de 0.7%, 9.8%, et 14.4% à une distance de 1.3 diamètre de la ligne de stagnation du modèle a été étudiée. Le nombre de Reynolds, basé sur le diamètre du modèle et la vitesse du gaz primaire, a été entre 23,000 à 75,000. Dans l'étude de l'efficacité du refroidissement à injection, le ratio du flux des deux gaz dans la portée $0.6 < M < 2.0$ a été considéré. Les résultats de l'expérience de transfert de chaleur sont présentés en terme de distribution du nombre Nusselt local et de la température non-dimensionnée sur la surface du modèle. Le résultat de l'étude sur l'efficacité du refroidissement à injection est présenté en termes de l'efficacité adiabatique.

Acknowledgments

First and foremost, I would like to thank very much Prof. B.R. Baliga for his extraordinary support and guidance. I am especially grateful to him for encouraging my undergraduate research projects, which evolved into a desire to pursue graduate studies and this research project. Over the past six years, the discussions I had with him, and his dedication to research has given me an understanding, and appreciation of research and engineering, which contributed greatly to the enjoyable and rewarding experience I had at McGill University.

I would like to thank NSERC for the financial support I received. I obtained a Master's scholarship, without which, it would have been very difficult to obtain this degree.

I am very grateful to Prof. B.G. Newman for allowing me to use one of the wind tunnels in the Aerodynamics Laboratory to carry out the experiments.

The construction of the model blade, test section, and all the related experimental apparatus was only possible through the help of the Machine Tool Laboratory (M.T.L.), the Aerodynamics Machine Shop (A.M.S.), and the Undergraduate Machine Shop (U.M.S.). Specifically, I would like to personally thank Fernand Picard and Arthur Clément from M.T.L., for their precise and beautiful work; Steve Markhauser and Scott Manktelow from A.M.S. for their help in all the aspects of construction, which was usually on their own time, as well as for their help in less academic projects and conversations, all of which made school much more enjoyable; Jack Kelly, Gary, John, and Roy from U.M.S. for always been there to help in my machining attempts.

I would like to thank George Dedic and George Tewfik, of the Instrument Laboratory, for the support they provided with the electrical and electronic part of the experiment, as well as for their help in finding appropriate suppliers.

While at McGill, I have been very fortunate to work with a number of great people. With these fellow students, we created an excellent peer support environment, making academic life pleasant, productive, and rewarding. I would like to especially thank Simone Sebben for her help with the model and the *pink* insulation, and all those pleasant conversations, John Saabas for his support, especially with the hot wire anemometry, Michel Bernier for helping me with the equipment when I was first learning the ropes, and Nasarollah Munshi for always being there to give me a hand, and to talk about the experiments. To complete the group circle, there was also Daniel Rousse, Stéphane Cyr, Christian Masson, and Nabil Elkouh who also helped in various aspects of the research project, and academic life.

I am very grateful to my family, who supported my studies and contributed to my research work. I would like to thank my brother Pericles for his help with the installation of some heavy pieces of equipment, my sister Maria-Helen who helped with the photography of the experimental apparatus, and the preparation of this thesis, my brother Emmanuel who helped with moving of large pieces of equipment and some of the figures in this thesis, my cousin Niko for his help with the construction of the thermocouples, and to my mom for her continuous emotional support throughout my years at McGill University. Last but not least, I would like to thank my fiancée Kathie Petrakos for her moral support, in addition to helping me with the delicate task of replacing endless number of burnt heater films, the photography of the experiment, the installation of the model blade in the test section, and the preparation of this thesis.

Table of Contents

Abstract.....	i
Sommaire.....	ii
Acknowledgments.....	iii
Table of Contents.....	v
List of Figures.....	viii
List of Tables.....	xi
Nomenclature.....	xii
CHAPTER 1.....	1
INTRODUCTION.....	1
1.1 Goals and Motivation of the Thesis.....	1
1.2 Overview of the Experimental Apparatus and Instrumentation.....	2
1.3 Synopsis of Related Investigations.....	4
1.3.1 Opening Remarks.....	4
1.3.2 Jets in Cross Flow.....	6
1.3.3 Overview of Film Cooling of Gas turbine Blades.....	6
1.3.4 Discrete-Hole Film Cooling of a Blunt Body with Semi- Circular Leading Edge.....	13
1.4 Overview of the Thesis.....	17
CHAPTER 2.....	18
THEORETICAL CONSIDERATIONS.....	18
2.1 Adiabatic Wall Temperature and Film Cooling Effectiveness.....	18
2.2 Experimental Determination of Film Cooling Effectiveness.....	20
2.3 Experimental Determination of the Heat Transfer Coefficient on the External Surface of the Model Blade without Secondary Flow.....	24

2.4 Determination of Tangential Heat Conduction within the Wall of the Model Blade in Film-Cooling Studies	27
2.5 Constant-Temperature Hot Wire Anemometry	30
CHAPTER 3	33
EXPERIMENTAL APPARATUS AND PROCEDURES	33
3.1 Test Section and Model Blade	33
3.2 Systems for Primary and Secondary Air Flow	35
3.3 Grids for Generating Turbulence	37
3.4 Data Acquisition, Instrumentation, and Control	37
3.4.1 Data Acquisition	37
3.4.2 Temperature Measurement	38
3.4.3 Differential Pressure Measurements	39
3.4.4 Barometric Pressure	40
3.4.5 Air Velocity and Flow Rate Measurements	40
3.4.6 Turbulence Measurements	41
3.5 Calibration Procedures	43
3.5.1 Thermocouple Calibration	43
3.5.2 Barocel Calibration	44
3.5.3 Hot Wire Calibration	45
3.5.4 Electronic Barometer Calibration	47
3.6 Computer Control	47
3.6.1 Wind Tunnel Velocity Control	48
3.6.2 Heating Film Control	49
3.7 Experimental Procedure	49
3.7.1 Procedure for the Investigation of Primary Flow Turbulence Intensity	50
3.7.2 Procedure for the Heat Transfer Experiment	52

3.7.3 Experimental Procedure for the Investigation of Film Cooling Effectiveness	53
CHAPTER 4	55
RESULTS AND DISCUSSION	55
4.1 Turbulence Intensity of the Primary Air Flow	55
4.2 Local Heat Transfer Coefficient on the Surface of the Model Blade Without Secondary Flow	58
4.3 Film Cooling Effectiveness Results	61
CHAPTER 5	67
CONCLUSIONS AND RECOMMENDATIONS	67
5.1 Contributions of this work	67
5.2 Suggestions for Improvements and Extensions	70
REFERENCES:	R.1
APPENDIX A	A.1
Hot Wire Data Reduction Procedure	A.1
APPENDIX B	B.1
Error Analysis	B.1
FIGURES	F.1
TABLES	T.1

List of Figures

- Fig. 1: Schematic illustration of the model blade: leading edge diameter is $D = 126.0$ mm; after body length is 381 mm; trailing edge length is 355 mm; and the width is 762 mm
- Fig. 2: Cross-sectional view of the test section with the model blade mounted inside: width of model and test section is 762 mm
- Fig. 3: Schematic illustration of the blower cascade wind tunnel
- Fig. 4: Square-bar pattern for turbulence generating grid
- Fig. 5: Local energy balance on the surface of the model blade in film cooling studies
- Fig. 6: Local conduction balance for the film cooling experiment
- Fig. 7: Quasi one-dimensional control volume for the heat transfer data processing
- Fig. 8: Thermocouple layout on the surface of the model and the triangular element configuration for the film cooling data processing
- Fig. 9: Details of triangular elements and a control volume surrounding a typical node
- Fig. 10: Details of X-wire probe and notation for the turbulence intensity data processing
- Fig. 11: Experimental apparatus block diagram
- Fig. 12: Details of the differential pressure measuring apparatus
- Fig. 13: Variation of turbulence intensity $\left(= \left\{ (u'^2 + v'^2 + w'^2) / U^2 \right\}^{1/2} \right)$ with nondimensional distance (X/D) from the location of the turbulence generating grid, along a line given by $Z/D=0$ and $Y/D=0$
- Fig. 14: Variation of turbulence intensity $\left(= \left\{ (u'^2 + v'^2 + w'^2) / U^2 \right\}^{1/2} \right)$ with nondimensional distance (X/D) from the location of the turbulence generating grid, along a line given by $Z/D=0$ and $Y/D=1.7$

- Fig. 15: Variation of mean velocity with nondimensional distance (X/D) from the location of the turbulence generating grid, along a line given by $Z/D=0$ and $Y/D=0$
- Fig. 16: Variation of mean velocity with nondimensional distance (X/D) from the location of the turbulence generating grid, along a line given by $Z/D=0$ and $Y/D=1.7$
- Fig. 17: Variation of turbulence intensity in the free stream direction only $\left(= \{u'^2/U^2\}^{1/2} \right)$ with nondimensional distance (X/D) from the location of the turbulence generating grid, along a line given by $Z/D=0$ and $Y/D=0$
- Fig. 18: Variation of turbulence intensity in the free stream direction only $\left(= \{u'^2/U^2\}^{1/2} \right)$ with nondimensional distance (X/D) from the location of the turbulence generating grid, along a line given by $Z/D=0$ and $Y/D=1.7$
- Fig. 19: Normalized local conduction and radiation heat transfer versus nondimensional distance (x/D) from the stagnation line on the model: $Re=51,000$; No Grid
- Fig. 20: Local Nusselt number versus nondimensional distance along the model: No grid
- Fig. 21: Local Nusselt number versus nondimensional distance along the model: Grid 1
- Fig. 22: Local Nusselt number versus nondimensional distance along the model: Grid 2
- Fig. 23: Comparison of local Nusselt numbers for low (No grid), medium (Grid 1), and high turbulence (Grid 2) intensities at a nominal Reynolds number of 54,000
- Fig. 24: Comparison of local Nusselt numbers at $Re=51,000$ and at low turbulence (No grid) at two different heater power levels
- Fig. 25: Film cooling effectiveness correction contributions of conduction and radiation, at nodes along line D: $Re=52,100$; $M=0.96$; No Grid
- Fig. 26: Local film cooling effectiveness versus nondimensional distance along line D at different Reynolds numbers: No grid

- Fig. 27: Local film cooling effectiveness versus nondimensional distance along line D at different Reynolds numbers: Grid 1
- Fig. 28: Local film cooling effectiveness versus nondimensional distance along line D at different Reynolds numbers: Grid 2
- Fig. 29: Comparison of local film cooling effectiveness for the low (No grid) and high (Grid 2) turbulence intensities at a nominal Reynolds number of 53,500 and mass flux ratio of 1.27
- Fig. 30: Local film cooling effectiveness versus nondimensional distance along line D at different mass flux ratios: $Re=52,100$; No grid
- Fig. 31: Local film cooling effectiveness versus nondimensional distance along line D at different mass flux ratios: $Re=39,200$; Grid 2
- Fig. 32: Comparison of film cooling effectiveness for Cases 16 and 17: $Re=39,200$; $M=0.65$; Grid 2

List of Tables

- Table 1: Local nondimensional temperatures and Nusselt numbers on the external surface of the model blade: No grid
- Table 2: Local nondimensional temperatures and Nusselt numbers on the external surface of the model blade: Grid 1
- Table 3: Local nondimensional temperatures and Nusselt numbers on the external surface of the model blade: Grid 2
- Table 4: Local film cooling effectiveness on the external surface of the model blade: Cases 1 to 4
- Table 5: Local film cooling effectiveness on the external surface of the model blade: Cases 5 to 8
- Table 6: Local film cooling effectiveness on the external surface of the model blade: Cases 9 to 12
- Table 7: Local film cooling effectiveness on the external surface of the model blade: Cases 13 to 15
- Table 8: Local film cooling effectiveness on the external surface of the model blade: Cases 16 to 19
- Table 9: Local film cooling effectiveness on the external surface of the model blade: Cases 20 to 23
- Table 10: Local film cooling effectiveness on the external surface of the model blade: Cases 24 to 27
- Table 11: Local film cooling effectiveness on the external surface of the model blade: Cases 28 to 31
- Table 12: Local film cooling effectiveness on the external surface of the model blade: Cases 32 to 34

Nomenclature

Symbol	Description
A, B, C	constant coefficients of temperature distribution equation
A_H	surface area of the film heater
A_p	surface area of a control volume
ds	elemental length
D	diameter of the leading edge of the model blade
DET	elemental determinant value
h	local convective heat transfer coefficient
h_p	convective heat transfer coefficient of the plenum
I_H	current applied to the heater film
k	longitudinal effective velocity factor for the hot wire
k_a	thermal conductivity of acrylic
k_i	thermal conductivity coefficient of the interior insulation
M	mass flux ratio
n	number of data points
\bar{n}	unit normal vector
Nu	Nusselt number
q''_H	local heat flux generated by the heater film
q_{cond}	rate of local conduction heat transfer
q''_{cond}	local conduction heat flux
q_{conv}	rate of local convective heat transfer
q''_{conv}	local convective heat flux
q_{rad}	rate of local radiation heat transfer
q''_{rad}	radiation heat flux
R	resistance per square of the heater film

Re	Reynolds number
T	temperature
T_{∞}	temperature of the primary air flow upstream of the model
T_{aw}	adiabatic surface wall temperature
T_{ref}	reference temperature
T_s	temperature of secondary air flow
T_w	surface wall temperature
TI	turbulence intensity
u	air velocity component in the streamwise direction
u'	square root of the mean streamwise fluctuation velocity squared
\bar{u}	mean air velocity component in the streamwise direction
U	instantaneous velocity of primary air flow
\bar{U}	mean velocity of the primary air flow
U_{e1}	effective velocity of primary air flow upon hot wire #1
U_{e2}	effective velocity of primary air flow upon hot wire #2
v	air velocity component in the Y direction
v'	square root of the mean fluctuation velocity squared, Y direction
V_H	voltage applied to the heater film
x, y, z	coordinate system along the surface of the model blade
X, Y, Z	coordinate system in the test section
w'	square root of the mean fluctuation velocity squared, Z direction

Greek Symbols

α	angle between the air flow and the normal of hot wire #1
δ_o	thickness of the acrylic surface of the model
δ_i	thickness of the insulation below the surface of the model
δx	distance between adjacent nodes in the streamwise direction
ϵ	emissivity

θ	angle between hot wire #1 and the air flow direction
η	adiabatic film cooling effectiveness
η'	measured film cooling effectiveness
σ	Stefan-Boltzmann constant
ϕ	angle between the two hot wires
Φ	nondimensional local surface temperature

subscripts

a	acrylic
ABS	absolute temperature in Kelvin
aw	adiabatic wall
e1,e2	effective for wire #1 and wire #2
e,w	coefficient value at the control volume boundary
E,P,W	coefficient value at the nodal point
H	heater film
HT TRF	heat transfer experiment
i	insulation
11, 12	direction along Wire #1 and Wire #2 of the hot wire probe
n1, n2	normal direction to Wire #1 and Wire #2 of the hot wire probe
N, T	direction normal and along the surface of model blade
p	plenum
s	secondary flow
w	wall surface of the model
1,2,3	coefficient value at element's nodes
∞	primary flow

Chapter 1

INTRODUCTION

1.1 Goals and Motivation of the Thesis

High thermal efficiency, high power to weight ratio, and compact size are all very desirable objectives in the design of modern gas turbine engines. In order to achieve these objectives, it is necessary to operate the engines at high temperatures, and this, in turn, requires innovative cooling schemes for the turbine blades. Current strategies for turbine blade cooling include film cooling and augmented internal cooling. Detailed discussions of these techniques and related issues are available in the works of Goldstein (1971) and Mayle and Anderson (1991). In practice, the problem of cooling a gas turbine blade involves many parameters [Goldstein, 1971], and suitable combinations of experimental and numerical methods are required for the design of appropriate cooling schemes.

One of the parameters that has a significant influence on the heat transfer from the turbine blades is upstream turbulence intensity [Goldstein, 1971; Kikkawa and Hayashida, 1987; Mehendale and Han, 1992a, 1992b; Mick and Mayle, 1988]. An experimental investigation of the influence of upstream turbulence on discrete-hole film cooling of a model blade in confined cross flow is presented and discussed in this thesis. This work complements and extends the studies of Simonich and Bradshaw (1978), Hancock and Bradshaw (1983), O'Brien and VanFossen (1986), Han and Young (1988), Mick and Mayle (1988), Kikkawa and Hayashida (1987), Mehendale *et al.* (1991), Ou *et al.* (1992b), and Ou and Han (1992a).

The objectives of this thesis are the following: (i) design and construction of a test section and a model blade; (ii) implementation of available hot wire techniques, for mean velocity and turbulence measurements, and a thin-film technique, for local heat transfer measurements, along with related instrumentation; (iii) design and implementation of a microcomputer-based system for data acquisition, control, and processing; and (iv) investigation of the influence of upstream turbulence on heat transfer from the model blade without injection, and on film cooling effectiveness with discrete-hole injection, for several combinations of cross flow Reynolds number and blowing ratios [Goldstein, 1971]. The overall goals are to develop an experimental facility for the investigation of film cooling, enhance the understanding of the physics involved in such experiments, and obtain data that could be used to test the predictions of numerical models.

The work reported in this thesis is a direct extension of an experimental investigation by Saabas (1991) of the fluid dynamics of discrete-hole injection from a model blade in confined cross flow. The work of Saabas (1991) and this work are a part of on-going experimental and computational investigations of discrete-hole film cooling of gas turbine blades, being carried out in the Heat Transfer and Aerodynamics Laboratories of the Department of Mechanical Engineering at McGill University. These investigations were initiated in 1988 with financial support from Pratt and Whitney Canada.

1.2 Overview of the Experimental Apparatus and Instrumentation

A synopsis of the experimental apparatus, instrumentation, and procedures used in this study are presented in this section. Detailed descriptions of these topics are provided in Chapter 3. The model blade used in this study is a blunt body with a semicircular leading edge and flat after body, similar to those used by Bellows and Mayle (1986), Mehendale

et al. (1991), and Saabas (1991). A schematic illustration of this model blade is given in Fig. 1. The discrete injection holes in this model blade can be closed, if desired, by the use of specially designed plugs. Thus, experiments can be carried out with and without discrete-hole injection. The model blade has three rows of injection holes, one row along the stagnation line, another row located along the line at 30° from the stagnation line, and the last row of holes located along the line at -30° from the stagnation line. In this work, experiments were conducted with no injection (all holes plugged), and with simultaneous injection from the holes along the $\pm 30^\circ$ lines. Injection from the holes along the stagnation line was not investigated.

The model blade was made of 12.7 mm ($\frac{1}{2}$ inch) thick Plexiglas. The diameter of the semicircular leading-edge was 127 mm (5 inches) and the width of blade was 762 mm (30 inches). The diameter of each injection hole was 13.2 mm (0.52 inches). Each hole was fed by a straight injection tube of length 38 mm (1.5 inches), with the axis of the injection tube oriented normally to the surface of the blade.

The model blade was mounted in a test section attached to a blower cascade wind tunnel available in the Aerodynamics Laboratory at McGill University. A schematic illustration of this wind tunnel is given in Fig. 3. A cross-sectional view of the test section with the model blade mounted inside is given in Fig. 2, along with some key dimensions. The blockage due to the model blade in the test section is 29.4%.

The model blade was covered with a thin, electrically conducting film, made by vapor deposition of indium/tin oxide on a polymer base. Copper electrodes were attached to this film at the ends of the blade adjacent to the walls of the test section. The indium/tin oxide film used in this study was manufactured by Courtaulds Performance Films, in Canoga Park, California, U.S.A. In the heat transfer experiments, this film was heated

using a DC power supply, and the local surface temperatures were measured using chromel-constantan thermocouples, calibrated to $\pm 0.05^\circ\text{C}$ accuracy. This thin-film technique for the measurement of local heat transfer coefficients has been used in earlier investigations by Baughn *et al.* (1985,1986), Hippensteele *et al.* (1985), Neill (1989), and Bernier and Baliga (1992).

The blower cascade wind tunnel produced turbulence intensities in the range of 0.6% to 0.9% over the range of cross flow velocities considered in this work. Higher upstream turbulence was obtained by using two different grids, each of a pattern similar to that shown in Fig. 4. The first grid, Grid #1, was made with bars of 6.5 mm square cross section, separated by 22.2 mm, The second grid, Grid #2, consisted of bars of 11.0 mm square cross section, separated by 37.6 mm. These grids were designed using recommendations of Baines and Peterson (1951) and Mehendale *et al.* (1991).

Velocity and turbulence data were measured using constant-temperature anemometry, with a cross-wire probe. Procedures discussed by Bradshaw (1971) and Champagne *et al.* (1967a, 1967b) were used to process the hot wire signals.

Microcomputer-based data acquisition, control, and processing techniques were extensively used in this work. Details are provided in Chapter 3.

1.3 Synopsis of Related Investigations

1.3.1 Opening Remarks

Some useful references pertaining to the subject of heat transfer, turbulence, hot wire anemometry, pitot and static tubes, liquid crystals, and local heat flux measurements are given in this subsection.

There are numerous books devoted to the subject of heat transfer. Excellent examples include the books published by Eckert and Drake (1972), Kays and Crawford (1993), Incropera and Dewitt(1985), Seigel and Howell(1981), and Modest (1993). Expert reviews of specific topics in heat transfer are available in the *Handbook of Heat Transfer*, edited by Rohsenow and Hartnett (1973), and the *Advances in Heat Transfer*, Volumes 1-24, edited by Hartnett and Irvine (1964-94). The subject of overall and local convective heat transfer from cylinders in cross flow has been discussed in detail by Mujumdar (1971) and Zhukaukas (1972). Heat transfer from spheres in cross flow has been discussed in papers by MacAdam (1954), and Raithby and Eckert (1968).

The physics and mathematical models of turbulence are discussed in the works of Hinze (1975), Tennekes and Lumley (1972), Schlichting (1987), Batchelor (1974), Launder and Spalding (1974), and Bradshaw *et al.* (1963, 1971). The theory, calibration, and uses of hot wire anemometry for the measurement of laminar and turbulent flows are discussed in detail in the works of Bradshaw *et al.* (1963, 1971), Perry (1982), Lomas (1986), Champagne *et al.* (1967a, 1967b), John and Schobeiri (1993), Lofdahl (1985), and in a monograph published by TSI systems Inc. (1993). Issues pertaining to grid-generated turbulence are discussed in detail by Baines and Peterson (1951), and Mehendale *et al.* (1991).

Pitot and static tube techniques for measuring fluid velocity and flow rate are described in the works of Ower and Pankhurst (1966) and Shaw (1960).

The theory, calibration, and practical applications of thermocouples are discussed in books by Holman (1986), Eckert and Goldstein (1976), and in a monograph published by Hewlett Packard (1993). Liquid crystal techniques for temperature field visualization are

discussed in the works of Hippensteele *et al.* (1985), Camci *et al.* (1993) and Dini (1991). Techniques for measuring local heat flux on surfaces have been discussed by Ferguson (1964), Simonich and Moffat (1982, 1984), and Baughn *et al.* (1985, 1986). Further discussion of these techniques is available in the M. Eng. thesis of Neill (1989).

1.3.2 Jets in Cross Flow

Jets in cross flow have many engineering applications. Some examples of such applications include film cooling of gas turbine blades, jets in combustors, effluent discharge into the atmosphere, and lifting jets for V/STOL aircraft. There are literally hundreds of papers on this subject in the published literature. In this subsection, only a few relevant papers will be reviewed. Keffer and Baines (1963) have investigated the interaction of a round turbulent jet entering a cross flow with no boundary layer. Wygnanski and Newman (1968) discussed the reattachment of an inclined two-dimensional slot jet to a flat surface with cross flow. Gartshore and Newman (1969) discussed the fluid dynamics of a jet in an arbitrary pressure gradient. Abramovich (1963), and Chassaing *et al.* (1974) have studied the physical characteristics of a strong jet issuing into a uniform cross stream. Investigations of jets in cross flow at low mass flux ratios have been carried out by Crabb *et al.* (1981), and Andreopoulos and Rodi (1984). Further discussion of these papers is available in the Ph.D. thesis of Saabas (1991). More recently, the works of Lee *et al.* (1994), Honami *et al.* (1994), and Salcudean *et al.* (1994) further investigate the flow dynamics, heat transfer characteristics, and effectiveness of the injected jet in film cooling schemes.

1.3.3 Overview of Film Cooling of Gas turbine Blades

In the published literature, there are numerous papers that deal with the subject of film cooling of gas turbine blades. Detailed discussions of film cooling and augmented internal cooling strategies are available in the works of Goldstein (1971), and Mayle *et al.* (1976). The state-of-the-art with regard to turbulence models that are applicable to fluid

flow and heat transfer in gas turbines has been reviewed by Launder (1988), and Hanjalic (1994). An extensive survey of the papers relevant to film cooling of gas turbine blades is outside the scope of this thesis, and it is certainly not the objective of this synopsis. In this subsection, only some of the key papers dealing with topics that are pertinent to the film cooling of gas turbine blades will be briefly reviewed. In the next subsection, some of the papers that are *directly* related or relevant to the work reported in this thesis will be surveyed.

Paxson and Mayle (1988) investigated the influence of the main stream thermal boundary layer on film cooling of a flat surface. The experiment involved injecting a secondary flow at a higher temperature than that of the primary flow, parallel to the wall and the main stream flow. The mass flux ratio was maintained constant at 0.7. Heat transfer results were presented in the form of film cooling effectiveness and temperature profiles. The study concluded that the thermal boundary layer affects the effectiveness significantly. The theoretical model, however, presented a few difficulties, since the ratio of thermal to velocity boundary layer had to be known, as well as the effectiveness without a boundary layer.

In exploring the characteristics of film cooling, the study of jets injected from a flat surface into the main stream flow is an important step. One such study, by Alekseyev and Zelengur(1986), involved the injection of a single jet into the primary airflow, while varying the mass flux ratio from 0.1 to 1.5, and the inclination of the injection tube from 30° to 90°, both in the main flow direction and perpendicular to it. The results indicate that for the range of parameters investigated, a larger mass flux ratio improves the film cooling effectiveness, however, the more interesting result is the variation of effectiveness with angle of the injection tube. As this angle decreased with respect to the flow direction, the film cooling effectiveness increased. However, as the angle with

respect to a line perpendicular to the flow direction decreased so did the film cooling effectiveness until about 50° , below which it became increasingly effective. The authors explain this by noting that as this angle deviates from 90° , the jet loses its stability and acquires a swirl, which mixes the jet flow more quickly with the main stream flow. At values of this angle smaller than 50° , this swirl is not predominant so the efficiency starts increasing again.

The study by Foster and Lampard (1980) employs a row of injection holes and uses a mass transfer technique to determine the film cooling effectiveness. Their investigation indicated that the most efficient angle of the injection tubes to the main flow direction, with respect to film cooling effectiveness, increased as the mass flux ratio increased. The paper published by Jabbari and Goldstein (1977) studied the effect of two rows of injection holes on film cooling effectiveness, which was determined using local temperature measurements on the surface of the plate near the injection hole. Among the conclusions discussed in the paper are that decreasing injection angle increases the film cooling effectiveness, and increasing the mass flux ratio increases the cooling effectiveness until a maximum after which the effectiveness decreased, especially around the jet hole. Another investigation of jets on a flat surface by Kadotani and Goldstein (1979) studied the effect of turbulence on film cooling effectiveness. That study concluded that the main stream turbulence affects the film cooling effectiveness through its influence on four different aspects of the flow: the boundary layer thickness; the mixing of the main stream flow with the jet flow; the shape of the jet flow due to vortex formation; and the penetration height of the jet. Each of these factors affects the effectiveness to a different degree, depending on the mass flux ratio.

Surface curvature can have a significant influence on film cooling effectiveness. The work of Schwarz, Goldstein, and Eckert (1991) discusses the effect of surface curvature

and of mass flux ratio on heat transfer values. The mass transfer analogy was used to determine the film cooling effectiveness. Their investigation concluded that the tangential momentum of the jets reduces the effectiveness on convex surfaces and improves the effectiveness on concave surfaces; an increase in normal momentum of the jet tends to decrease the effectiveness, regardless of the curvature of the surface; the mass added to the main stream tends to increase the film cooling effectiveness for any curvature; the instabilities in the flow over concave surfaces produce a more evenly distributed film cooling effectiveness; and the cross-stream pressure gradient tends to move the film cooling jets into a convex surface and away from a concave surface.

Kasagi *et al.* (1987, 1989) extensively investigated film cooling on curved walls. To measure the heat transfer data, temperature sensitive liquid crystals were utilized. The conclusions drawn from their investigation was that the film cooling effectiveness on a convex wall is higher than that on a flat wall, and the opposite is true for a concave wall; the spanwise average effectiveness increases along a convex surface, while on a concave surface, it remains approximately constant; and the sensitivity of the film cooling effectiveness is more pronounced on the convex surface than on the concave surface.

Similar work by Schwarz and Goldstein (1989) concluded that the film cooling effectiveness increases on the concave surface until the injected air flow separates from the surface. The paper also concludes that the tangential momentum of the jet is beneficial to the film cooling effectiveness, whereas the normal momentum promotes flow separation. Furthermore, the unstable flow on the concave surface promotes lateral mixing and, therefore, produces a more even distribution of the film cooling effectiveness.

Mayle *et al.* (1976) have also studied the effect of surface curvature on film cooling effectiveness. They used a slot for the injection of the secondary air and thermocouples

to measure the temperatures necessary to determine the film cooling effectiveness. The findings of this study were that convex curvature increased the effectiveness whereas concave curvature was detrimental. This was explained by the growth of the shear and thermal boundary layers along the surface.

Another paper on the effect of surface curvature on heat transfer is by Thomann (1968). The interesting aspect of this study is that the tests were done in the supersonic regime, at Mach 2.5. The data is shown in the form of Stanton number distributions for four different configurations, and the result show that a concave wall increases the heat transfer.

Some studies have employed a cylinder with the axis perpendicular to the flow, and with injection holes on the surfaces. Such a study was done by Wadia and Nealy (1988) with the injection holes at 20, 30, 45 and 90 degrees from the stagnation line, and with the main stream Reynolds number varying from 35,000 to 90,000. The film cooling jet was heated using a 20 kW heater, and thermocouples were placed on the surface of the stainless steel cylinder. Typical gas temperatures surpassed 500°C, and the surface to gas temperature ratio was in the range of 0.6 to 0.8. The observations of this experiment were that the effectiveness decreased slightly with the increase of free-stream Mach number, and the inverse occurred with the leading-edge Reynolds number; and effectiveness exhibited a significant dependence on the spanwise inclination angle of the injection tube.

To faithfully reproduce the geometry of the turbine section in a jet engine, certain groups of researchers have used realistic models of turbine blades, and placed them in the wind tunnel in cascade formations. Ito, Goldstein, and Eckert (1978) used the mass-heat transfer analogy to study film cooling effectiveness with such a cascade. The only

variable in this experiment was the mass flux ratio, which was varied from 0.2 to 3.0. Their paper presents the variation of the film cooling effectiveness both in the downstream direction and in the spanwise direction. The conclusion arrived at was that the convex side of the model was more effectively cooled than the concave side.

Krishnamoorthy (1982) used turbine blade models in a cascade arrangement and studied the influence of free stream turbulence intensity on the heat transfer coefficient. The Reynolds number based on the free stream velocity and blade chord was varied between 200,000 and 450,000, and the turbulence intensity was varied up to 21%. The author develops an empirical formula to determine the heat transfer coefficient in turbulent flow based on the heat transfer coefficient in non-turbulent flow and the turbulence intensity. The important conclusion is that the local heat transfer coefficient only changes slightly below 5% turbulence intensity, but it changes considerably at higher turbulence levels. This is explained by the more significant penetration of the boundary layer by the turbulent flow.

In the experimental investigation conducted by Camci and Arts (1990), a model blade similar to a turbine blade was made from glass ceramic and instrumented with thin film gages. The free-stream temperature was set at 415 K with the turbulence intensity varying from 0.8 to 5 percent, the mass flux ratio was varied from 0.5 to 3.1, and the main stream velocity approached Mach 1. The conclusions arrived at in this investigation were that film cooling is effective at low mass flux ratios; the distribution of the convective heat transfer coefficient is strongly dependent on the coolant to free-stream temperature ratio; and the free-stream turbulence intensity does not significantly affect the heat transfer characteristics. The last statement confirms the conclusion of Krishnamoorthy (1982) that the free stream turbulence intensity only becomes significant beyond 5%.

A series of papers published by Kikkawa *et al.* (1985, 1987a, 1987b, 1988, 1990) investigates in detail film cooling of a turbine cascade. All the different experiments used the same facility and the same basic shape for the model turbine blade. The experiments employed either the heat-mass transfer analogy or directly measured temperature values to determine the local film cooling effectiveness. The various aspects explored in the paper by Kikkawa and Iwasaki (1985) is the effect of mass flux ratio, slot location, pitch-chord ratio, stagger angle, incidence angle, and turbulence intensity. The conclusions of this investigation were that the pressure coefficient decreases slightly with the increase of mass flux ratio; film cooling effectiveness increases with increasing mass flux ratios up to a maximum value and decreases afterwards; the pitch to chord ratio and the stagger angle does not significantly affect the film cooling effectiveness; the film cooling effectiveness increases on the suction surface with an increase of the incidence angle, but does not significantly change on the pressure side; and the turbulence intensity gradually decreases the film cooling effectiveness on both sides of the model, but becomes significant only when the turbulence is larger than 4%. The paper by Kikkawa and Nakanishi (1987b) explores the mass flux ratio, injection angle, injection hole location, pitch-chord ratio, and incidence influence on film cooling effectiveness. The conclusions drawn are that the optimum film cooling effectiveness is achieved at a significantly lower mass flux ratio than that with slot injection; the profile of the film cooling effectiveness for low mass flux ratios is not significantly affected by the location or the angle of injection; and the film cooling effectiveness increases with decreasing pitch to chord ratio and with increasing incidence angle. The papers published by Kikkawa and Hayashida (1987a), by Kikkawa and Okui (1988), and by Kikkawa and Sakaguchi (1990) explore variations of the experiments discussed above by studying the effect of two-dimensional film cooling, and three-dimensional discrete-hole injection. The result is an empirical equation that can determine the contour, along the surface, where the film cooling effectiveness is 0.5.

Using this result and the principle of superposition, the distribution of the full-coverage film cooling effectiveness can be predicted.

1.3.4 Discrete-Hole Film Cooling of a Blunt Body with Semi-Circular Leading Edge

In investigations of film cooling of the leading edge of gas turbine blades, models with a semi-circular leading edge, connected to a flat surface parallel to the main stream flow, and a tapered trailing edge have been used quite extensively. The injection holes are located in the semi-circular leading edge at various angles from the stagnation line. Such a model blade is also used in this work. A schematic illustration of this type of model blade is given in Fig. 1.

The model used by Mick and Mayle (1988) has four rows of injection holes at $\pm 15^\circ$ and at $\pm 44^\circ$ from the stagnation point. The injection holes were four diameters apart and angled at 30° to the surface in the spanwise direction. The Reynolds number based on the main stream velocity and the leading edge diameter was kept fixed at 100,000, and the mass flux ratio was either 0.38, 0.64, or 0.97. Their research shows that film cooling effectiveness and heat transfer rapidly change both downstream of and in between the holes. The film cooling effectiveness also appears to decrease with the increase of the mass flux ratio around the injection holes, but has the opposite variation further downstream. Finally, the area of high film cooling effectiveness does not necessarily translate to a region of high heat transfer, and the disparity between these two results increases as the mass flux ratio is increased.

Using the same equipment, model, and test conditions as in Mick and Mayle (1988), Mayle and Anderson (1991) determined the velocity and temperature profiles. The findings of this study demonstrate that the film cooling jets affect considerably both the

velocity and temperature profiles; the jets immediately leave the surface at high mass flux ratios, thus eliminating any benefit the additional mass flow might bring, whereas at low mass flux ratios the injected fluid remains on the surface, but has a low mass flow; the boundary layer thickness with injection is much larger than without injection, and it is highly three dimensional; and the aerodynamic loss caused by the injection of the secondary flow is linearly proportional the mass flux ratio.

Model blades similar to that illustrated in Fig. 1 are also used in a series of papers published Han *et al.* (1988), Mehendale *et al.* (1991, 1992a, 1992b), and Ou *et al.* (1992a, 1992b). The injection holes are placed at $\pm 15^\circ$ and at $\pm 40^\circ$ from the center of the leading edge. The injection tubes are inclined 90° from the surface in the streamwise direction and 30° in the spanwise direction. The surface of the model is covered with 3.8 cm wide stainless steel strips that are linked electrically in a snaked fashion to provide heating for the surface. The aspect ratio of the model is 1.67, the injection hole to leading edge diameter ratio is .072, and the ratio of the length to the diameter of the injection tubes is 5.1. The injection tube is angled at 30° to the surface, making the effective length to diameter ratio of 3.37. The temperature is measured using 88 T-type thermocouples placed near three injection holes in the 15° row, two injection holes in the 40° row, and downstream of these five holes. The main stream velocity was determined using a pitot-static tube, and the turbulence intensity was determined using a single hot wire and 1032 readings per data point. The turbulence was generated using grids placed 47.6 cm upstream of the model.

The paper by Mehendale, Han, and Ou (1991) studies heat transfer from the leading edge. The variables of this experiment are the upstream turbulence intensity level that was varied from 0.5% to 15.2%, and the Reynolds number, based on the main stream velocity and leading edge diameter, set at 25,000, 40,000, and 100,000. The model did not have

injection holes. The findings of this study are that the heat transfer in the leading-edge region increases significantly with increasing main stream turbulence intensity; the separation and reattachment locations are not affected significantly by the turbulence level; and the turbulence level does not affect significantly the heat transfer far downstream on the flat surface of the model blade.

The research by Ou, Mehendale, and Han (1992b) investigates the effect of the location of the injection hole row on the leading-edge film cooling. The Reynolds number based on the model diameter, was kept constant at 100,000. The turbulence intensity was varied between four values from 0.5% to 12.9%, and three mass flux ratios were investigated, 0.4, 0.8, and 1.2. The main conclusions of this study are that an increase in the main stream turbulence intensity decreased the film cooling effectiveness; the heat transfer coefficient increased with increasing mass flux ratio and increasing turbulence intensity; and surface heat load, as defined in Mick and Mayle(1988), decreased with decreasing mass flux ratios.

The paper by Mehendale and Han (1992a) used the same parameters as those in the previous paper [Ou, Mehendale, and Han, 1992b]. The findings of this paper are that the surface heat load increased with increasing mass flux ratio, except in the area between the two rows; the film cooling effectiveness decreased with increasing blowing ratio except between the two rows where the film cooling effectiveness is the highest at a mass flux ratio of 0.8, and decreased when the turbulence intensity increased; and the heat transfer coefficient increased with increasing mass flux ratio and increasing turbulence intensity.

Mehendale and Han (1992b) studied the effect of injection hole spacing. Their research investigated the variation of film cooling effectiveness with the injection holes spaced at 3 and 4 diameters apart. The experimental conditions corresponded to a Reynolds

number, based on main stream velocity and leading-edge diameter, of 100,000, mass flux ratio of 0.4, 0.8 and 1.2, and four different levels of turbulence intensity. The reported results were that the heat transfer coefficient increased with an increase in mass flux ratio, and with an increase of the turbulence intensity; and injection holes placed further apart lead to lower heat transfer coefficients than those obtained with injection holes placed close together.

The paper by Ou and Han (1992) studies the effect of using *non-circular* injection holes on the heat transfer from the leading edge. The experimental conditions and variations are identical to those of Mehendale and Han (1992b). The holes are rectangular with circular ends, however, the orientation of the injection tubes remains the same as that in Mehendale and Han (1992a, 1992b). The injection holes have length to width ratio of 2, with the orientation of the longest side in the spanwise direction. The conclusion of this study is that the leading-edge heat transfer increases with an increase in the mass flux ratio, and with increasing main stream turbulence level; the film cooling effectiveness decreases with increasing turbulence level, however, the significance of this relation decreases with the increase of the mass flux ratio; and the optimal mass flux ratio increases with increasing main stream turbulence intensity.

The paper by Saicudean *et al.* (1994) discusses the film cooling effectiveness near the leading edge of a model blade. They used a flame ionization technique based on the heat/mass transfer analogy. The model in this study was geometrically similar to the model used by Mick and Mayle (1988). The free-stream velocity was varied from 2 to 20 m/s, the mass flux ratio was $0.35 < M < 1.00$, and the turbulence intensity was maintained constant at 0.5%. The main conclusions of this study were: at low mass flux ratio, the secondary flow from the first row of holes can be completely shutoff, endangering the leading edge; the optimal mass flux ratio was 0.45, however, a slight variation from this

optimal value brings about a significant decrease in the film cooling effectiveness; the injected fluid from the first row tends to flow towards the injection holes in the second row; and the chosen injection tube arrangement and inclination result in a poor overall performance with respect to the film cooling effectiveness.

1.4 Overview of the Thesis

The presentation of thesis is divided into five chapters. The goals and motivation of this thesis and a literature review relevant to this research have been already presented in the earlier sections of this chapter. In Chapter 2, certain theoretical considerations that are pertinent to this thesis are discussed. The third chapter of this thesis discusses in detail the experimental apparatus and procedure. The test section design is also discussed and the details of the final arrangement are given, along with a description of the measuring apparatus and the calibration of the instruments. The chapter finishes with a summary of the procedure utilized for the experiment. Chapter 4 presents and discusses the results of the experiment. In Chapter 5, a summary of the conclusions drawn from this work are presented, along with a summary of the contributions of this work, and suggestions for improvements and possible extensions.

Chapter 2

THEORETICAL CONSIDERATIONS

In the design of the experimental apparatus and the processing of the experimental data, a number of theoretical considerations pertaining to film cooling and hot wire anemometry were necessary. These theoretical considerations, based on the works of Goldstein (1971), Han *et al.* (1988), and Mayle *et al.* (1976, 1991), are presented in this chapter.

2.1 Adiabatic Wall Temperature and Film Cooling Effectiveness

As was mentioned in Chapter 1, one of the objectives of this work is to study the influence of upstream turbulence intensity on the discrete-hole film cooling of a model blade in confined cross flow. The model blade used in this work is shown in Fig. 1. A schematic illustration of the blower cascade wind tunnel used in this work is given in Fig. 3, and a cross-sectional view of the test section with the model blade mounted inside it is given in Fig. 2.

In the design of film cooling schemes, the general aim is to predict, for a given geometry, primary (or main stream) flow, and injected (or secondary) flow, the relationship between the wall temperature distribution and heat transfer [Goldstein, 1971]. Alternatively, for a given geometry, primary flow, and heat transfer, the requirement may be to predict the secondary flow that is needed to maintain the surface temperature below some critical value [Goldstein, 1971].

In this thesis, attention is limited to low-speed (Mach number <0.1) flows. In such flows, the compressibility effects can be assumed to be negligible. Furthermore, if the range of

temperature variations is not too large (typically, for air, $\pm 100^\circ\text{C}$ about some mean value of temperature), it may be assumed that the thermophysical properties of the fluid are essentially constant at values corresponding to the mean temperature.

For incompressible, constant-property flows, the velocity distribution is independent of the temperature distribution, and it is convenient to use the concept of a convective heat transfer coefficient:

$$\dot{q}_{conv} = h \cdot \Delta T = h(T_w - T_{ref}) \quad (1)$$

where \dot{q}_{conv} is the local heat flux from the wall to the fluid, h is the local heat transfer coefficient, T_w is the local wall temperature, and T_{ref} is a suitable reference, or datum, temperature. In the limiting case of a perfectly insulated (or adiabatic) surface, the heat flux, \dot{q}_{conv} , would be zero, and the resulting surface temperature distribution is called the *adiabatic wall temperature*, T_{aw} . In film cooling applications involving incompressible flow, the reference temperature in Eq. (1) is chosen to be the local adiabatic wall temperature. Thus,

$$\dot{q}_{conv} = h \cdot \Delta T = h(T_w - T_{aw}) \quad (2)$$

The use of Eq. (2) in low-speed, constant-property flows yields a heat transfer coefficient that is independent of the temperature difference [Goldstein, 1971]. It should be noted that in the absence of blowing (no injection), T_{aw} is equivalent to the main stream, or primary flow, temperature, T_∞ .

Often, the heat transfer coefficient is found to be relatively close to the value obtained without secondary flow [Goldstein, 1971], except in the immediate vicinity of the

injection hole at high mass flux ratios. On the other hand, the adiabatic wall temperature distribution can vary considerably with secondary flow, and is harder to predict. In addition, the adiabatic wall temperature is significant because it is the limiting value of wall temperature that is obtained *without* internal wall cooling or conduction heat transfer within the walls of the blade. Thus, most film cooling studies have treated the determination of heat transfer coefficient and adiabatic wall temperature distribution separately, with primary emphasis on the latter [Goldstein, 1971].

The adiabatic wall temperature is a function of the geometry, the primary and secondary flow fields, and the temperatures of the two gas streams. To eliminate this temperature dependence, a dimensionless adiabatic wall temperature, η , called the *film cooling effectiveness* is used. For low-speed, constant-property flows, the film cooling effectiveness is defined as follows [Goldstein, 1971]:

$$\eta = \frac{T_{aw} - T_{\infty}}{T_s - T_{\infty}} \quad (3)$$

where the temperatures of the primary flow, T_{∞} , and the secondary flow, T_s , are assumed constant. In low-speed, constant-property flows, the energy equation is linear in temperature, thus the film cooling effectiveness is dependent only on the geometry, primary and secondary flows, and the position on the surface. It should be noted here that this film cooling effectiveness varies from unity at the point of injection, where $T_{aw} = T_s$, to zero far downstream, where, because of the dilution of the secondary flow, $T_{aw} = T_{\infty}$.

2.2 Experimental Determination of Film Cooling Effectiveness

In experimental studies of film cooling, it is impossible to completely eliminate the effects of conduction heat transfer within the model blade and radiation heat transfer from

the surface of the blade to the surroundings. Thus the measured surface temperature, T_w , does not correspond to the adiabatic wall temperature, T_{aw} . Therefore, the measured wall temperature, T_w , has to be suitably compensated, or processed, to determine the film cooling effectiveness, η , as defined in Eq. (3).

Consider a local energy balance on the surface of the model blade, as shown schematically in Fig. 5. Under steady-state conditions,

$$q_{conv}'' + q_{rad}'' + q_{cond}'' = 0 \quad (4)$$

where q_{conv}'' is the heat flux due to convection heat transfer from the surface of the blade to the fluid flow over it, q_{rad}'' is the heat flux due to radiation heat transfer from the surface of the blade to the surroundings, and q_{cond}'' is the conduction heat flux into the blade.

The convection heat flux, q_{conv}'' , is given by Eq. (2). As was mentioned in the previous subsection, the heat transfer coefficient, h , in this equation is often found to be very close to that obtained without secondary flow [Goldstein, 1971]. In this work, it was assumed that for the same Reynolds number and upstream turbulence intensity of the cross flow, the h values with and without secondary flow are the same. The values of h without secondary flow were determined experimentally. A detailed description of the apparatus and procedures that were used to obtain h will be presented in the next chapter. The theoretical considerations that were used to obtain h from the experimental data are discussed in the next subsection.

The radiation heat flux, q_{rad}'' , is given by

$$q_{rad}'' = \sigma \epsilon (T_{w_{ABS}}^4 - T_{\infty_{ABS}}^4) \quad (5)$$

where σ is the Stefan-Boltzmann constant, ϵ is the emissivity of the surface, $T_{w_{ABS}}$ is the absolute value of the local surface temperature, and $T_{\infty_{ABS}}$ is the absolute value of the temperature of the primary flow. Here, it is assumed that the surroundings can be approximated as a very large isothermal enclosure at the uniform temperature $T_{\infty_{ABS}}$, and the primary and secondary fluid flows are assumed to be radiatively non-participating.

The conduction heat flux, q_{cond}'' , is obtained by considering an energy balance on a small segment, or control volume, surrounding the location of interest, or node, on the surface of the model blade. Such a control volume is illustrated in Fig. 6. The blade is made of acrylic, and it is insulated on the inside surface with a polyurethane foam insulation. Complete details of the construction of the model blade are given in Chapter 3. With reference to the notation in Fig. 6, it is assumed that the rate of conduction heat transfer, q_{cond} , is due to the rate of tangential conduction heat transfer, q_{cond_T} , within the acrylic wall, and normal conduction heat transfer, q_{cond_N} , through the acrylic wall and insulation to the secondary fluid in the plenum chamber within the model blade. The tangential component, q_{cond_T} , is determined by using measured temperatures at numerous points on the surface of the model blade, assuming essentially two-dimensional temperature distribution with the acrylic wall (noting that the thermal conductivity of the insulation is much smaller than the thermal conductivity of acrylic), and a control-volume-based finite element method. Details of this procedure are given later in this chapter. The normal component, q_{cond_N} , is obtained by using a locally one-dimensional model of heat transfer through the blade:

$$q_{cond_N} = \frac{A_p (T_w - T_s)}{[(\delta_a / k_a) + (\delta_i / k_i) + (1 / h_p)]} \quad (6)$$

where, using the notation shown in Fig. 6, A_p is the surface area of the segment or control volume, δ_a is the thickness of the acrylic wall, δ_i is the thickness of the insulation, k_a is the thermal conductivity of the acrylic, k_i is the thermal conductivity of the insulation, and h_p is the heat transfer coefficient at the interface between the insulation and the secondary air in the plenum chamber within the model blade. The value of h_p was estimated from experimental measurements.

Under steady-state conditions, an energy balance on the control volume shown in Fig. 6 gives:

$$q_{cond} = q_{cond_T} + q_{cond_N} \quad (7)$$

Using Eq. (6) in Eq. (7), the following relation is obtained for q_{cond}^* :

$$q_{cond}^* = \frac{q_{cond}}{A_p} = \frac{q_{cond_T}}{A_p} + \frac{T_w - T_s}{\left[(\delta_a / k_a) + (\delta_i / k_i) + (1 / h_p) \right]} \quad (8)$$

The measured wall temperature, T_w , is nondimensionalized as follows:

$$\eta^* = \frac{T_w - T_\infty}{T_s - T_\infty} \quad (9)$$

Combining Eqs. (2) to (9), the following expression is obtained for the film cooling effectiveness:

$$\eta = \frac{T_w - T_\infty}{T_s - T_\infty} + \frac{q_{rad}^* + q_{cond}^*}{h(T_s - T_\infty)} = \eta^* + \frac{q_{rad}^* + q_{cond}^*}{h(T_s - T_\infty)} \quad (10)$$

2.3 Experimental Determination of the Heat Transfer Coefficient on the External Surface of the Model Blade without Secondary Flow

The model blade, depicted schematically in Fig. 1, was designed so that it could be used with its injection holes open, in film-cooling studies, or with its injection holes plugged, in investigations of heat transfer on its external surface without secondary flow. In the heat transfer investigations without secondary flow, the model blade was covered with a thin, electrically conducting film, made by vapor deposition of indium/tin oxide on a polymer base. Electrodes were attached to this film at the ends of the blade adjacent to the walls of the test section. This film was heated using a DC power supply, and the temperature distribution on the external surface of the blade was measured using thin (30 gauge) chromel-constantan (Type E) thermocouples. Additional details of the experimental apparatus are given in the next chapter.

Through independent tests that were carried out as a part of this work, the surface electrical resistance of the indium/tin oxide film was found to be related to the local temperature of the film by the following relation:

$$R = 0.0375 \cdot T + 61.36 \quad (11)$$

where R is given in ohms per square (Ω/sq), and T is the local film temperature in degrees Celsius. In the experiments, the range of film temperatures was $25^\circ\text{C} < T < 70^\circ\text{C}$, thus the electrical resistance of the film could be assumed to be essentially constant at $62 \Omega/\text{sq}$ with an uncertainty of $\pm 5\%$. The electrical power dissipated per unit area of the thin film heater (q_H'') was obtained from the following equation:

$$q_H'' = (V_H I_H) / A_H \quad (12)$$

where V_H is the total voltage drop across the electrodes fixed to the film, I_H is the total current passing through the film, and A_H is the total surface area of the film that is exposed to the cross flow.

In this heat transfer investigation, the radiation heat flux from the surface of the film to the cross flow was obtained in the following manner:

$$q_{rad_{HT TRF}}'' = \sigma \epsilon_H \left(T_{w_{ABS. HT TRF}}^4 - T_{\infty_{ABS}}^4 \right) \quad (13)$$

In this equation, σ is the Stefan-Boltzmann constant, and ϵ_H is the total hemispherical emissivity of the conductive surface of the thin film. In this work, the value of ϵ_H was found to be 0.20.

The conduction heat flux *into* the model blade, $q_{cond_{HT TRF}}''$, was estimated by assuming that the temperature distribution inside the Plexiglas wall of the model blade is quasi one-dimensional, in a manner akin to the basic assumption in classical fin theory: $T_{Model Blade} \cong T_w(x)$, where x is the distance along the external surface of the model blade in the main stream direction (Fig. 3). It was also assumed that there is no heat loss from the inside surface of the model blade to the insulation and air within the blade. With these assumptions,

$$q_{cond_{HT TRF}}'' = -k_a \delta_a d^2 T_w / dx^2 \quad (14)$$

where k_a and δ_a are the thermal conductivity and thickness, respectively, of the Plexiglas wall of the model blade. The value of δ_a is 12.7 mm, and independent tests yielded the value of 0.21 W/m·°C for k_a .

The value of d^2T_w/dx^2 in Eq. (14) was approximated by using the values of the measured local temperatures along the surface of the model blade. With respect to the notation given in Fig. 7.

$$(d^2T_w/dx^2)_p = \frac{[(T_E - T_P)/(\delta x)_e - (T_P - T_W)/(\delta x)_w]}{[(\delta x)_e + (\delta x)_w]/2} \quad (15)$$

The convective heat flux from the surface of the film to the cross flow of air ($q''_{conv,HT TRF}$) was obtained in the following manner:

$$q''_{conv,HT TRF} = q''_H - q''_{rad,HT TRF} - q''_{cond,HT TRF} \quad (16)$$

The local heat transfer coefficient, $h_{HT TRF}$, the corresponding Nusselt number, Nu , and a nondimensional surface temperature, Φ , on the external surface of the model blade in these heat transfer studies are defined as follows:

$$h_{HT TRF} = q''_{conv,HT TRF} / (T_{W,HT TRF} - T_\infty) \quad (17)$$

$$Nu = hD/k_\infty \quad (18)$$

$$\Phi = (T_{W,HT TRF} - T_\infty) / (T_{W,x=0,HT TRF} - T_\infty) \quad (19)$$

where D is the diameter of the semicircular leading edge of the model blade, and k is the thermal conductivity of the air.

2.4 Determination of Tangential Heat Conduction within the Wall of the Model Blade in Film-Cooling Studies

In this section, the method that was used to determine the value of $q_{cond\tau}$ in Eq. (7) is described.

The points at which the local temperature of the surface of the model blade is measured are first connected by a grid of triangular elements, as shown in Fig. 8. It is then assumed that the variation of the temperature in the model blade in a direction normal to its surface is negligible compared to its variation in directions that are tangential to the surface:

$T_w \cong T_w(x, z)$, where x is the coordinate along the surface of the blade in the direction of the main stream (Fig. 3), and z is the coordinate normal to x , but lying in the surface of the model blade. This assumption is akin to assuming that the wall of the model blade behaves as a two-dimensional fin. With this assumption, the heat conduction flux vector lying in the surface of the model blade is given by:

$$\bar{q}_{cond\tau}'' = -k_a \left(\frac{\partial T}{\partial x} \bar{i} + \frac{\partial T}{\partial z} \bar{k} \right) \quad (20)$$

where k_a is the thermal conductivity of the Plexiglas wall of the model blade, \bar{i} and \bar{k} are unit vectors in the x and z directions, respectively.

Consider a point P and neighboring points at which the local temperature of the surface of the model blade is measured. The triangular elements which connect these points are shown in Fig. 9.

Following Baliga and Patankar (1983, 1988), the centroids of the triangular elements are joined to the midpoints of the sides. As shown in Fig. 9, this procedure creates polygonal control volumes around each point (or node) of interest. With respect to the control volume surrounding point P (also denoted as node 1 in Fig. 9), the rate of tangential heat conduction, $(q_{cond_r})_p$, out of this control volume is given by:

$$(q_{cond_r})_p = \delta_a \left\{ \left[\int_a^o \bar{q}''_{cond_r} \cdot \bar{n} ds + \int_o^c \bar{q}''_{cond_r} \cdot \bar{n} ds \right] + \right. \\ \left. [\text{similar contributions from other elements associated with node P}] \right\} \quad (21)$$

where \bar{n} is a unit vector normal to the boundary of the control volume, pointing *out* of the control volume, and δ_a is the thickness of the Plexiglas wall of the model blade.

Within each triangular element, it is assumed that the temperature varies linearly. Thus, with respect to a typical element, 1-2-3, shown in Fig. 9. the temperature variation is given by:

$$T = Ax^* + Bz^* + C \quad (22)$$

where x^* and z^* are element-based Cartesian coordinates, parallel to the global x and z coordinate directions, respectively, and with the origin located at the centroid of the element. The constants A , B , and C in this interpolation function are determined by requiring that the temperature at the vertices of the triangular element equal the measured values [Baliga and Patankar, 1983, 1988].

$$A = [(z_2 - z_3)T_1 + (z_3 - z_1)T_2 + (z_1 - z_2)T_3] / DET \quad (23)$$

$$B = [(x_3 - x_2)T_1 + (x_1 - x_3)T_2 + (x_2 - x_1)T_3] / DET \quad (24)$$

$$C = [(x_2z_3 - x_3z_2)T_1 + (x_3z_1 - x_1z_3)T_2 + (x_1z_2 - x_2z_1)T_3] / DET \quad (25)$$

$$DET = (x_1z_2 + x_2z_3 + x_3z_1 - z_1x_2 - z_2x_3 - z_3x_1) \quad (26)$$

It is worth noting here that $|DET|$ is twice the area of the triangular element. Using the linear interpolation function in Eq. (22), the tangential heat conduction flux vector, \bar{q}''_{cond_T} , can be expressed as follows:

$$\bar{q}''_{cond_T} = -\delta_a (A\bar{i} + B\bar{k}) \quad (27)$$

The rate of tangential heat conduction *out* of the control volume surrounding point P is given by:

$$\begin{aligned} (\bar{q}''_{cond_T})_p = \delta_a \{ & [(Ak_a z'_a - Bk_a x'_a) - (Ak_a z'_c - Bk_a x'_c)] + \\ & [\text{similar contributions from other elements associated with point P}] \} \end{aligned} \quad (28)$$

It is important to note that for these expressions to be valid, x' and z' must be measured with respect to a local Cartesian coordinate system within each element, and the node numbering system for *each* element must be in a counter-clockwise sense as shown in Fig. 9.

2.5 Constant-Temperature Hot Wire Anemometry

The constant-temperature hot-wire anemometer (CTA) is an instantaneous velocity measuring device. The major components of this anemometer are a hot-wire probe, a bridge, a linearizer, and a voltage meter. The probe is a heated, electrically conducting filament exposed to the fluid flow of interest. The bridge supplies the probe with the electrical power required to maintain it at a constant temperature. The linearizer takes the voltage output of the bridge and amplifies it, in addition to linearizing the signal. Finally, the high-speed voltmeter records the output of the linearizer. The system is calibrated such that the recorded voltage is correlated with a known velocity. Further details of this equipment and the calibration procedure are given in Chapter 3.

In this experiment, a cross-wire or X-probe was used, so that the instantaneous velocity in both the streamwise and spanwise directions could be measured. The X-probe consists of two hot-wire filaments. The filaments are perpendicular to each other and each is oriented at 45° to the streamwise direction. The advantage of this probe is the capability of obtaining an instantaneous velocity vector, in two-dimensional flows, and by using statistics, the overall time-average velocity vector. It should be noted, however, that CTA is inherently very delicate and requires frequent calibration. The calibration procedure is described in detail in Section 3.4.3.

Since it is practically impossible to derive an exact theoretical equation to describe the response of the hot wire, many different empirical schemes have been used. The method used for this study is described by Champagne *et al.* (1967a, 1967b). It states that the voltage necessary to maintain the hot wire at a desired temperature is proportional to the effective velocity experienced by the probe. To relate the effective velocity and the actual flow velocity, Champagne proposed the following equation

$$U_{e1}^2(\alpha) = U_{\alpha=0}^2 \cdot (\cos^2 \alpha + k^2 \sin^2 \alpha) \quad (29)$$

where α is the angle between the velocity vector and the normal of the wire and k is a correction factor to account for the effect of the velocity component parallel to the axis of the wire. In this work k was set equal to 0.1 based on recommendations of Champagne *et al.* (1967a, 1967b). For a single wire normal to the flow, the above relationship makes the effective velocity equal to the actual velocity. In the case of an X-probe, the determination of velocity magnitude and direction become considerably more complicated. The derivation of the equations presented below is done in detail in Appendix A.

$$\frac{U_{e2}^2}{U_{e1}^2} - \frac{\sin^2(\varphi - \theta) \cdot (1 - k^2) + k^2}{\sin^2 \theta \cdot (1 - k^2) + k^2} = 0 \quad (30)$$

$$U^2 = \frac{U_{e1}^2}{\sin^2 \theta + k^2 \cos^2 \theta} \quad (31)$$

U_{e1} represents the effective velocity for the first wire, U_{e2} represents the effective velocity for the second wire, φ is the angle between the two wires, and θ is the angle between the first wire and the actual velocity vector, as shown in Fig. 10. The values of U_{e1} and U_{e2} are obtained from the measured instantaneous voltages across wires 1 and 2, using the appropriate calibration curves. Eq. (30) is not linear, therefore, to determine the angle θ an iterative procedure must be used. In this work, the secant method described by Gerald (1978) was used. Once the angle θ is determined, the magnitude of the actual velocity, U , can be obtained by using Eq. (31) directly.

To calculate the mean velocity, the velocity vector is broken into the components in the X and Y directions, shown in Fig. 10:

$$\begin{aligned}u &= U \cos(\varphi/2 - \theta) \\v &= U \sin(\varphi/2 - \theta)\end{aligned}\tag{32}$$

Where u is the streamwise component, and v is the Y component. The average velocity for each component is determined, and then the average velocity vector is determined by adding vectorially the two mean velocity components.

The CTA was also used in this work to determine the turbulence intensity of the primary air flow. The mean-square of the fluctuation of the streamwise velocity is determined by

$$u'^2 = \frac{\sum_{i=1}^n (\bar{u} - u)^2}{n}\tag{33}$$

where \bar{u} is mean velocity component in the streamwise direction, and n is number of data samples. Similarly, the mean-square of the fluctuation of the cross stream velocity is determined. It is assumed that $w'^2 = v'^2$. The turbulence intensity is then given by

$$TI = \sqrt{\frac{u'^2 + v'^2 + w'^2}{\bar{U}^2}}\tag{34}$$

Chapter 3

EXPERIMENTAL APPARATUS AND PROCEDURES

The experimental set-up that was used in this work is discussed in this chapter in four parts: (a) test section and model blade; (b) systems for primary and secondary air flows; (c) grids for generating turbulence; and (d) data acquisition instrumentation, and control. A schematic illustration of the overall experimental set-up is given in Fig. 11. Also included in this chapter are concise descriptions of the methods that were used to calibrate the various instruments used for acquiring data. Experimental procedures are also summarized in this chapter.

3.1 Test Section and Model Blade

The model blade that was used in this study is a blunt body with a semicircular leading edge, a flat after body, and a tapered trailing edge. Similar model blades have been used by Bellows and Mayle (1986), Mehendale *et al.* (1991, 1992a, 1992b), Saabas (1991), and Salcudean *et al.* (1994). Schematic illustrations of the model blade, and relevant geometric dimensions, are given in Figs. 1 and 3.

As can be seen in Fig. 1, the model blade has provisions for discrete-hole film cooling studies. The injection holes are arranged in two rows, each row consisting of eight equally-spaced holes, 30° from the stagnation line. The injection holes are fed by injection tubes, each of inner diameter 13.2 mm and length 38 mm. The spacing between the injection holes, in the z direction with respect to the coordinate axes shown in Fig. 1, is 0.0635 m from center to center. The centers of the last holes in each row are 0.159 m from the nearest wall of the test section. The design of the model blade allowed easy opening and closing of the injection holes.

The model blade was made of 12.7 mm (½ inch) thick Plexiglas. The model blade was mounted in a test section, as shown in Fig. 3, and it was supported between two clear acrylic walls of the test section. Rubber gaskets were used between the model and these supporting walls. The model was centered by dowel pins on either side, leveled so that the flow was evenly distributed below and above the model, and then squeezed into place. The even distribution of the flow on the top and bottom surfaces of the model was verified by static pressure measurements at several symmetrically placed pressure taps. The model blade was maintained at a zero angle of incidence to the upstream cross flow throughout this work.

In studies of the influence of upstream turbulence on heat transfer without film cooling, all of the injection holes were plugged. The model blade was covered with a thin, electrically conducting film, made by vapor deposition of indium/tin oxide on a polymer base. Copper electrodes were attached to this film at the ends of the blade adjacent to the walls of the test section. The indium/tin oxide film used in this study was manufactured by Courtaulds Performance Films, in Canoga Park, California, U.S.A. As was stated in Chapter 2, the electrical resistance of this film was found to be $62 \Omega/\text{sq}$ within $\pm 5\%$. In the heat transfer experiments, the film was heated using a DC power supply, and the local surface temperatures were measured using chromel-constantan thermocouples, calibrated to $\pm 0.05^\circ\text{C}$ accuracy. Similar thin-film techniques have been used for the measurement of local heat transfer coefficients in earlier investigation by Baughn *et al.* (1985, 1986), Hippensteele *et al.* (1985), Neill (1989), and Bernier and Baliga (1992).

Fifty-five thermocouples of type E were used to measure the surface temperature of the model blade in the immediate vicinity and downstream of one injection hole. The injection hole selected to be studied was the fourth one from the left on the top row. The

central location of this injection hole ensured that the fluid dynamics and heat transfer characteristics inside geometrically similar modules on either side of this hole were essentially the same. As was mentioned earlier, in addition to these thermocouples, there were four static pressure taps on the model blade surface. These static pressure taps were used for dynamically centering the model in the tunnel.

3.2 Systems for Primary and Secondary Air Flow

The primary air flow was generated by a blower cascade wind tunnel in the Aerodynamics Laboratory at McGill University [Wyganski and Gartshore, 1963]. A schematic illustration of this tunnel is given in Fig. 3. It is an open-return type wind tunnel, in which the air flow is created by a centrifugal fan. The air is exhausted into the laboratory and circulated back to the blower through a wall of filters. The fan, for this experiment was driven by a 5 hp DC shunt motor. The electric power for this motor was provided by three Kepco power supplies (Model ATE 100-10M). Each of the power supplies is capable of providing 1000 W of power, with a maximum voltage of 100 V and current of 10 A. The power supplies were connected in parallel, in order to obtain a maximum current of 30 A. The speed of the fan was controlled by appropriate variation of the electrical power fed to the motor. The voltage going to the motor was computer controlled, as described in a following section of this chapter. A 6:1 area reduction, three fine screens, and a honeycomb-style flow straightener in the wide section, all shown schematically in Fig. 2, enable the wind tunnel to produce an even air flow at low turbulence. The exit of this tunnel is 0.432 m high and 0.762 m wide, and is specially designed so that a test section can be attached and removed easily. At this exit section, outside the boundary layer, the maximum spatial variation in the velocity is 1%, and the maximum turbulence level is less than 1%. The Aerodynamics Laboratory has its own

separate environmental control unit that maintains the air in the laboratory, as well as the primary air flow, at an essentially constant temperature of 21°C.

The secondary air flow was generated by a centrifugal blower, driven by a 10 hp constant speed AC motor. The air for this blower was taken from the Aerodynamics Laboratory through a filter. The air exiting the blower was split into two branches, one of which, termed the bypass branch, exhausted the air back into the laboratory, and the other, the secondary-air branch, provided air that was fed to the injection tubes in the film cooling studies. By using the by-pass branch, the blower could be maintained at a cooler temperature, and the effect of adjusting the mass flux ratio on the motor's performance was reduced. The secondary-air branch was fitted with a gate valve that was used to regulate the air flow into the plenum chamber of the model blade. Before being fed to the plenum chamber of the model blade, the secondary air was passed through a section consisting of five variable heating coils of 1000 W to 1500 W. After this heating section, the air was fed to a large mixing box to make it isothermal, and then passed through a flow-measuring tube made of acrylic. At the end of the flow-measuring tube, a traversing pitot stagnation tube and wall static pressure taps, were used to measure the air flow velocity at specific locations determined by the ten-point log-linear method [Ower and Pankhurst, 1966], that was used to calculate the total mass flow rate of the secondary air. A detailed description of the instruments, and procedures are presented in the data-acquisition section of this chapter. After the flow-measuring section, the secondary air was fed into the plenum chamber of the model blade through an acrylic tube fitted through the side wall of the test section. The diameter of the acrylic tube was seven times larger than the diameter of the injection tubes: this ensured that the velocity of the air flow to the plenum never surpassed 1 m/s, and the static pressure in the plenum chamber was essentially constant. Furthermore, with this arrangement, as verified by Saabas (1991), the velocity of the air emerging through the injection holes in the surface of the

blade, in the absence of primary cross flow in the test section, is essentially uniform (deviation $< 2\%$).

3.3 Grids for Generating Turbulence

The blower cascade wind tunnel produced turbulence intensities in the range 0.6% to 0.9% over the range of cross flow velocities considered in this work. Higher upstream turbulence intensities were obtained by using two different grids, denoted as Grids 1 and 2, each of a pattern similar to that shown in Fig. 4. Grid 1 consisted of bars of 6.5 mm square cross section, separated by 22.2 mm. Grid 2 was made with bars of 11.0 mm square cross section, separated by 37.6 mm. With Grid 1, the turbulence intensity at a distance 1.3D upstream of the stagnation line on the model blade was about 9.8%, and with Grid 2, the turbulence intensity at this location was about 14.4%; D (=0.126 m) is the diameter of the semi-circular leading edge of the model blade. These grids were designed using recommendations of Baines and Peterson (1951), and Mehendale *et al.* (1991, 1992a, 1992b). In all cases, the stagnation line on the semicircular leading edge of the model blade was located 4.7D downstream of the grid.

The variations of the turbulence intensity with nondimensional distance (X/D) from the position of the grid, along a straight line located at $Z/D = 0.0$ and $Y/D = 1.7D$, are presented in Fig. 14. These variations of turbulence intensity were essentially insensitive to the Reynolds number for the cases considered in this study.

3.4 Data Acquisition, Instrumentation, and Control

3.4.1 Data Acquisition

Two different systems were used for data acquisition in the experiments described in this thesis. The main system consisted of a small network of measuring devices connected

through bus cables in series to a special serial card installed in a personal computer with an Intel 80486 chip, following the IEEE 488.2 protocol. This system is called Hewlett Packard Interface Bus (HP-IB) by the Hewlett Packard (HP) company, or GP-IB by other companies that use this protocol. On this network there were two multimeters (HP Model 3478A) and a data acquisition unit (HP Model 3497A) with three twenty-channel thermocouple multiplexor cards, one twenty-channel multiplexor card, and an eight-channel actuator card. The digital voltmeter built into the data acquisition unit is capable of reading up to a resolution of $1\mu\text{V}$, at a rate of 60 readings per second, and an accuracy of $\pm 3\mu\text{V}$.

The second system was designed around a Keithley Metrabyte DAS-20 data acquisition card that was plugged into an expansion slot in the personal computer. This card features sixteen single-ended analog input channels and two analog output channels. The data acquisition card has twelve-bit resolution and is capable of taking up to 100,000 readings per second. This system was used for acquiring signals from a constant-temperature hot wire anemometer, and to control the power supply to the DC motor that was used to drive the fan of the wind tunnel.

3.4.2 Temperature Measurement

The temperature measurements in this work were done using a total of sixty chromel-constantan (Type E) thermocouples. The thermocouples were fabricated in the Heat Transfer Laboratory using a spot welder and 30 gauge chromel-constantan wire (Omega TT-E-30) with teflon insulation. These thermocouples were connected to three thermocouple multiplexor cards which were installed in a data acquisition unit (HP Model 3497A). The thermocouple multiplexor cards had internal hardware compensation circuitry, thus the zero-degree reference voltage was automatically added to the actual measured voltages.

3.4.3 Differential Pressure Measurements

Differential pressure measurements were made using a Barocel capacitance-type transducer (Datametrix Model 72W 590 23 232). The Barocel was powered by a DC power supply set at 28 volts. This Barocel has an output of -10 to +10 volts DC that is linearly proportional to the applied differential pressure of -1000 to 1000 Pa, with an accuracy of ± 0.05 Pa. The voltage output was connected, through a shielded wire, to one of the channels in the multiplexor card, installed in the main data acquisition unit. The Barocel is a very precise instrument, however the zero-pressure voltage reading tends to drift slightly due to environmental conditions. To correct this problem, a pair of y-branch electronic solenoid valves and the circuit shown in Fig. 12 were used. This tubing circuit was designed so that when the solenoid valves were not powered, the differential pressure of interest was applied to the Barocel, whereas when the valves were powered, the circuit made a closed loop and provided the Barocel with a reference zero-pressure reading. The power to the solenoid valves was obtained from a normal AC power outlet, however, the triggering power to the on-off switch was provided through a channel in the high-voltage actuator card installed in the main data acquisition unit. The objective of this setup was to automate the zeroing process of the Barocel.

It should be noted that the output of the Barocel also fluctuates due to the inherent high sensitivity of the instrument, and also the turbulence of the air flow. To compensate for these fluctuations, the data acquisition system was programmed to take sixty readings and determine the mean voltage value. At the beginning of each data acquisition sequence, the zero-pressure voltage was measured. This voltage was subtracted from subsequent differential pressure readings so as to obtain the correct voltage. The corrected voltage of the Barocel is linearly proportional to the differential pressure, consequently, the voltage need only be multiplied by the slope of the calibration curve that relates differential pressure to voltage output.

3.4.4 Barometric Pressure

A typical series of experimental runs in this study could extend over several days, because approximately four hours were required to achieve steady-state conditions for each run. Thus, the atmospheric pressure could change significantly over the course of one series of experimental runs. The Aerodynamics Laboratory is equipped with a precise mercury barometer (Princo, Fortin type), however, to automate the data acquisition process as much as possible, a Vaisala electronic barometer (Model PTA 427) was employed. This electronic barometer was powered by a Hewlett Packard power supply (Model E3612A) that was set to 28 V DC. This electronic barometer has a precision that is equivalent to that of the mercury barometer, and its voltage output could be read and stored by the data acquisition unit. The purpose of determining the atmospheric pressure was primarily to calculate the density of the air, which, in turn, was used in calculations of the air flow velocity, and the Reynolds number.

3.4.5 Air Velocity and Flow Rate Measurements

The velocity of the primary air flow was determined using a pitot-static tube. The dynamic pressure, which is the difference between the stagnation and static pressures, was measured using the Barocel and the procedures described in the subsection 3.4.3.

The flow rate of the secondary, or injection, air in the film-cooling studies was calculated using pitot and static pressure measurements in the flow-metering section of the secondary air-flow circuit (Fig. 11). The pitot tube was traversed across the cross-section of the acrylic flow-metering tube. The dynamic pressure at each location was measured using the Barocel, and the local velocity was calculated. The ten-point log-linear method [Ower and Pankhurst, 1966] was then used to obtain the flow rate of the secondary air.

It should be noted here that the ten-point log-linear process is a very accurate method for determining the secondary air flow rate, but it required a fair amount of time and manual attention because the traversing of the pitot tube was not automated in this work. It was, however, determined that by using a suitable calibration curve, the secondary air flow rate could be determined with sufficient accuracy from just one differential pressure measurement, with the pitot tube located at the center of the flow-metering tube. This procedure, which also allowed enhanced automation of the data acquisition and processing, was employed in the final experimental runs. It should also be noted that the density of the air in the flow-metering section was determined from the measured static pressure and temperature.

3.4.6 Turbulence Measurements

The turbulence intensities were measured using constant-temperature hot wire anemometry, in conjunction with the theoretical considerations discussed in Chapter 2.

A cross-wire (X-wire) probe, consisting of two tungsten wires 5 μm in diameter, made by Dantec (Model 9055 P 0511) was used in this work. In this probe, two wires are essentially perpendicular to one another in an X formation, with each wire have a length to diameter ratio of 450. The probe holder is bent at a right angle, so that the probe could be oriented with its axis parallel to the main flow. The probe was connected to two bridges (Dantec Model 56C01), by 5 m shielded cables. The output from the bridge was connected to a linearizer-amplifier (Dantec Model 55D10). The output of the linearizer was connected to a sample-and-hold data acquisition board, made by Keithley-Metrabyte (Model SSH-4). This sample-and-hold board is an enhancement unit that was attached to the Metrabyte DAS-20 data acquisition board. The purpose of this enhancement unit is to be able to read multiple channels at the same time. At the fastest sampling rate, the DAS-20 has a delay of the 10 microseconds between each reading, but with the SSH-4 unit the

delay between the readings of successive channel is reduced to 10 nanoseconds. The motivation for this increase in the rate of digital data acquisition was to ensure that the inferred velocity vector is based on measurements taken at essentially the same moment in time.

The acquisition of raw data from the X-wire probe presented some difficulties due to hardware limitations. To obtain a consistent turbulence reading, it was determined that the output voltage must be read for approximately ten seconds at a sampling rate of 33,000 readings per second per wire. This represents approximately 700,000 voltage readings, and requires over one megabyte of storage space. Conventional PC-based methods of acquiring data and storing it into arrays are inadequate for this rate and amount of data. Fortunately, this difficulty could be overcome by using a Keithley-Metrabyte software, named Streamer, which directs the flow of data directly onto the hard disk, or to the RAM of the computer, by bypassing the CPU. Streamer can do this at the sustained rate of the data acquisition board as long there is available memory in the storage device.

Once the hot-wire data was acquired, the computer was used to analyze the data, obtain the turbulence intensity of the primary flow, and store the information. This analysis was based on the theoretical considerations presented in Chapter 2. The raw data was then discarded, and the computer was freed to record more data. The reason for discarding the raw data was to manage the size of the files. It would be practically very difficult to store the data from many runs on one hard disk. A suitable data archiving facility, such a tape drive, is recommended if it is essential to store the raw data.

3.5 Calibration Procedures

3.5.1 Thermocouple Calibration

To obtain high accuracy in temperature measurements, each thermocouple was calibrated individually. The thermocouples were made from the same spool of wire, however, each of the thermocouples was kept on the same data acquisition channel during the experiment as it was during the calibration, because the thermocouples may exhibit slightly different responses in different channels. The calibration of the thermocouples was done by placing them in a controlled temperature environment, and recording their voltage outputs as well as the temperature of the environment.

To create a controlled and stable temperature environment, a constant-temperature liquid bath (Neslab Model RT-220) was used. This bath has a stability of $\pm 0.02^{\circ}\text{C}$, once steady-state conditions have been achieved, however, over a relative short period of time (in the order of minutes) the stability is in the order of $\pm 0.001^{\circ}\text{C}$. The thermocouples were first inserted into a copper block, so as to ensure that all the thermocouple sense the same temperature. To further assure the uniformity of the temperature sensed by each thermocouple, the copper block was placed in a beaker with an insulated bottom so that the turbulence of the liquid in the bath did not affect the copper block. A quartz thermometer (HP Model 2804A) was used to measure the temperature of the bath. This quartz thermometer has an accuracy of $\pm 0.005^{\circ}\text{C}$ (a calibration and certification of this device was done by NRC, Ottawa).

The entire calibration procedure was automatically managed by the main data acquisition system, for the range of temperature desired, using a program that was specifically written for this task. To control the bath temperature, the control circuit of the bath was modified so that its temperature was made proportional to an applied DC voltage. This

voltage was controlled by a programmable analog-output card installed in the main data acquisition unit. The computer calibration software first sets the bath to a desired temperature. To verify that steady-state has been achieved, the quartz thermometer readings are constantly recorded, until a chosen stability criteria is satisfied. The stability criterion used in this work was that the temperature over a five minute interval could not change more than $\pm 0.002^{\circ}\text{C}$. Once this condition was satisfied, all the thermocouple voltages were measured. To ensure the accuracy of the calibration procedure, the data was kept only if the temperature of the bath during this data acquiring stage did not vary by more than 0.001°C . This procedure was repeated in increments of 0.25°C in the bath temperature over the range of interest.

Once the calibration data was gathered, the computer program produced a least-squares polynomial fit for each individual thermocouple. The order of the polynomial began with a third-order fit, however, if the error of the polynomial was too large, the order was increased and the least-square fit was recalculated to a maximum of sixth order. After all the polynomials were determined, the coefficients were stored in a file along with the value of the absolute average error of each thermocouple. The data file containing these coefficients was made available to the main data acquisition software to determine the temperature from the measured thermocouple voltage in the final experimental runs.

3.5.2 Barocel Calibration

To calibrate the Barocel, a known differential pressure must be applied and the voltage output of the instrument has to be recorded, and ultimately correlated with the applied differential pressure. An Askania manometer was used for this task. The Askania manometer functions with distilled water, and its readings are in millimeters of water. The high- and low-pressure outlets of the Askania manometer were connected to the corresponding ports of the Barocel, thus it could be used to produce a differential

pressure. On the reference side of this circuit, a specially designed piston-tube device was used to add air in the reference tube, so as to ensure that the original reference water level was maintained.

The differential pressure range of interest in this experiment was from 0 to 100Pa, so the calibration was done from 0 to 10 mm of water. The procedure for the calibration was as follows: set the Askania manometer to the desired pressure difference; ensure that the reference water level is maintained, and if it is not, inject air until it is; record the voltage output of the Barocel by taking an average of sixty readings, and store this reading and also the value of the applied pressure; increase the differential pressure by 0.2 mm of water, and repeat the procedure until 10 mm of water. With the electronic solenoid valves and Barocel connected as described in section 3.4.3 the zero pressure voltage is measured before each pressure reading and subsequently subtracted from the reading. Once the corrected voltage reading is calculated, it is stored in a data file along with the value of the corresponding differential pressure. A least-squares procedure was used to fit a straight line through this data; it was ensured that this straight line passed through the origin or (0,0) point.

3.5.3 Hot Wire Calibration

Hot wire anemometry is a very sensitive measuring technique, and the X-wire probe and associated electronics required daily calibration.

The first step in the calibration process is to determine the cold resistance of the probe. The reason for determining this resistance is that the bridge must be set to balance this resistance of the probe. The probe's temperature (and thus its resistance) is dependent on the cooling effect of the air flow over it and the current flow in the wire. The purpose of the bridge is to respond to the change of cooling effect with a change in the current such

that the wire maintains a constant temperature. The balance in the bridge is set to a resistance value of 1.6 times the cold resistance, this is called the overheat ratio. This brings the operating temperature of the wire to approximately 250°C.

Once the correct resistance value is set for the bridge, the linearizer has to be adjusted. In this work, the linearizer was used only to amplify the signal, such that the output over the range of interest spanned the full limit of the data acquisition card, which is set from 0 to 10 volts. The gain of the linearizer was adjusted, such that at the maximum air flow speed, the output signal read close to 10 volts.

From this stage onwards, the entire calibration procedure was managed by a specially designed computer program written by the author. First, it instructs the computer to set the wind tunnel speed to a desired value. After a suitable period of time, making sure that the wind tunnel has achieved a prescribed stability criterion, the computer records, fifty times in succession, the velocity of the air flow in the tunnel, measured using a pitot-static tube and the Barocel, as well as the voltage signal registered by the hot wire anemometry system. As described in the hot wire theory in Chapter 2, Champagne's law [Champagne *et al.*, 1967a, 1967b] has been adopted in this study. The basic assumptions are that the turbulence in the flow does not affect the readings significantly, and that the wires are symmetric about the mean flow velocity vector. The turbulence intensity of the tunnel was under 1%, so that the assumption regarding the negligible effect of turbulence is valid. The assumption of the X-wire probe being symmetrical about the mean-flow velocity vector was verified by adjusting the orientation of the probe until the maximum value of the product of the two voltage outputs was obtained.

The signals from the X-wire probe can be processed to obtain velocity and turbulence data provided that the angle between the two wires is known. This angle was measured

by using an optical comparator. This device, in essence, projects a magnified shadow of the wires, thus allowing the use of a precise protractor to measure the desired angle with an accuracy up to fractions of a minute. The optical comparator was also useful to verify that the wires were straight, and free from any contamination.

The calibration software was used to collect a series of data points, by incrementing the wind tunnel speed and repeating the data acquisition procedure over the entire velocity range of interest. Once the data was collected, a polynomial of fourth order was fitted for each wire using the least-squares method. The coefficients were then stored in a data file for future access by the hot wire data acquisition program.

3.5.4 Electronic Barometer Calibration

The calibration of the electronic barometer (Vaisala Model PTA 427) involved simply recording, for a month, the daily atmospheric pressure using a Fortin-type mercury barometer and the corresponding voltage output of the electronic barometer. Once a sufficient number of data points, as well as a good range of pressure values, were obtained, the voltage signal of the electronic barometer was linearly correlated with the readings of mercury barometer. The correlation, obtained from the calibration, was excellent, with a difference of less than $\pm 0.1\%$ on any given day.

3.6 Computer Control

With the advent of powerful personal computers, as well as the computer - data acquisition interface, experiments have a potential of becoming more accurate and easy to carry out. The advantages of having a computer run and control the experiment is that the repeatability is improved, and manual input can be minimized. The advantages of having the data acquisition done by a computer is that the data recording can be done orders of magnitude faster than possible manually, while eliminating possible human

errors. One goal in designing the experiment was to involve the personal computer as much as reasonably possible. The task of the computer was divided into two parts: experimental control and data acquisition.

The components of the experiment which remained out of computer control are the level of turbulence intensity in the main stream flow, which required the grid in the wind tunnel to be changed manually; the flow rate of the secondary air, which was controlled by a butterfly-gate valve; and the heating elements of the secondary flow, that were controlled by manually setting electrical transformers.

3.6.1 Wind Tunnel Velocity Control

The primary air flow was controlled by varying the power supplied to the DC motor. The DC power was supplied by three Kepco power supplies (Model ATE 100-10M). Each of these power supplies could generate 1000 W of power, with a maximum of 100 V and 10 A. The three power supplies were connected in parallel, thus allowing a maximum current of 30 A. To control the DC voltage, Kepco has designed a 50 pin connector at the back of each unit, so the control circuitry of each unit can be interconnected. The configuration used is the master-slave parallel connection where one unit drives the subsequent units to mimic the voltage the master unit is delivering. The master unit can be set either manually, by adjusting the knob in the front of the unit or, as in this case, automatically by providing a 0-10 V control potential. The voltage output is linearly proportional to the control potential, and it can be approximately determined by multiplying the control voltage by ten.

The control voltage was supplied by the first of two analog channel outputs in the data acquisition card (Keithley Metrabyte DAS-20). By calling a DAS-20 computer language routine and passing the appropriate values, the equivalent voltage was set in the analog

channel. Once the voltage for a desired velocity was determined, the same voltage was used throughout the experiment to maintain consistency in the conditions of the experiment. It is important to note that the cross flow velocity used in the calculation of the Reynolds number was determined in each case by the dynamic pressure measurements and not the programmed voltage.

3.6.2 Heating Film Control

The thin-film heater was powered by two DC power supplies connected in a master-slave series configuration. The series configuration makes available to the heating film a total voltage of 200 V. The 'master' power supply was controlled by the second analog output channel of the DAS-20 data acquisition card.

The maximum temperature of the heating film had to be maintained below a tolerable value (in this case 80°C). The reason for this is that the heating film is delicate and can burnout if the temperature is too elevated. It was also necessary to maintain the desired differences in the temperatures of the main stream air, the surface of the model, and the injection air. To determine the corresponding heater power levels, a series of tests were done with no injection cooling. This way, the temperature of the surface is only dependent on the energy dissipated by the heater film, and the convection cooling caused by the primary air flow. Once the appropriate levels of heater power were determined for each primary flow velocity, exactly the same heater power was applied for each turbulence level investigated in this work.

3.7 Experimental Procedure

The experimental study was divided into three parts. The first part of the experiment investigated the turbulence characteristics of the wind tunnel without any turbulence generating grid, with a relative fine turbulence generating grid (referred to as Grid 1), and

with a coarse turbulence generating grid (referred to as Grid 2). In the second part of the experimental study, the heat transfer characteristics of the model without any secondary air flow were investigated. The model was subjected to the three different turbulence intensity levels investigated in the first part, and the Reynolds number of the primary air flow was varied from 23,000 to 75,000. Finally, in the third part, the film-cooling effectiveness of the model was investigated, under the same cross flow Reynolds numbers and turbulence intensities as those considered in the second part, and with the mass flux ratio varying from 0.5 to 2.0.

This section describes the procedures that were used to gather all the data. For each experiment, the equipment was turned on the night before to warm up, and remained on during the entire run, which sometimes lasted for days.

3.7.1 Procedure for the Investigation of Primary Flow Turbulence Intensity

Three different levels of turbulence intensities were employed in this study: the turbulence naturally produced by the wind tunnel; and turbulence produced by two different grids inserted in the wind tunnel upstream of the model blade. The grid-generated turbulence intensity, however, does not remain constant in the wind tunnel and in the test section. Therefore, in first part of this study, the turbulence intensity downstream of the grid location was investigated, with and without grids.

A series of turbulence intensity and mean velocity data were collected along the centerline of the wind tunnel ($Z/D=0.0$ and $Y/D=0.0$ in Fig. 3), starting just downstream of the grid until approximately one diameter of the model upstream of the stagnation line on the model. Another series of data were collected along a line located at $Z/D=0.0$ and $Y/D=1.7$ (Fig. 3) from just downstream of the grid until approximately $3D$ downstream of the leading edge of the model. And a final series of data were collected by varying the

height of the probe from the center of the tunnel to one eighth the height of the test section, along a central vertical line located $1.3D$ upstream of the leading edge of the model. Along the two horizontal lines, the data were collected at intervals of $D/2$ making for six locations along the centerline, and thirteen locations along the line at $Z/D=0.0$ and $Y/D=1.7D$. Note that during this entire experiment, the model blade was maintained in place.

At the beginning of each day, the hot wire probe was calibrated. Once the calibration was done, the wind tunnel speed was set and a particular grid was selected. The probe was placed in the appropriate position. With the computer constantly recording the voltage from the hot wires and displaying their product, the orientation of the probe was finely adjusted until that the mean velocity vector intersected the X-probe symmetrically. The air flow was then allowed to stabilize for fifteen minutes. At this point, the voltage signals from the probe were recorded as described earlier in this chapter.

Once the data were collected and stored, the voltages was converted into effective velocities, from which the instantaneous velocity vector was determined. The computer program then calculated the mean velocity and the turbulence intensity based on the theory presented in Chapter 2. This procedure was repeated for every location, wind tunnel speed, and turbulence grid condition.

The range of Reynolds number studied was from 23,000 to 75,000, at intervals of 10,000. Hot wire readings were taken at six positions along the centerline, thirteen positions along the line at $Z/D=0.0$ and $Y/D=1.7D$, and five positions along the vertical line. The experiment was done for the No Grid condition, as well as with Grid 1 and Grid 2.

3.7.2 Procedure for the Heat Transfer Experiment

The goal of this phase of this work was to obtain the distribution of the local heat transfer coefficient between the outer surface of the model and the primary air flow under different experimental conditions, *without* any secondary air injection. There were three variable parameters for this experiment: the Reynolds number based on the upstream velocity of the cross flow and the diameter, D , of the semicircular leading edge of the model blade ($Re = \rho_{\infty} u_{\infty} D / \mu_{\infty}$); the turbulence intensity level; and the power applied to the film heater. The Reynolds number was varied between 23,000 and 75,000, for each of the three different turbulence intensity levels. With the assumption of constant fluid properties, the heat transfer coefficient number is independent of the model surface temperature. The experiment was run with different film heater power levels in order to verify this assumption.

Once the experimental conditions were set, they were maintained for a period of four hours in order to reach steady-state conditions. Then the computer control system switched into a data acquiring mode. The software cycled through all the instruments and recorded their measurements fifty times. The data acquiring cycle was started by recording all the thermocouple voltage values. Then it registered the voltage output of the electronic barometer, the voltage and amperage applied to the heater film, the wind tunnel DC motor voltage, and the Barocel output related to the primary air flow. It took approximately five minutes to complete this data acquisition cycle. Once a particular data-acquisition cycle was completed, for each data point, the computer program stored the mean value of fifty readings along with the standard deviation. The standard deviation was used to verify the stability, consistency, and repeatability of each reading.

3.7.3 Experimental Procedure for the Investigation of Film Cooling Effectiveness

In the film cooling experiment, the cross flow temperature at a location 4D upstream of the model blade was maintained at T_∞ ($\cong 21^\circ\text{C}$). The temperature of the secondary flow within the plenum chamber of the model blade was T_s : $60^\circ\text{C} < T_s < 80^\circ\text{C}$. The model blade was unheated. In practice $T_\infty > T_s$, however, running the experiments with $T_\infty < T_s$ was more convenient in this work, and with the assumption of the constant fluid properties, the values of film cooling effectiveness, η , are unaffected.

The parameters for this part of the study were the Reynolds number of the primary air flow, the turbulence intensity level, and the ratio of the mass flux of the injected air to the mass flux of the primary air flow ($M = \rho_s U_s / \rho_\infty U_\infty$). The same data acquisition software was used as in the heat transfer experiment, with the additional recording of the secondary air flow rate, and the elimination of the section pertaining to the film heater power measurements.

At the beginning of each run, the upstream velocity of the primary air flow, and the mass flow rate of the secondary air flow were set. Once the two air flows were set, the secondary air heaters were adjusted so as to provide the desired injection air temperature. Following this, the computer program waited for four hours before it began its fifty recording cycles, as described in the heat transfer experimental procedure.

A series of five runs with the Reynolds number of the primary air flow varying from 23,000 to 75,000 was done for each level of turbulence intensity. The mass flux ratio in each of these runs was set to approximately one. Afterwards, a series of eight runs was executed with the no-grid condition, the primary air flow Reynolds number set at 50,000, and with the mass flux ratio varying from 0.5 to 2.0. A similar series of runs was done with Grid 2, with the primary flow Reynolds number at 50,000 and the mass flux ratio

varying from 0.5 to 2.0. Finally, a set of four runs at $Re=50,000$ with Grid 2, and the mass flux ratio set at 0.5 and 2.0 were done, to do a repeatability check of the previous results.

Chapter 4

RESULTS AND DISCUSSION

As was mentioned earlier, the experimental work was divided into three parts: (i) investigation of the turbulence intensity of the primary air flow, with and without turbulence generating grids; (ii) study of local heat transfer coefficients on the surface of the model blade *with no secondary flow*, under different values of primary flow Reynolds number and turbulence intensity; and (iii) study of the local film cooling effectiveness, for various values of primary flow Reynolds number, turbulence intensity levels, and mass flux ratios. The subsequent sections of this chapter are devoted to the presentation and discussion of the results obtained in each of these parts of the experimental work. The errors and repeatability of these results are discussed in Appendix B.

4.1 Turbulence Intensity of the Primary Air Flow

As was mentioned in Section 3.6.1, with respect to Fig. 3, a series of turbulence intensity data were collected along two horizontal lines (one located at $Z/D=0$ and $Y/D=0$; and the other at $Z/D=0$ and $Y/D=1.7$), and one vertical line (at $Z/D=0$ and $2D$ upstream of the leading edge of the model). Along the two horizontal lines, the data were measured at intervals of $D/2$, for a total of six locations along the line at $Z/D=0$ and $Y/D=0$, and thirteen locations along the line at $Z/D=0$ and $Y/D=1.7$. Data were obtained at five positions along the vertical line. These measurements were done for the no-grid conditions, as well as with Grid 1 and Grid 2.

The calibration of the X-probe was done daily in order to account for possible drift of the anemometer, and also the different turbulence intensities. The instantaneous velocity near the turbulence generating grid could fluctuate by as much as $\pm 50\%$ about the mean

velocity. The data acquisition card used in this work requires that the output of the hot wire anemometer be between 0 to 10 volts. So when taking velocity readings near the grids, the hot wires were calibrated so that the voltage reading, corresponding to the mean velocities, would be between 3 and 6 volts, rather than 2 to 9 volts when there was No grid. With this calibration of the X-probe for experiment with the turbulence-generating grids, the resolution of the velocity readings near the turbulence grids is only half of the resolution possible without the grids.

Since the X-probe can be only used to determine time-mean and fluctuating velocity components in the plane of the X wires, it was assumed that the contribution to the turbulence intensity of the velocity fluctuations in the Z direction is the same as the contribution of the velocity fluctuations in the Y direction. The validity of this assumption was verified by recording the turbulence intensity with the X-probe in the X-Y plane, as well as in the X-Z plane. The contribution to the turbulence intensity of the velocity fluctuations in the Y direction was within $\pm 10\%$ of that due to the velocity fluctuations in the Z direction. Since the contributions of the Y and Z direction velocity fluctuations to the turbulence intensity represent about 25% of the total value, for the cases considered in this work, the aforementioned assumption does not seriously affect the accuracy of the turbulence readings.

To verify the repeatability of the readings, several different sets of readings were obtained for each turbulence level. The results from these tests indicates very good repeatability of the readings for $X/D > 2$ from the grid. The various set of readings for each case were within $\pm 0.3\%$ of the mean values. Due to the high turbulence just downstream of the grid, repeatability deteriorates to $\pm 5\%$ for $0 < X/D < 2$.

The turbulence intensity readings were taken at different primary air flow Reynolds numbers in the range $23,000 < Re < 75,000$. However, it was found that the distribution of turbulence intensity in this range of Re barely changed: the difference are within the experimental error, therefore, the reported values could be considered to be independent of the primary air flow Reynolds number.

The axial velocity distribution along a vertical line, $1.3D$ upstream of the model, was measured at five different locations in between the center to the ceiling of the wind tunnel. This velocity distribution was found to be fairly uniform, with all the readings within 3% of the mean velocity. The variation could be attributed to the proximity of the probe to the model. As the air flow approaches the model, the air in the center of the wind tunnel begins to swerve upwards (or downwards) to pass over (or under) the model. Thus it was expected that the velocity would increase as the probe was traversed away from the center of the tunnel.

At a location about $2D$ downstream of the turbulence generating grid, the velocity measurements indicate an erratic behavior as is seen in Figs. 15 and 16. This behavior can be explained by the fact that the turbulence grids used in this study produce approximately 50% blockage, hence the mean velocity just downstream of the grid is not quite uniform. Since the turbulence intensity depends on the mean velocity, it would be expected that the turbulence intensity also behaves in this fashion.

Plot of TI vs X/D along the $Z/D=0$ and $Y/D=0$ line and the $Z/D=0$ and $Y/D=1.7$ line are given in Figs. 13 and 14, respectively. Often, the turbulence intensity is defined based on only the fluctuating velocity component in the mainstream direction [Baines and Peterson, 1951; Han and Young, 1988]. In order to facilitate the interpretation of the results of this work *vis-a-vis* related works in the literature, plots of $(\sqrt{u'^2}/\bar{U})$

corresponding to the results in Figs. 13 and 14, are given in Figs. 17 and 18, respectively. In the rest of this thesis, however, reference will only be made to turbulence intensity, TI , as defined in Eq. (34).

The turbulence intensity distribution depicted in Figs. 13 and 14 exhibit a behavior similar to that described by Baines and Peterson (1951). The turbulence intensity dies out relatively quickly downstream of the grid, from approximately 40% to less than 10% in a distance of $4D$ for both Grids 1 and 2, and it remains less than 1% throughout for the no-grid case. Furthermore the measured turbulence intensities are essentially independent of the location in the Y direction (Figs. 1 and 3); the variation of turbulence intensity is approximately the same at corresponding X/D points along the horizontal lines located at $Z/D=0$ and $Y/D=0$, and $Z/D=0$ and $Y/D=1.7$. A last point to note is that the turbulence intensity decays more quickly once the flow in the region over the model is accelerated because of the blockage of the model in the central region of the test section, as this acceleration of the flow leads to negative production of turbulence [Hinze, 1975].

4.2 Local Heat Transfer Coefficient on the Surface of the Model Blade Without Secondary Flow

As was mentioned earlier in this thesis, the heat transfer experiments were conducted *without* secondary injection. The values of cross flow Reynolds number, Re , investigated were in the range of 23,000 to 74,000. The influence of upstream turbulence intensity was studied by running the experiments with No grid, and also with Grids 1 and 2. The variations of turbulence intensity with nondimensional distance (X/D) from the position of the grid, along a horizontal straight line located at $Z/D=0.0$ and $Y/D=1.7$ (Figs. 1 and 2), are presented in Fig. 14. As was discussed in section 4.1, these distributions of

turbulence intensity were essentially insensitive to the cross flow Reynolds number, Re , for the cases considered in this work.

As was discussed in Chapter 2, the convective heat flux from the surface of the film to the cross flow of air ($q''_{conv|IT TRF}$) is obtained by suitably correcting the electrical power dissipated per unit area of the film (q''_H), according to Eq. (16). The corrections account for the radiative heat-flux lost from the surface of the model blade to the walls of the test section ($q''_{rad|IT TRF}$) and the conduction heat flux *into* the model blade, $q''_{cond|IT TRF}$. Typical distribution of $q''_{cond|IT TRF} / q''_H$ and $q''_{rad|IT TRF} / q''_H$, for the case of $Re=51,000$, No grid, is presented in Fig. 19. It was found that the values of $q''_{rad|IT TRF}$ were all less than 5% of q''_H . The values of $q''_{cond|IT TRF}$ were also rather small compared to q''_H over most of the model blade, except in the vicinity of $x/D=\pi/4$, the position at which the semicircular leading edge meets the flat after body, where $q''_{cond|IT TRF}$ could be as high as 40% of q''_H . The relatively large heat conduction correction in the vicinity of $x/D=\pi/4$ is required because the flow separates from the surface of the model blade in this region and, as a result, there are large temperature gradients within the wall of the blade. It is to be noted here that the use of classical fin theory to estimate $q''_{cond|IT TRF}$, as was discussed in Chapter 3, could be in error in the regions of high temperature gradients. A two-dimensional analysis of heat conduction within the wall of the model blade is needed to obtain accurate estimates of $q''_{cond|IT TRF}$.

The aforementioned correction scheme assumes that the heat conduction inside the wall of the model blade is quasi one-dimensional in the x direction ($T_w \cong T_w(x)$). In two distinct regions within each geometrically similar module of the model blade, however, this assumption is not quite correct. One of these region is located in the vicinity of $Z/D=0$ and $x/D=0.26$ (Figs. 1 and 2), where the injection tubes (plugged in the heat transfer experiment) are inserted into the wall of the model blade, thus invalidating,

locally, the assumption that $T_w \cong T_w(x)$: the effect of the injection tubes is manifested in the small bumps in the Nu vs x/D curves, in the vicinity of $x/D=0.26$, in Figs 20 to 23. The second region is encountered only with grid-generated turbulence, and it is located in the vicinity of $Z/D=0$ and $x/D>\pi/4$. In this region, the thermocouples in the wall of the model blade were *not* located along the $Z/D=0$ line, but were staggered about this line, in order to minimize the adverse effects of the insertion of the thermocouples. In the experiments with grid-generated turbulence, the mean velocity and turbulence intensity distributions behind the grid are not quite uniform in the Y-Z plane (Figs. 1 and 2), rather, they have a dimpled or rippled distribution in this plane. Thus the model blade temperature distribution is also slightly dimpled or rippled in the Z direction, about the $Z/D=0$ location. The conduction correction procedure used in this work ignores this rippled temperature distribution. Thus the Nu vs x/D curves in Figs 21 and 22, which correspond to cases run with Grids 1 and 2, respectively, exhibit a slightly rippled behavior for $x/D>\pi/4$.

The heat transfer results were cast in terms of a local Nusselt number, Nu, and a nondimensional temperature, Φ , defined in Eq. (19) in Chapter 2 (Tables 1 to 3). Distributions of Nusselt number (Nu) versus nondimensional distance along the blade (x/D) are given in Figs. 20, 21, and 22, for cases with No grid, Grid 1, and Grid 2, respectively. It should be noted that $x/D=0.0$ at the stagnation line on the model blade. A comparison of Nusselt numbers for low (No grid), medium (Grid 1), and high (Grid 2) values of turbulence intensity and Reynolds number of about 54,000 is presented in Fig. 23. Numerical values of the local nondimensional temperature, Φ , and Nusselt number, Nu, are presented in Tables. 1, 2, and 3, for the No grid, Grid 1 and Grid 2 cases, respectively.

The results in Figs. 20 to 23 show that for all cases, the boundary layer on the leading edge of the model blade separates from the surface at about $x/D=\pi/4$, which corresponds to the location where the semicircular leading edge meets the flat after body. This location of the separation point is different from that for a cylinder in *unconfined* cross flow, for which the laminar boundary layer separates at $x/D\cong 0.7$. For a fixed upstream turbulence intensity, the local Nusselt number increases with increasing Reynolds number, due to thinner boundary layers and more vigorous flow separation and reattachment. Furthermore, for fixed upstream turbulence intensity and Reynolds number, the Nusselt decreases from its stagnation point ($x/D=0$) value to a minimum at the location where the boundary layer separates, then increases sharply until the reattachment point on the flat after body, and decreases again downstream of the reattachment point. The results in Fig. 23 show that higher upstream turbulence intensity produces higher Nusselt numbers on the leading edge of the model blade, but downstream of the separation point, this trend is reversed. This indicates that higher upstream turbulence intensity diminishes the extent of the zone of separated flow and its influence on the heat transfer downstream of the separation point.

4.3 Film Cooling Effectiveness Results

The definition of the film cooling effectiveness, η , and the theoretical considerations that are necessary to determine it from the experimental measurements of temperature were presented in Chapter 2, section 2.2. As was discussed there, the η distribution can be calculated from the measured values of the model blade wall temperature, T_w , the upstream value of the primary flow temperature, T_∞ , and the secondary flow temperature, T_s . To do this, the adiabatic wall temperature, T_{aw} , has to be estimated from T_w by appropriately compensating, or correcting, for tangential and radial heat conduction in the wall of the blade, the convective heat transfer from the outer surface of the blade to the

fluid flow, and the radiative heat transfer from the outer surface of the blade to the walls of the test section. The procedures that were used to calculate these corrections were also discussed in Chapter 2.

The model blade surface temperature was measured by using fifty-five chromel-constantan (Type E) thermocouples. The data from the thermocouples yielded the values of T_w at the nodal locations of the triangular mesh shown in Fig. 8. In this figure, the horizontal line joining nodes 0 and 1 coincides with the stagnation line ($x/D=0$) on the model blade; and the horizontal line through node 33 is located at the position where the semicircular leading edge of the model blade meets the flat after body ($x/D=\pi/4$). The following notation is adopted in the rest of the section:

Line A: line through nodes 5, 15, 22, 29, 34, 37, 40, 43, 46, 49, and 52

Line B: line through nodes 2, 11, 19, and 26

Line C: line through nodes 0, 6, 16, 23, and 30

Line D: line through nodes 3, 20, 27, 33, 36, 39, 42, 45, 48, and 51

Line F: line through nodes 4, 12, 21, and 28

Line G: line through nodes 8, 18, 25, 32, 35, 38, 41, 44, 47, 50, and 53

As mentioned earlier, the values of η are obtained by correcting the values of η^* , in accordance with Eq. (10). For the particular case of $Re=52,100$, no turbulence grid, and mass flux ratio of 0.96, the variations of $q''_{cond_r}/h(T_s - T_\infty)$, $q''_{cond_N}/h(T_s - T_\infty)$, and $q''_{rad}/h(T_s - T_\infty)$ with x/D , along Line D for $x/D > \pi/6$, are presented in Fig. 25. As can be inferred from these results, the values of $q''_{cond_N}/h(T_s - T_\infty)$ are all less than 0.10, and values of $q''_{rad}/h(T_s - T_\infty)$ are all less than 0.05. However, the values of $q''_{cond_r}/h(T_s - T_\infty)$ can be as high as 0.25 in the vicinity of $x/D=\pi/6$. These results are representative of the corrections in the other cases considered in this study.

The value of η for the various cases considered in this study are presented in Tables 4 to 12. The injection tubes in this work were all normal to the surface of the model blade, in the X-Y plane (Fig. 1). Thus for the cases considered here, the film cooling takes place mostly directly downstream of the injection holes. Thus the η values in Tables 4 to 12 are the highest along Line D, and essentially negligible along Lines A, B, C, E, F, and G. It should also be noted that the η values are essentially symmetrical about Line D, within the experimental uncertainties discussed in Appendix B. Therefore, in the rest of the section, attention will be limited to the η values along Line D only.

The effect of the primary flow Reynolds number, Re , on η at three different levels of upstream turbulence intensity (with No grid, and with Grids 1 and 2), and a fixed value of mass flux ratio ($M \cong 1.0$) is illustrated in Figs. 26, 27, and 28. The η values presented in these figures correspond to the location of thermocouples #20, #36, and #45 along D in Fig. 8: thermocouple #20 is located immediately downstream of the injection hole; thermocouple #36 is the first thermocouple on the flat after body of the model blade (just after $x/D = \pi/4$); and thermocouple #45 is located downstream of the separation bubble on the flat after body with $[(x/D)_{\#45} - (x/D)_{\#36}] \cong [(x/D)_{\#36} - (x/D)_{\#20}]$. The results in Figs. 26, 27, and 28 show that η increases slightly, or stays essentially unchanged with increasing Re , for all cases considered here, except for $Re > 45,000$ with Grid 2, in which case η decreases slightly with Re . It is also observed that the η values at locations #36 and #45 are significantly lower than those at location #20: this is because the flow separation and reattachment phenomena causes the injected secondary flow to mix rapidly with the primary flow, with the consequent lowering of the film cooling effectiveness.

The influence of upstream turbulence intensity on η is clearly illustrated in Fig. 29, where the η distribution along Line D is presented for two cases: No grid, $Re=52,100$, and $M=1.29$; and Grid 2, $Re=55,200$, and $M=1.25$. It is seen that the values at low levels of turbulence intensity (No grid) are higher than those at the high levels of turbulence intensity (Grid 2). This result is to be expected because the rate of mixing of the secondary flow with the primary flow is more rapid at the high level of upstream turbulence intensity (Grid 2) than that at low levels of upstream turbulence intensity (No grid). Another observation is that the drop in η just beyond $x/D=\pi/4$ is higher for the No grid case than for the Grid 2 case: this is because the extent and effect of the flow separation zone are higher for the No grid case than those for the case with Grid 2. It is also interesting to note that the locations of the peak value of η for the two cases considered in Fig. 29 are not the same: this indicates that the behavior of the secondary flow jet immediately downstream of the injection hole for the No grid case is different from that for the case with Grid 2.

In summary, the results in Fig. 29 highlight the significant influence of upstream turbulence intensity on the fluid dynamics of the primary and secondary flows over the model blade, and, consequently, on the film cooling effectiveness.

The influence of mass flux ratio, M , on the film cooling effectiveness is illustrated in Figs. 30 and 31. The results in Fig. 30 pertain to the No grid case with a primary flow Reynolds number of $Re=52,100$. Results for the case with Grid 2 and $Re=39,200$ are presented in Fig. 31. In both these figures, the η distributions pertain to values along Line D (Fig. 8). It is clearly seen that for the range of parameters considered here, η decreases with increasing values of M . This might seem unusual because an increase in M , for a fixed primary flow Reynolds number, corresponds to an increase in the rate of the secondary, or cooling, air flow. However, in this work, the secondary flow is injected

at an angle that is normal to the surface of the model blade. Thus as M increases, for a fixed primary flow Re , the secondary flow jet penetrates further into and mixes more rapidly with the primary flow, leading to a decrease in the values of η .

Another interesting aspect of the results in Fig. 30, which pertains to the No grid case, is that the location of the peak value of η shifts away from the vicinity of the injection hole with increasing values of M , until it reaches $x/D=\pi/4$. This shows that the point at which the secondary flow reattaches to the surface of the blade, downstream of the injection hole with increasing values of x/D with increasing values of M , until it reaches $x/D=\pi/4$, where the semicircular leading edge meets the flat after body of the model blade.

A series of duplicate sets of runs was also done to check the repeatability of the experiments related to film cooling effectiveness. In each set of duplicate runs, all experimental conditions were maintained the same, as closely as possible. In some of these duplicate sets however, the temperature of the injected fluid was changed in order to verify the assumption that the fluid properties, and, hence, the film cooling effectiveness, were essentially independent to the temperatures, in the range of experimental conditions investigated in this study. In all cases, the repeatability of the results was excellent, well within the experimental uncertainties (Appendix B). The repeatability results for the case of $Re=39,200$, Grid 2, and $M=0.65$ are presented in Fig. 32, and are illustrative of the results obtained for the other cases considered in this study.

A final point to note is that in Fig. 30 and in Table 9, some values of η exceeded unity ($\eta>1$). This is physically impossible. The raw temperature data that correspond to these results showed no such difficulties: in all cases, it was found that $T_{\infty} \leq T_w \leq T_s$, and the values of η' were all less than unity. This suggests that at points where η exceeds unity, the error is in the corrections that were made to account for conduction within the wall of

the model blade, and for radiation from the surface of the model blade to the walls of the test section. As was mentioned earlier, fifty five thermocouples were used to measure values of T_w . The slight anomalies in the values of η , however, indicate that more values of T_w are required in order to obtain more accurate values of the corrections to the η^* values. It is also likely that the use of two-dimensional fin analysis in the calculation of q_{cond} , (as discussed in Chapter 3) is invalid in the regions of high temperature gradients. A full three-dimensional conduction analysis within the wall of the model blade is required to check this.

Chapter 5

CONCLUSIONS AND RECOMMENDATIONS

An experimental investigation of the influence of upstream turbulence on discrete-hole film cooling of a model blade in confined cross flow was presented and discussed in the earlier chapters of this thesis. The main contributions and possible extensions of this work are discussed concisely in this chapter.

5.1 Contributions of this work

The main contributions of this work are summarized in the following points:

- (i) A model blade for discrete-hole film cooling studies was designed and constructed. A schematic illustration of this blade is given in Fig. 1. The geometry of this blade is similar to that of model blades used by Bellows and Mayle (1986), Mehendale *et al.* (1991), and Saabas (1991). The discrete injection holes of this blade were designed so that they could be closed, if desired, by the use of specially designed plugs. Thus, experiments could be carried out with and without discrete-hole injection of a secondary fluid. The model blade was fitted with a total of 55 chromel-constantan (Type E) thermocouples for the measurement of the local wall temperature, T_w . A test section for mounting this model blade in a blower cascade wind tunnel was also designed and constructed. Schematic representations of the blower cascade wind tunnel and the test section, with the model blade mounted inside, are given in Figs. 2 and 3, respectively. Two turbulence generating grids were also designed and constructed, following the recommendations of Baines and Peterson (1951) and Mehendale *et al.* (1991). The test section was designed to facilitate the quick insertion and removal of these grids.

- (ii) A constant-temperature anemometer (CTA) system with a X-wire probe was implemented, tested, and then used for mean velocity and turbulence intensity measurements. A computer program was written to acquire and process the hot wire data. In addition, a special computer software, Streamer, developed by Keithley-Metrabyte was purchased, tested, and incorporated into the data acquisition procedure. This software allows direct storage of the hot wire data on the hard disk, or RAM, of the personal computer, at the sustained rate of the Metrabyte DAS-20 data acquisition board fitted with a Keithley-Metrabyte SSH-4 sample-and-hold unit. This implementation of Streamer was crucial in obtaining consistent and repeatable readings of turbulence intensity.

- (iii) In the heat transfer investigation, local heat transfer coefficients on the surface of the model blade were obtained by implementing a thin film technique developed earlier by Baughn *et al.* (1985, 1986), Hippensteele *et al.* (1985), Neill (1989), and Bernier (1991).

- (iv) A comprehensive microcomputer-based system for data acquisition, control, and processing was designed and implemented. The software to run this system was also developed and implemented as a part of this investigation.

- (v) The influence of upstream turbulence on heat transfer from the model blade *without* secondary air injection, and on film cooling with discrete-hole injection of secondary air was investigated for several combinations of cross flow Reynolds number, Re , and blowing ratio, M . The results of the heat transfer investigation were presented in terms of the local Nusselt number, Nu , and nondimensional temperature, Φ , distributions on the surface of the model blade. The results of the

film cooling study were presented in terms of the film cooling effectiveness, η , distributions.

The values of Nu reported in this thesis incorporate corrections to account for heat conduction within the wall of the model blade, and radiation heat transfer from the surface of the blade to the walls of the test section. The theoretical considerations on which these corrections are based were discussed in Chapter 2, and they are similar to those used by Neill (1989).

The values of film cooling effectiveness, η , reported in this thesis also incorporate corrections for heat conduction within the wall of the model blade, and radiation heat transfer from the surface of the blade to the walls of the test section. The radiation heat transfer was estimated using a procedure similar to that used by Neill (1989). The procedure to correct for conduction heat transfer, however, is an *extension* of the quasi one-dimensional procedures proposed earlier by Neill (1989), Mick and Mayle (1988), and Mehendale *et al.* (1991). In the proposed procedure, quasi two-dimensional heat conduction within the wall of the model blade is assumed, and the correction is estimated using ideas borrowed from the Control-Volume Finite Element Method (CVFEM) of Baliga and Patankar (1983, 1988).

The uncertainties involved in the reported values of the primary flow Reynolds number, Re , the turbulence intensity, TI , the mass flux ratio, M , the local Nusselt number, Nu , and the film cooling effectiveness, η , are discussed in Appendix B.

5.2 Suggestions for Improvements and Extensions

The experimental facilities that were designed and implemented in this work have proved useful, and the result reported in this thesis have been quite encouraging. However, during the course of this investigation and the writing of this thesis, it became clear that the experimental facilities and results of this work could be improved and extended. Some suggestions in this regard are presented in this section.

- (i) The geometry of the model blade used in this work (Fig. 1) was based on that of similar blades used by Bellows and Mayle (1986), Mehendale *et al.* (1991), and Saabas (1991). This geometry is convenient for modeling film cooling in the leading-edge region of turbine blades, or the so-called shower head film cooling schemes. However, the strong flow separation at the point where the semicircular leading edge meets the flat after body ($x / D = \pi/4$) exerts a dominating influence on the results, and it is not representative of the flow over blades in actual gas turbine engines. Thus, a model blade with geometry similar to that of an actual turbine blade, or similar to one of the NACA families of wing sections [Abbott and Von Doenhoff, 1959], may be more appropriate for extensions of this work.
- (ii) The heat conduction corrections that were necessary to obtain values of the film cooling effectiveness, η , involved considerable uncertainties. One way to reduce these uncertainties is to increase the number of thermocouples that are used to measure the values of T_w . However, with the geometry of the current model blade, or with other blade shapes with multiple injection holes, it would be very difficult and tedious to obtain accurate heat conduction corrections in the vicinity of the injection holes. Furthermore, with multiple injection holes fed by a plenum chamber located within a model blade, it is very difficult to prescribe, or measure

precisely, the conditions of the secondary flow (velocity, turbulence quantities, and temperature distributions) at the inlet of the injection holes. These difficulties, and the associated uncertainties they introduce, diminish the value of the corresponding experimental data as checks on numerical predictions.

In the context of the aforementioned difficulties, if the main objective is to obtain experimental data that is suitable for the testing of numerical predictions, it may be best to conduct experiments with primary flow in a rectangular duct with top and bottom walls shaped to resemble the concave and convex surface of a turbine blade, and secondary flow injected through a *single* hole fed by a straight tube that is long enough to ensure full developed flow conditions well upstream of the exit plane.

- (iii) As was mentioned earlier in this thesis, it is often assumed, as it was in this work, that values of the heat transfer coefficient obtained *without* secondary air injection are also applicable to corresponding situations *with* injection of secondary air. This assumption has been shown to be quite good in regions that are removed from the injection holes [Goldstein, 1971], but it could be of questionable validity in the vicinity of the injection holes. It is difficult to obtain accurate measurements of the heat transfer coefficient with injection, especially with model blades that have multiple injection holes and house a plenum chamber for the secondary air. One way around this difficulty is to obtain accurate experimental data with a single injection hole in ducts with convex and concave walls, as discussed in the previous paragraph, use this data to fine-tune appropriate mathematical models and numerical simulations of the flow, and then use the numerical model to simulate the more complex geometries and multiple injection holes encountered in practice.

Another option is to use the naphthalene ablation technique [Sparrow, 1979] to obtain values of the local heat transfer coefficient with injection of the secondary fluid. If only the film cooling effectiveness is required, techniques based on foreign gas injection, gas chromatography, and the heat/mass transfer analogy would be useful [Salcudean *et al.*, 1994].

- (iv) The experimental facilities developed in this work could be used for investigations of the effects of the shape of the injection holes and the orientation of the injection tubes, with respect to the angle they make with the surface of the blade *and* the primary flow direction, on the film cooling effectiveness.
- (v) Improvements in the experimental facilities developed in this work could include automation of the measurement and control of the secondary air flow, turbulence measurements with three-wire probes, and an automatic system for planar traverses of the hot-wire probe.
- (vi) From a practical point of view, it would be very useful to conduct film cooling studies with compressible flow effects, transonic flow conditions, significant differences in the densities of the primary and secondary fluids, and large temperature differences. Facilities for such studies do not exist at McGill University, and it would be difficult and expensive to develop such facilities from scratch. Thus, it is suggested that studies of this type be carried out in collaboration with interested industries, such as Pratt and Whitney, Canada, Ltd., or government laboratories, such as the National Research Council in Ottawa.

In conclusion, the author of this thesis hopes that this work will facilitate and motivate at least some of the improvements and extensions suggested in this section.

REFERENCES:

1. Abbott, I.H., Von Doenhoff, A.E., *Theory of Wing Sections*, Dover Publications Inc., New York, 1959.
2. Abramovich, G.N., *Theory of Turbulent Jets*, MIT Press, Cambridge, Mass., 1963.
3. Alekseyev, N.M., Zelengur, A.A., Heat Transfer in and Efficiency of a Cooling Film Injected Through a Circular Hole, *Heat Transfer - Soviet Research*, Vol. 18, No. 6, pp. 63-68, 1986.
4. Andreopoulos, J., Rodi, W., Experimental Investigation of Jets in a Crossflow, *Journal of Fluid Mechanics*, Vol. 138, pp. 93-127, 1984.
5. Baines, W.D., Peterson, E.G., An Investigation of Flow Through Screens, *Transactions of the ASME*, Vol. 73, pp. 467-480, 1951.
6. Baliga, B. R., Patankar, S.V., A Control Volume Finite Element Method for Two-Dimensional Fluid Flow and Heat Transfer, *Numerical Heat Transfer*, Vol. 6, pp. 245-261, 1983.
7. Baliga, B.R., Patankar, S.V., Elliptical Systems: Finite-Element Method II, *Handbook of Numerical Heat Transfer*, Chapter 11, pp. 421-461, 1988.
8. Batchelor, G.K., *An Introduction to Fluid Dynamics*, Cambridge University Press, 1974.
9. Baughn, J.W., Elderkin, M.J., McKillop, A.A., Heat Transfer From a Single Cylinder, Cylinders in Tandem, and Cylinders in the Entrance Region of a Tube Bank with a Uniform Heat Flux, *Journal of Heat Transfer*, Vol. 108, pp. 386-391, 1986.
10. Baughn, J.W., Takahashi, R.K., Hoffman, M.A., McKillop, A.A., Local Heat Transfer Measurements Using an Electrically Heated Thin Gold-Coated Plastic Sheet, *Journal of Heat Transfer*, Vol. 107, pp. 953-959, 1985.
11. Bellows, W.J., Mayle, R.E., Heat Transfer Downstream of Leading Edge Separation Bubble, *Journal of Turbomachinery*, Vol. 108, pp. 131-136, 1986.
12. Bernier, M.A., *Investigation of a Closed-Loop Thermosyphon*, Ph. D. Thesis, Department of Mechanical Engineering, McGill University, 1991.

13. Bernier, M.A., Baliga, B.R., Visualization of Upward Mixed-Convection Flows in Vertical Pipes Using a Thin Semitransparent Gold-Film Heater Ad Dye Section, *Int. J. Heat and Fluid Flow*, Vol. 13, No. 3, pp. 241-249, 1992.
14. Bradshaw, P., *An Introduction to Turbulence and its Measurement*, Pergamon Press, Oxford, 1971.
15. Bradshaw, P., Johnson, R.F., *Turbulence Measurements and Hot Wire Anemometers*, Notes on Applied Science No. 33, 1963.
16. Camci, C., Arts, T., An Experimental Convective Heat Transfer Investigation Around a Film-Cooled Gas Turbine Blade, *Journal of Turbomachinery*, Vol. 112, pp. 497-503, 1990.
17. Camci, C., Kim, K., Hippensteele, S.A., Poinsatte, P.E., Evaluation of a Hue Capturing Based Transient Liquid Crystal Method for High-Resolution Mapping of Convective Heat Transfer on Curved Surfaces, *Journal of Heat Transfer*, Vol. 115, pp. 311-318, 1993.
18. Champagne, F.H., Sleicher, C.A., Wehrmann, O.H., Turbulence Measurements With Inclined Hot-Wires: Part 1. Heat Transfer Experiments With Inclined Hot-Wire, *Journal of Fluid Mechanics*, Vol. 28, part 1, pp. 153-175, 1967a.
19. Champagne, F.H., Sleicher, C.A., Turbulence Measurements with Inclined Hot-Wires: Part 2. Hot-Wire Response Equations, *Journal Fluid Mechanics*, Vol. 28, part 1, pp.177-182, 1967b.
20. Chassaing, J.G., Claria, A., Sananes, F., Physical Characteristics of Subsonic Jets in a Cross-Stream, *Journal of Fluid Mechanics*, Vol. 62, Part 1, pp. 41-64, 1974.
21. Crabb, D., Durao, D.F.G., Whitelaw, J.H., A Round Jet Normal to a Crossflow, *Journal of Fluids Engineering*, Vol. 103, pp. 142-153, 1981.
22. Dini, S., Simultaneous uses of Temperature Sensitive and Liquid Crystal Coatings to Measure Heat Transfer Coefficients, *Proceedings of the 32nd Heat Transfer and Fluid Mechanics Institute*, pp. 253-263, 1991.
23. Eckert, E.R.G., Drake, Jr., R.M., *Analysis of Heat and Mass Transfer*, McGraw-Hill Book Company, New York, 1972.
24. Eckert, E.R.G., Goldstein, R.J., *Measurements in Heat Transfer*, 2nd ed., Hemisphere Publishing Corporation, Washington, D.C., 1976.

25. Fergason, J.L., Liquid Crystals, *Scientific American*, Vol. 211, No. 2, pp. 765-85, 1964.
26. Foster, N.W., Lampard, D., The Flow and Film Cooling Effectiveness Following Injection Through a Row of Holes, *Journal of Engineering for Power*, Vol. 102, pp. 584-588, 1980.
27. Gartshore, I.S., Newman, B.G., The Turbulent Wall Jet in an Arbitrary Pressure Gradient, *Aeronautical Quarterly*, Vol. 20, p.25, 1969.
28. Gerald, C.F., *Applied Numerical Analysis*, 2nd ed., Addison-Wesley, 1978.
29. Goldstein, R. J., Film Cooling, *Advances in Heat Transfer*, Vol. 7, pp. 321-377, 1971.
30. Han, J.C., Young, C.D., The Influence of Jet-Grid Turbulence on Turbulent Boundary Layer Flow and Heat Transfer, *Transport Phenomena in Turbulent Flows*, Hemisphere Publishing Corporation, New York, pp. 501-514, 1988.
31. Hancock, P.E., Bradshaw, P., The Effect of Free-Stream Turbulence on Turbulent Boundary Layers, *Journal of Fluids Engineering*, Vol. 105, pp. 284-289, 1983.
32. Hanjalic, K., Advanced Turbulence Closure Models: A View of Current Status and Future Prospects, *Int. J. Heat and Fluid Flow*, Vol. 15, pp. 178-203, 1994
33. Hartnett, J.P., Irvine, Jr., T.F., *Advances in Heat Transfer*, Vols. 1-24, 1964-94.
34. Hewlett Packard Application Note 290, *Practical Temperature Measurements*, 1993.
35. Hippensteele, S.A., Russell, L.M., Torres, F.J., Local Heat Transfer Measurements on a Large-Scale Model Turbine Blade Airfoil Using a Composite of a Heater Element and Liquid Crystals, *Journal of Engineering for Gas Turbine and Power*, Vol. 107, pp. 953-960, 1985.
36. Hinze, J.O., *Turbulence*, 2nd ed., McGraw-Hill Book Co., 1975.
37. Holman, J.P., *Heat Transfer*, 6th edition, McGraw-Hill Book Company, 1986.
38. Honami, S., Shizawa, T., Uchiyama, A., Behavior of the Laterally Injected Jet in Film Cooling: Measurements of Surface Temperature and

- Velocity/Temperature Field Within the Jet, *Journal of Turbomachinery*, Vol. 116, No. 1, pp. 106-112, 1994.
39. Incropera, F.P., Dewitt, D.P., *Fundamentals of Heat and Mass Transfer*, 2nd ed., J. Wileys and Sons, New York, 1985.
 40. Ito, S., Goldstein, R.J., Eckert, E.R.G., Film Cooling of a Gas Turbine, *Journal of Engineering for Power*, Vol. 100, pp. 476-481, 1978.
 41. Jabbari, M.Y., Goldstein, R.J., Adiabatic Wall Temperature and Heat Transfer Downstream of Injection Through Two Rows of Holes, *ASME Publication*, No.77-GT-50, 1977.
 42. John, J., Schobeiri, T., A Simple and Accurate Method of Calibrating X-Probes, *Journal of Fluids Engineering*, Vol. 115, pp. 148-152, 1993.
 43. Kadotani, K., Goldstein., On the Nature of Jets Entering a Turbulent Flow Part B-Film Cooling Performance, *Journal of Engineering for Power*, Vol. 101, pp. 466-470, 1979.
 44. Kasagi, N., Hirata, M., Full-Coverage Film Cooling on Curved Walls, Part 3. Cooling Effectiveness on Concave and Convex Walls, *Heat Transfer - Japanese Research*, Vol. 18, n2, pp. 28-42, 1989.
 45. Kasagi, N., Hirata, M., Ikeyama, M., Effects of the Wall Curvature on the Full-coverage Film Cooling Effectiveness, *Heat Transfer and Fluid Flow in Rotating Machinery (1st International Symposium on Transport Phenomena)*, pp. 103-112, 1987.
 46. Kays, W.M., Crawford, M.E., *Convection Heat and Mass Transfer*, 3rd ed., McGraw-Hill Book Co., 1993.
 47. Keffer, J.F., Baines, W.D., The Round Turbulent Jet in a Cross Wind, *Journal of Fluid Mechanics*, Vol. 15, pp. 481-497, 1963.
 48. Kikkawa, S., Hayashida, M., Heat Transfer From a Two-Dimensional Film Cooled Gas Turbine Blade, *Heat Transfer - Japanese Research*, Vol. 16, No. 1, pp. 49-71, 1987a.
 49. Kikkawa, S., Iwasaki, Y., Experimental Investigation on Film Cooling of a Gas Turbine Cascade, *Heat Transfer - Japanese Research*, Vol. 13, No. 2, pp. 30-44, 1985.
 50. Kikkawa, S., Nakanishi, K., Experimental Investigation on Film Cooling of a Pressure Surface of a Gas Turbine Blade, *Heat Transfer and Fluid Flow in*

- Rotating Machinery (1st International Symposium on Transport Phenomena)*, pp. 27-36, 1987b.
51. Kikkawa, S., Okui, Y., Film Cooling of the Suction Surface of a Gas Turbine Blade with Three-Dimensional Injection, *Heat Transfer - Japanese Research*, Vol. 17, No. 5, pp. 1-16, 1988.
 52. Kikkawa, S., Sakaguchi, K., Experimental Investigation of Film Cooling on the Suction Surface of a Gas Turbine Blade and a Trial Application of Full Coverage Film Cooling, *Heat Transfer - Japanese Research*, Vol. 19, No. 5, pp. 455-473, 1990.
 53. Krishnamoorthy, V., Effect of Turbulence on the Heat Transfer in a Laminar and Turbulent Boundary Layer over a Gas Turbine Blade, *ASME Publication*, 82-GT-146, 1982.
 54. Launder, B.E., On the Computation of Convective Heat Transfer in Complex Turbulent Flows, *Journal of Heat Transfer*, Vol. 110, pp. 1112-1128, 1988.
 55. Lee, S.W., Lee J.S., Ro, S.T., Experimental Study on the Flow Characteristics of Streamwise Inclined Jets in Crossflow on a Flat Plate, *Journal of Turbomachinery*, Vol. 116, No. 1, pp.97-105, 1994.
 56. Lofdahl, L., *Basic Hot-Wire Technique*, Department of Applied Thermodynamics and Fluid Mechanics Lecture series April 22-23, Chalmers University of Technology, 1985.
 57. Lomas, C.G., *Fundamentals of Hot Wire Anemometry*, Cambridge University Press, 1986.
 58. MacAdams, W.H., *Heat Transmission*, 3rd. ed., McGraw-Hill Book Company, New York, 1954.
 59. Mayle, R.E., Anderson A., Velocity and Temperature Profiles for Stagnation Film Cooling, *Journal of Turbomachinery*, Vol. 113, pp. 457-463, 1991.
 60. Mayle, R.E., Kopper, F.C., Blair, M.F., Bailey, D.A., Effect of Streamline Curvature on Film Cooling, *ASME Publication*, 76-GT-90, 1976.
 61. McBrien, R.K., *Fully Developed Turbulent Flow in Rectangular Interrupted-Plate Ducts*, Ph. D. Thesis, Dept. of Mech. Eng., McGill University, 1989.
 62. Mehendale, A.B., Han, J.C., Influence of High Mainstream Turbulence on Leading Edge Film Cooling Heat Transfer, *Journal of Turbomachinery*, Vol. 114, pp.707-715, 1992a.

63. Mehendale, A.B., Han, J.C., Influence of High Mainstream Turbulence on Leading Edge Film Cooling Heat Transfer: Effect of Film Hole Spacing, *Int. J. Heat Mass Transfer*, Vol. 35, No. 10, pp. 2593-2604, 1992b.
64. Mehendale, A.B., Han, J.C., Ou, S., Influence of High Mainstream Turbulence on Leading Edge Heat Transfer, *Journal of Heat Transfer*, Vol. 113, pp. 843-850, 1991.
65. Mick, W.J., Mayle, R.E., Stagnation Film Cooling and Heat Transfer, Including Its Effect Within the Hole Pattern, *Journal of Turbomachinery*, Vol. 110, pp. 66-72, 1988.
66. Modest, M.F., *Radiative Heat Transfer*, McGraw-Hill Book Company, New York, 1993.
67. Mujumdar, A.S., *The Effect of Free-Stream Turbulence on Heat Transfer from Cylinders in Cross-Flow*, Ph. D. Thesis, Dept. of Chem. Eng., McGill University, 1971.
68. Neill, W.S., *Local Natural Convection Heat Transfer Measurements Using a Thin Gold-Film Technique*, M. Eng. Thesis, Dept. of Mech. Eng., McGill University, 1989.
69. O'Brien, J.E. and VanFossen, G.J., The Influence of Jet-Grid Turbulence on Heat Transfer From the Stagnation Region of a Cylinder in Crossflow, *ASME Publication*, 85-HT-58, 1986.
70. Ou, S., Han, J.C., Influence of Mainstream Turbulence on Leading Edge Film Cooling Heat Transfer Through Two Rows of Inclined Film Shots, *Journal of Turbomachinery*, Vol. 114, pp. 724-733, 1992.
71. Ou, S., Mehendale, A.B., Han, J.C., Influence of High Mainstream Turbulence on Leading Edge Film Cooling Heat Transfer: Effect of Film Hole Row Location, *Journal of Turbomachinery*, Vol. 114, pp. 716-723, 1992.
72. Ower, E., Pankhurst, R.C., *The Measurements of Air Flow*, 4th ed., Pergamon Press, 1966.
73. Patankar, S.V., *Numerical Heat Transfer and Fluid Flow*, Hemisphere Publishing Corporation, 1980.
74. Paxson, D.E., Mayle, R.E., The Influence of a Mainstream Thermal Boundary Layer on Film Effectiveness, *ASME Publication*, 88-GT-17, 1988.

75. Perry, A.E., *Hot-Wire Anemometry*, Clarendon Press, Oxford, 1982.
76. Raithby, G.D., Eckert, E.R., The Effects of Turbulence Parameters and Support Position on the Heat Transfer From Spheres, *Int. Journal of Heat and Mass Transfer*, Vol. 11, pp. 1233-1252, 1968.
77. Rohsenow, W.M., Hartnett, J.P., *Handbook of Heat Transfer*, McGraw-Hill Book Company, 1973.
78. Saabas, H.J., *A Control Volume Finite Element Method for Three-Dimensional, Incompressible, Viscous Fluid Flow*, Ph. D. Thesis, Dept. of Mech. Eng., McGill University, 1991.
79. Salcudean, M., Gartshore, I., Zhang, K., McLean, I., An Experimental Study of Film Cooling Effectiveness Near the Leading Edge of a Turbine Blade, *Journal of Turbomachinery*, Vol. 116, No. 1, pp. 71-79, 1994.
80. Schlichting, H., *Boundary-Layer Theory*, 7th ed., McGraw-Hill Book Company, 1987.
81. Schwarz, S.G., Goldstein, R.J., The Two-Dimensional Behavior of Film Cooling Jets on Concave Surfaces, *Journal of Turbomachinery*, Vol. 111, pp. 124-130, 1989.
82. Schwarz, S.G., Goldstein, R.J., Eckert E.R.G., The Influence of Curvature on Film Cooling Performance, *Journal of Turbomachinery*, Vol. 113, pp. 472-478, 1991.
83. Seigel, R., Howell, J.R., *Thermal Radiation Heat Transfer*, 2nd. ed., Hemisphere Publishing Corporation, New York, 1981.
84. Shaw, R., The influence of hole dimensions on static pressure measurements, *Journal of Fluid Mechanics*, Vol. 7, pp. 550-564, 1960.
85. Simonich, J.C., Bradshaw, P., Effect of Free-Stream Turbulence on Heat Transfer Through a Turbulent Boundary Layer, *Journal of Heat Transfer*, Vol. 100, pp. 671-677, 1978.
86. Simonich, J.C., Moffat, R.J., New Technique for Mapping Heat-Transfer Coefficient Contours, *Review Scientific Instrumentation*, Vol. 53, pp. 678-683, 1982.
87. Simonich, J.C., Moffat, R.J., Liquid Crystal Visualization of Surface Heat Transfer on a Concavely Curved Turbulent Boundary Layer, *J. Engineering for Gas Turbine for Power*, Vol. 106, pp. 619-627, 1984.

88. Launder, B.E., Spalding, D.B., The Numerical Computation of Turbulent Flows, *Computer Methods in Applied Mechanics and Engineering*, Vol. 3, pp. 269-289, 1974.
89. Sparrow, E.M., Heat Transfer in Complex Duct Flows, *Studies in Heat Transfer*, pp. 273-295, Hemisphere Publishing Corporation, New York, 1979.
90. Tennekes, H., Lumley, J.L., *A First Course in Turbulence*, The MIT Press, Cambridge, 1972.
91. Thomann, H., Effect of streamwise wall curvature on heat transfer in a turbulent boundary layer, *Journal Fluid Mechanics*, Vol. 33, part 2, pp. 283-292, 1968.
92. TSI Fluid Mechanics Note TB 5, *Hot Film and Hot Wire Anemometry Theory and Application*, 1993.
93. Wadia, A.R., Nealy, D.A., Experimental Simulation of Turbine Airfoil Leading Edge Film Cooling, *Journal of Turbomachinery*, Vol. 110, pp. 226-232, 1988.
94. Wagnanski, I., Gartshore, I.S., *General Description and Calibration of the McGill 17 in. x 30 in. Blower Cascade Wind Tunnel*, Mechanical Engineering Research Lab T. N. 63-7, McGill University, 1963.
95. Wagnanski, I., Newman, B.G., The Reattachment of an Inclined Two Dimensional Jet to a Flat Surface in Streaming Flow, *CASI Transactions*, Vol. 1, No. 1, 1968.
96. Zuhkavkas, A., Heat Transfer from Tubes in Crossflow, *Advances in Heat Transfer*, Vol. 8, pp 93-160, 1972.

Appendix A

Hot Wire Data Reduction Procedure

The following analysis indicates how the raw hot wire data were reduced to mean velocity, as well as instantaneous velocity components. In Fig. 10, the coordinate system and the various variables used in this derivation are shown.

It is assumed that Champagne's law (1967a) is applicable in this case.

$$\begin{aligned}U_{e1}^2 &= U_{n1}^2 + k^2 U_{l1}^2 \\U_{e2}^2 &= U_{n2}^2 + k^2 U_{l2}^2\end{aligned}\tag{A1}$$

where

$$\begin{aligned}U_{n1} &= U \sin \theta & U_{l1} &= U \cos \theta \\U_{n2} &= U \sin(\varphi - \theta) & U_{l2} &= U \cos(\varphi - \theta)\end{aligned}\tag{A2}$$

The subscripts n and l refer to the directions normal and along the hot wire respectively, and the subscript e indicates the effective velocity felt by the wire. By substituting Eq. (A2) into Eq. (A1), the effective velocity on each wire becomes:

$$\begin{aligned}U_{e1}^2 &= U^2 \sin^2 \theta + k^2 U^2 \cos^2 \theta \\U_{e2}^2 &= U^2 \sin^2(\varphi - \theta) + k^2 U^2 \cos^2(\varphi - \theta)\end{aligned}\tag{A3}$$

By manipulating Eq. (A3) for Wire #1, the instantaneous velocity can be determined as follows:

$$U^2 = U_{e1}^2 / (\sin^2 \theta + k^2 \cos^2 \theta) \quad (A4)$$

To calculate the instantaneous velocity, as shown in Eq. (A4), the values of U_{e1} , θ , and k must be known. The value of k is dependent on the aspect ratio of the wire [Champagne *et al.* 1967a] and was determined to be $k=0.1$ for the X-wire probe ($l/d=450$) used in this thesis. The value of U_{e1} was obtained from the data gathered in the data acquisition process. To determine θ , the Eq. (A3) has to be manipulated such that the effective velocity for Wire #2, is divided by the effective velocity of Wire #1, as follows:

$$\frac{U_{e2}^2}{U_{e1}^2} = \frac{U^2 \sin^2(\varphi - \theta) + k^2 U^2 \cos^2(\varphi - \theta)}{U^2 \sin^2 \theta + k^2 U^2 \cos^2 \theta} \quad (A5)$$

With further simplification, Eq. (A5) becomes:

$$\frac{U_{e2}^2}{U_{e1}^2} = \frac{\sin^2(\varphi - \theta) + k^2 [1 - \sin^2(\varphi - \theta)]}{\sin^2 \theta + k^2 [1 - \sin^2 \theta]} \quad (A6)$$

or

$$\frac{U_{e2}^2}{U_{e1}^2} = \frac{\sin^2(\varphi - \theta) \cdot (1 - k^2) + k^2}{\sin^2 \theta \cdot (1 - k^2) + k^2} \quad (A7)$$

Eq. (A7) only contains one unknown, θ . However, Eq. (A7) is not linear, therefore to determine θ an iterative method is required. In this thesis, the secant method [Gerald, 1978] was used. Once the angle θ was determined, the instantaneous velocity vector, U ,

can be determined using Eq. (A4). The final step in the data reduction was to determine the velocity components in the X and Y directions, as follows:

$$\begin{aligned}u &= U \cos[(\varphi/2) - \theta] \\v &= U \sin[(\varphi/2) - \theta]\end{aligned}\tag{A8}$$

With the instantaneous velocity, and its components, the mean velocity and the turbulence intensity can be determined, as described in Chapter 2.

Appendix B

Error Analysis

The turbulence intensity, velocity, temperature, voltage, electrical power, mass flux ratios, and pressure measurements reported in this thesis are all affected by uncertainties that are intrinsic to the instruments used in this work. Furthermore, the values of Nusselt number reported in the heat transfer studies, and the values of effectiveness obtained in the film cooling investigation are affected by inaccuracies in the correction procedures described in Chapter 2.

Voltage Measurements

The voltage output of the thermocouples, the Barocel differential pressure transducer, and the Vaisala electronic barometer were measured using the HP Model 3494A data acquisition unit. This unit is equipped with a digital voltmeter (DVM) that has a 5½ digit readout with a resolution of 1μV, and is capable of reading voltages to an accuracy of ±3 μV in the 0-0.1 V range.

The voltage output of the constant-temperature hot-wire system (X probe, CTA bridges, linearizer/amplifier) was read using a DAS-20 data acquisition card manufactured by Keithley Metrabyte. This card has a 12 bit resolution and a ±3 bit count accuracy, which translates to ±7mV accuracy for the 0-10V range.

Temperature Measurements

The chromel-constantan (Type E) thermocouples were very carefully calibrated against a high-accuracy quartz thermometer (HP Model 2804A with a Model 18111A probe), which, in turn, was calibrated by the Physic Division of the National Research Council,

Ottawa, and certified to be accurate to within $\pm 0.005^{\circ}\text{C}$, in the range of 0°C to 95°C range. As was mentioned earlier, the voltage outputs of the thermocouples were fed to a thermocouple multiplexor card, with internal zero-reference temperature compensation, and read using the DVM of the HP 3497A data acquisition unit. Numerous calibration runs indicated that this setup allows temperature measurements with an accuracy of $\pm 0.05^{\circ}\text{C}$ or better, in the range of interest (15°C to 95°C). These accuracy estimates are consistent with those established for similar systems by Bernier (1991).

Differential Pressure Measurements

Differential pressure values were measured using the Barocel capacitance type transducer. The voltage output of the Barocel was measured using the DVM of the HP 3497A data acquisition unit. Procedures used to compensate for zero drift and to time average multiple readings for the same data point were discussed in Chapter 3.

Numerous calibrations of this system, against an Askania manometer, revealed that the differential pressure measurements in this work were accurate to within $\pm 0.05\text{Pa}$. This estimate is consistent with those obtained by McBrien (1989).

Atmospheric Pressure Measurements

Atmospheric pressure was measured using the Vaisala electronic manometer. The voltage output of this manometer was measured using the DVM of the HP 3497A data acquisition unit. This system was calibrated against a high accuracy mercury-in-glass Fortin type barometer. Based on these calibrations, it was established that the accuracy of the atmospheric measurements in this work was $\pm 0.1\%$.

Electric Power Measurements

Electric power to the thin-film heater, in the heat transfer experiments, was obtained by measuring the total current flow through the heater, and the voltage drop across the film.

The current, I , was measured using a HP 3478A multimeter, to an accuracy of $\pm 30\mu\text{A}$. The voltage drop measurements had an uncertainty of $\pm 0.1\%$. Based on these uncertainties, the error in the measured values of the total electrical power input to the film heater were estimated to be all less than $\pm 0.2\%$ of the reported values.

Measurements of the electrical resistance of the thin film heater yielded a value of $62\ \Omega$ /sq to within $\pm 4\%$. When this uncertainty is combined with the uncertainties in the values of I and V , the calculated values of ohmic power dissipation per unit area of the film heater ($q_H'' = V \cdot I / A_H$) can be considered accurate to within $\pm 5\%$ or better.

Time-Mean Velocity Measurements

The time-mean velocity measurements in the test section upstream of the model blade were obtained using a pitot-static tube, and the Barocel for measuring the corresponding dynamic pressure. The density of the air at the measurement location was estimated using the measured values of the temperature, T_∞ , and the corresponding absolute static pressure. Based on the aforementioned estimates of uncertainties in temperature, atmospheric pressure, differential pressure, and voltage measurements, and the intrinsic error of the pitot-static tube, it was estimated that the time-mean velocity measurements were accurate to within ± 0.02 m/s. This estimate, and additional compensation to account for flow turbulence, translates to a maximum uncertainty of ± 300 in the reported values of primary flow Reynolds number in the range $23,000 < \text{Re} < 75,000$.

Values of Mass Flux Ratio

The mass flux ratio was calculated using: $M = \rho_s U_s / \rho_\infty U_\infty$. To obtain values of this parameter, therefore, values of density and velocity for the primary and secondary air flow are required. Uncertainties for the primary air flow velocity have already been discussed. The values of the densities were calculated from measurements of the

corresponding static pressures and temperatures. The error in the results for the densities were estimated to be less than $\pm 0.1\%$ in all cases. The values for the mean velocity of the secondary flow, U_s , were obtained by assuming that the secondary air flow rate, measured by using the 10-point log-linear method in the flow measuring section of the secondary flow circuit (Fig. 11, and Chapter 3), is uniformly distributed over all the injection holes. The geometry of the model blade and the secondary flow measurement set-up used in this work were essentially similar to those used by Saabas (1991). He had determined that the assumption of uniform secondary flow distribution through the injection holes, without the primary cross flow, was accurate to within $\pm 2\%$. Saabas (1991) had also estimated the uncertainty in the secondary mass flow rate measurements to be $\pm 1.5\%$. It should also be noted that the secondary mass flow rate did not change by more than $\pm 1\%$ over the course of an entire run (typically 4-6 hours), and over the course of the measurements for any particular data point (typically, 15 seconds or less) the secondary mass flow rate stayed essentially constant. Factoring in these various uncertainties, it is estimated that the reported values of the mass flux ratio, M , are accurate to within $\pm 6\%$.

Turbulence Intensity Measurements

With the DAS-20 data acquisition card, and the procedure that was used to calibrate the X-wire probe, it is estimated that the mean velocity measurements with the CTA are accurate to within ± 0.1 m/s. With regard to the fluctuating velocity components and the turbulence intensity, after numerous repeatability checks and calibration experiments, it was determined that the uncertainties are within $\pm 1.0\%$: thus $TI = TI_{reported} \pm 1.0\%$.

Calculated Values of Nusselt Number and Film Cooling Effectiveness

As was mentioned earlier in the thesis, excellent repeatability ($<1\%$ differences between values for corresponding runs) was obtained in the calculated values of Nusselt number,

Nu, in the heat transfer studies, and the effectiveness, η , in the film cooling investigation. Thus the major part of the uncertainties in these values is due to errors in the estimation of the corrections to account for conduction within the wall of the model blade, and radiation from the outer surface of the blade to the walls of the test section.

In all cases, the corrections to account for the radiation losses amounted to less than 10% of the report values of Nu or η . Thus uncertainties in the estimates of the radiation corrections have only a negligible effect on the values of Nu and η .

The conduction corrections, however, could be as high as $\pm 40\%$ of the reported values, in the vicinity of $x/D=\pi/4$, where the semicircular leading edge meets the flat after body, and $x/D=\pi/6$, where the centerline of the injection tube intersects the surface of the model blade. It was not possible to come up with an accurate estimate of the uncertainties in the conduction correction - that would require at least two additional sets of runs, each with more T_w measurements than those obtained in this study. A rather crude analysis, based on expected T_w variations indicated that the conduction correction could introduce uncertainties of the order of $\pm 6\%$ in the values of the Nusselt number, and up to $\pm 10\%$ error in the values of the film cooling effectiveness.

Another source of errors in the values of η is the assumption that the values of convective heat transfer coefficient obtained without secondary air injection are also applicable to corresponding cases with air injection. This assumption has been shown to be valid away from the injection sites [Goldstein, 1971], but it could introduce significant error in the immediate vicinity of the injection holes. Again, it is not possible to accurately estimate this error within the scope of this experimental investigation. A rudimentary analysis, based on available data for jets in cross flow, indicated that this assumption could introduce errors up to $\pm 10\%$ in the reported values of η .

Based on all the aforementioned uncertainties, it is estimated that the reported values of Nu could be in error by up to $\pm 10\%$, and the reported values of η could be off by up to $\pm 20\%$.

Figures

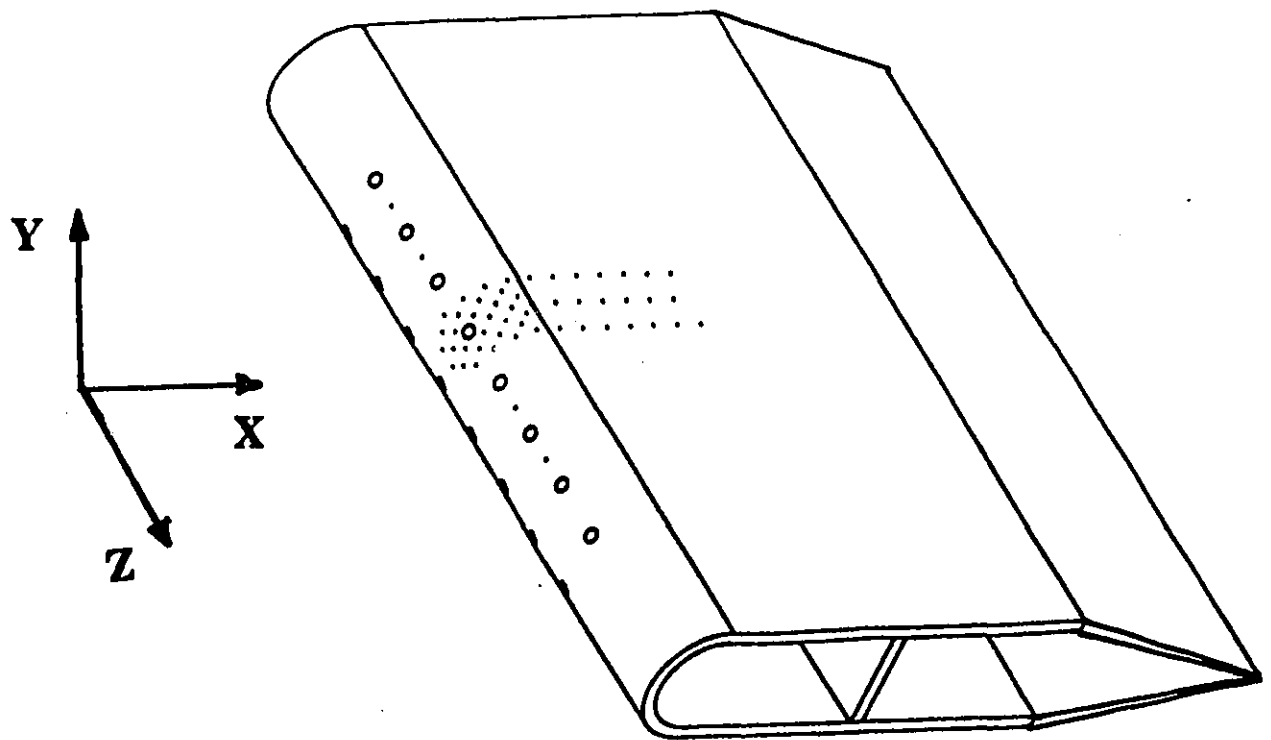
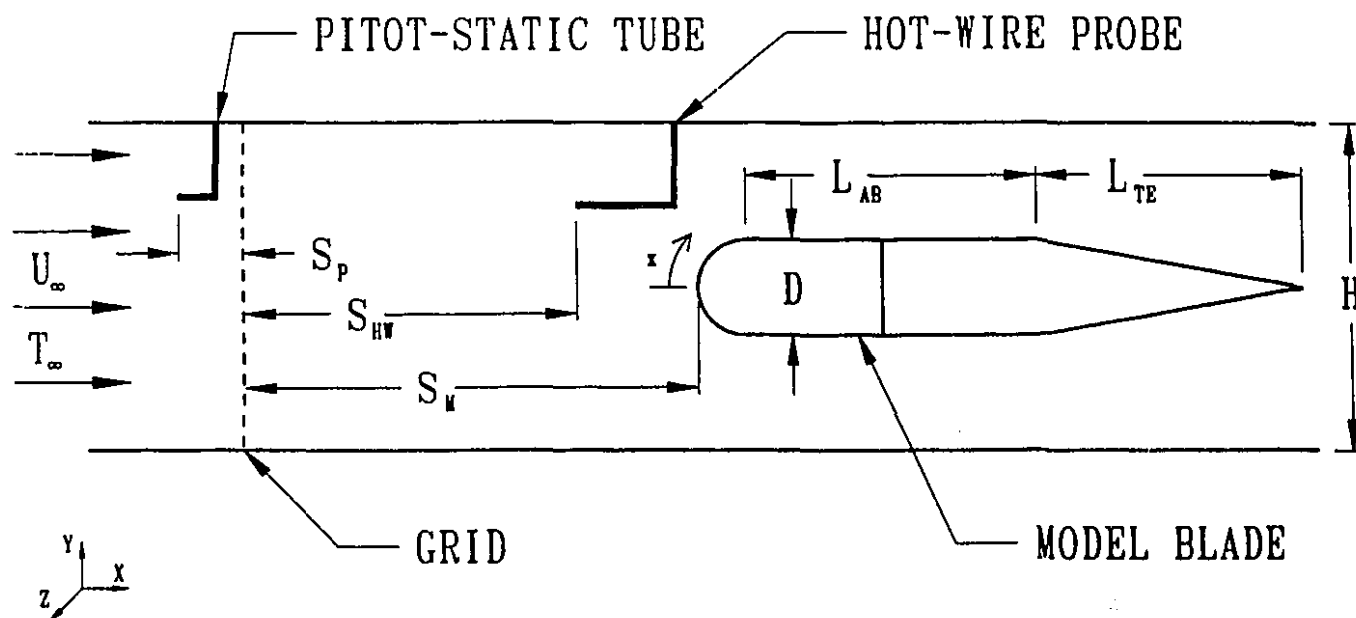


Fig. 1: Schematic illustration of the model blade: leading edge diameter is $D = 126.0$ mm; after body length is 381 mm; trailing edge length is 355 mm; and the width is 762 mm



$$D = 127.0 \text{ mm} ; L_{AB} = 381.0 \text{ mm} ; L_{TE} = 355.6 \text{ mm}$$

$$S_P = 82.6 \text{ mm} ; S_{HW} = 431.8 \text{ mm}$$

$$S_M = 596.9 \text{ mm} ; H = 431.8 \text{ mm}$$

Fig. 2: Cross-sectional view of the test section with the model blade mounted inside:
width of model and test section is 762 mm

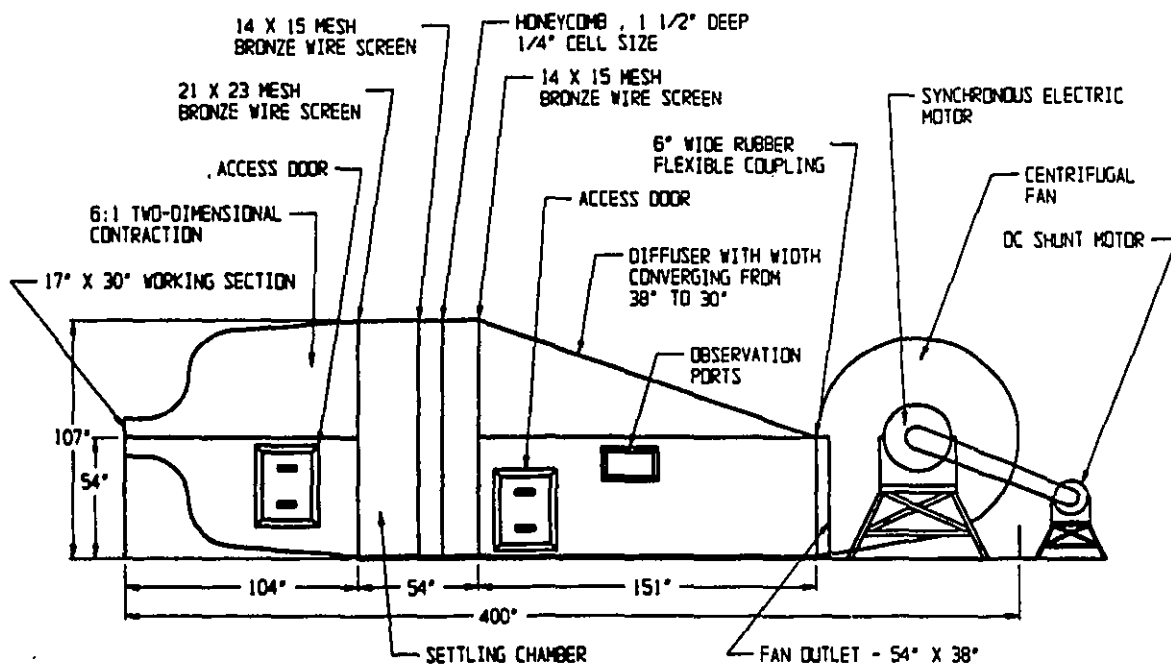


Fig. 3: Schematic illustration of the blower cascade wind tunnel

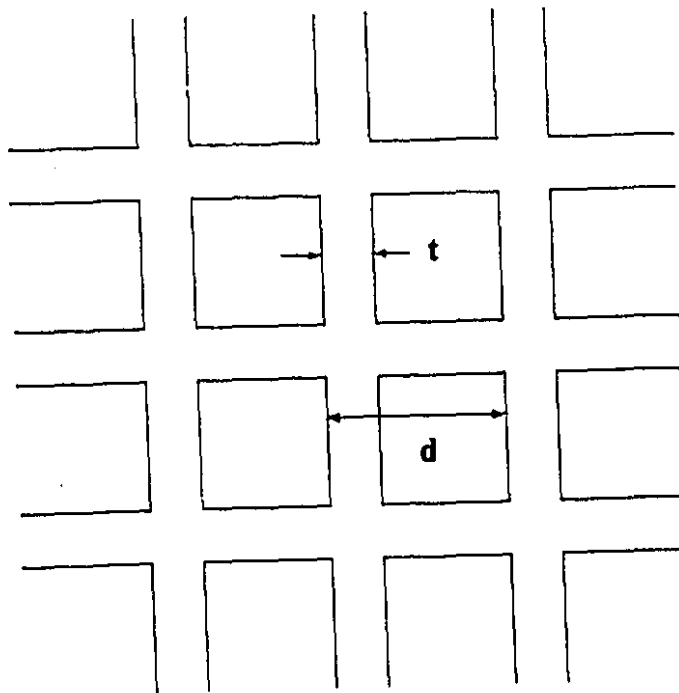


Fig. 4: Square-bar pattern for turbulence generating grid

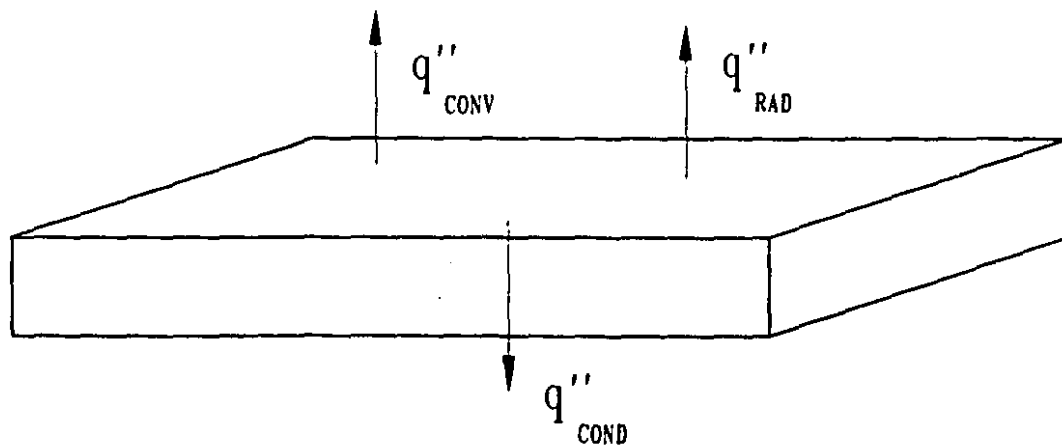


Fig. 5: Local energy balance on the surface of the model blade in film cooling studies

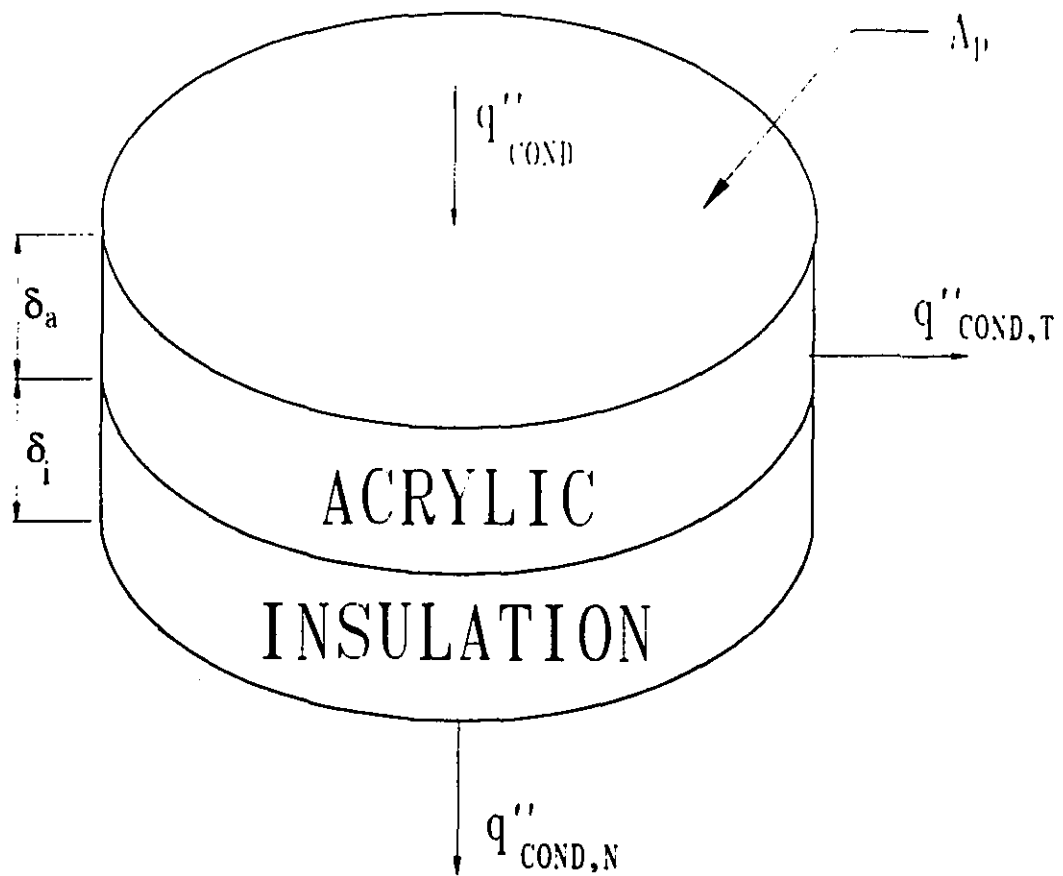


Fig. 6: Local conduction balance for the film cooling experiment

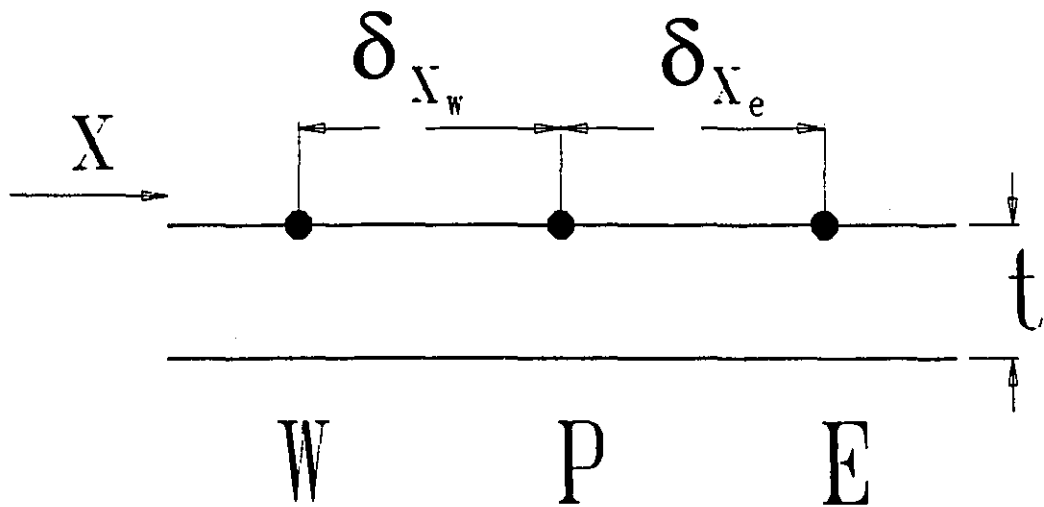


Fig. 7: Quasi one-dimensional control volume for the heat transfer data processing

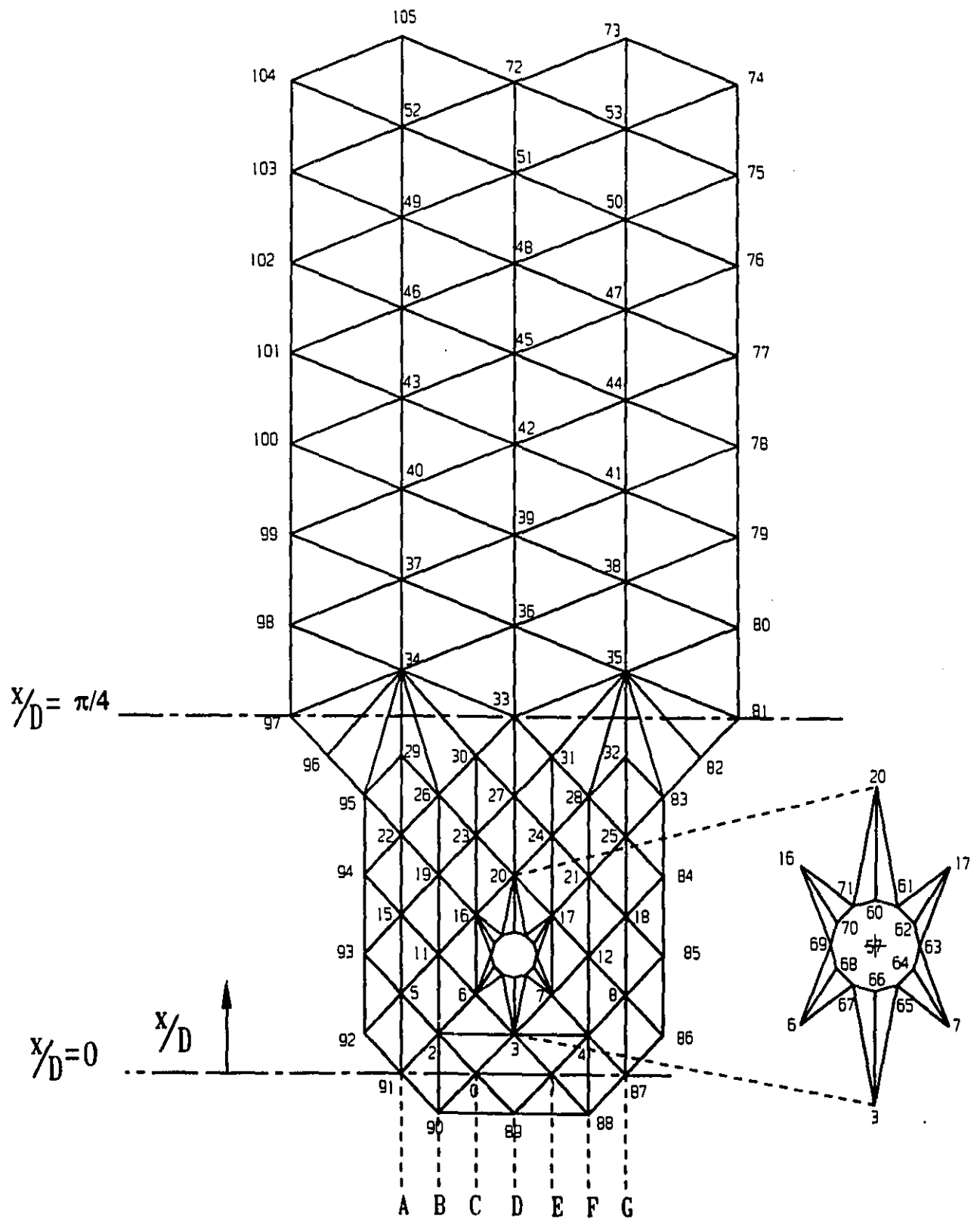


Fig. 8: Thermocouple layout on the surface of the model and the triangular element configuration for the film cooling data processing

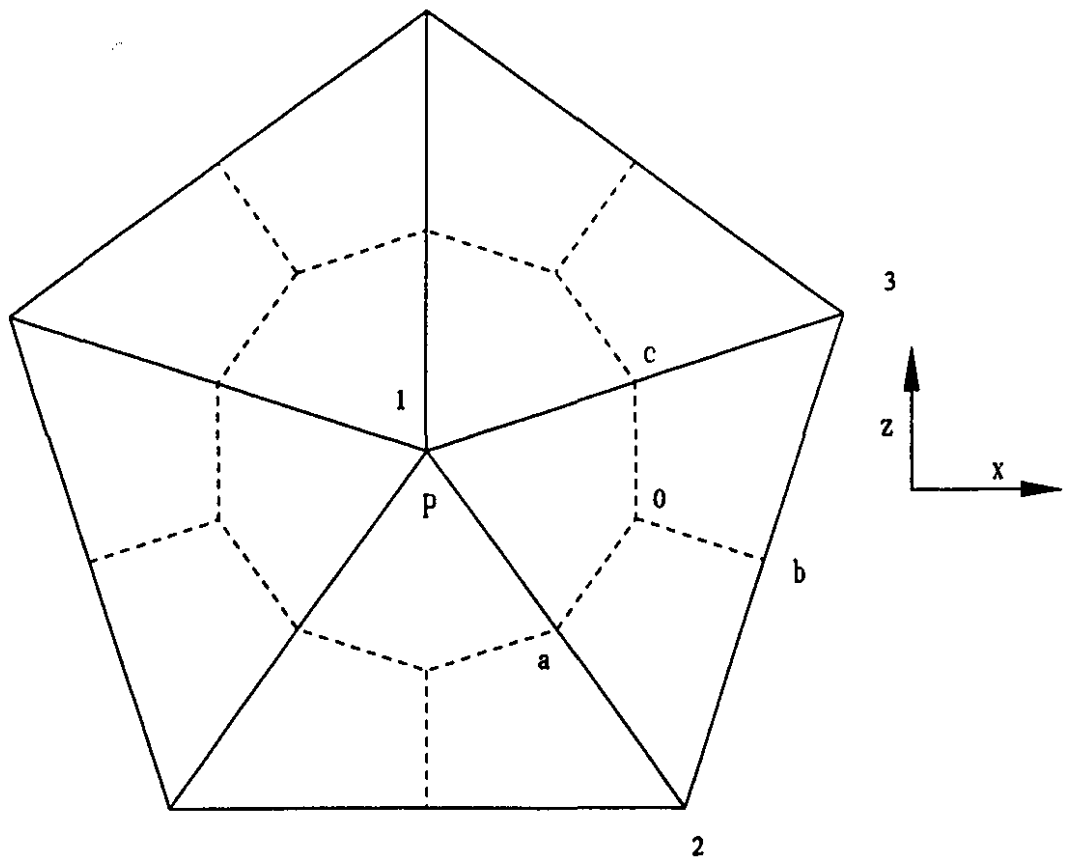


Fig. 9: Details of triangular elements and a control volume surrounding a typical node

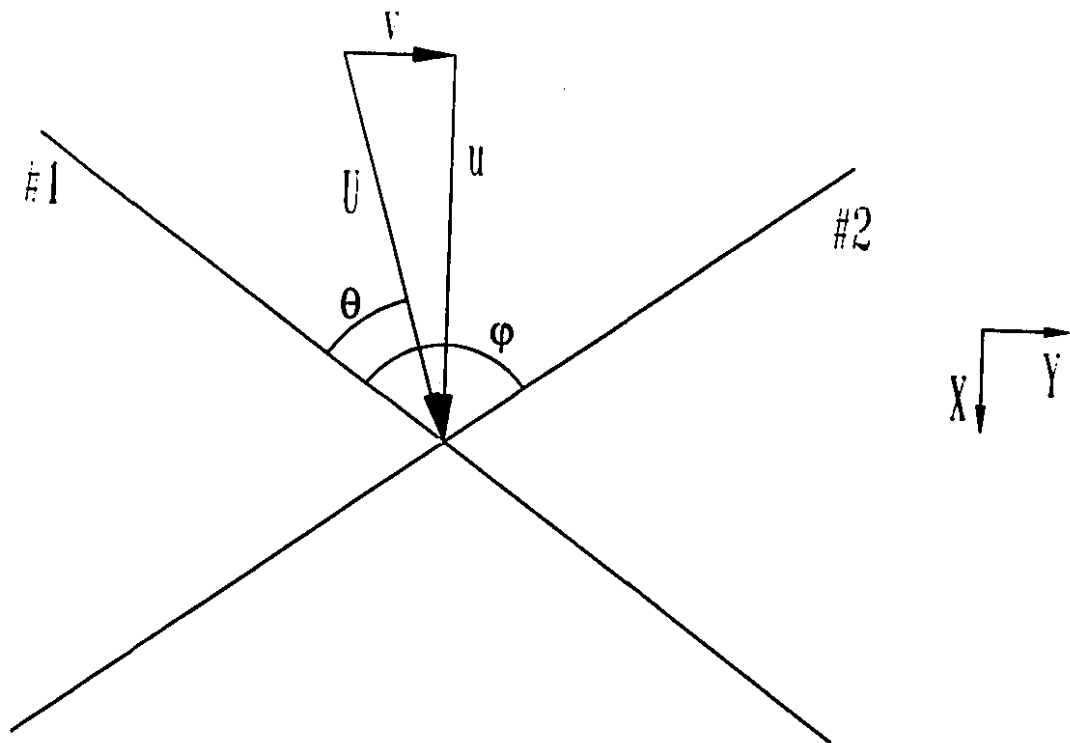


Fig. 10: Details of X-wire probe and notation for the turbulence intensity data processing

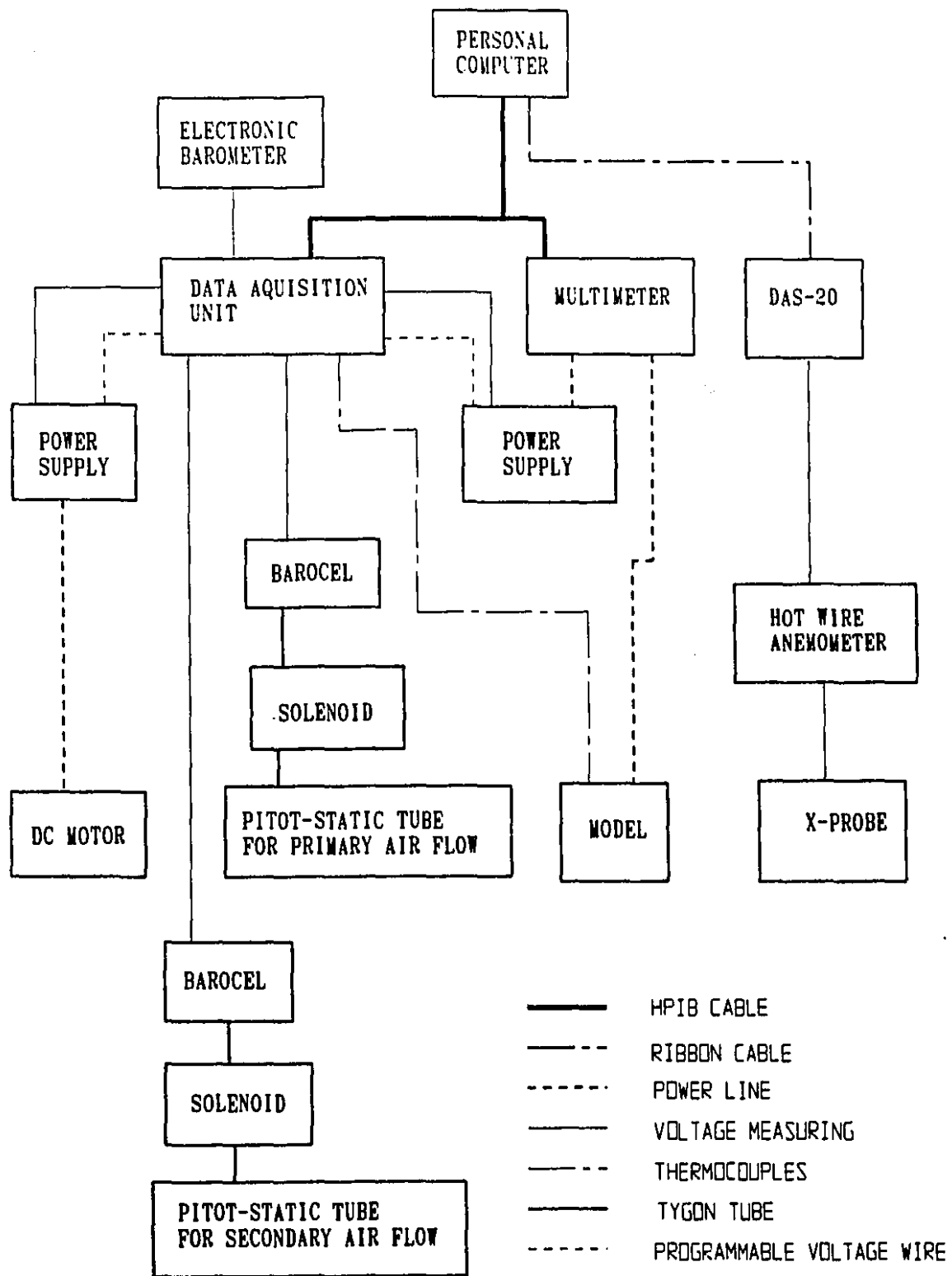


Fig. 11: Experimental apparatus block diagram

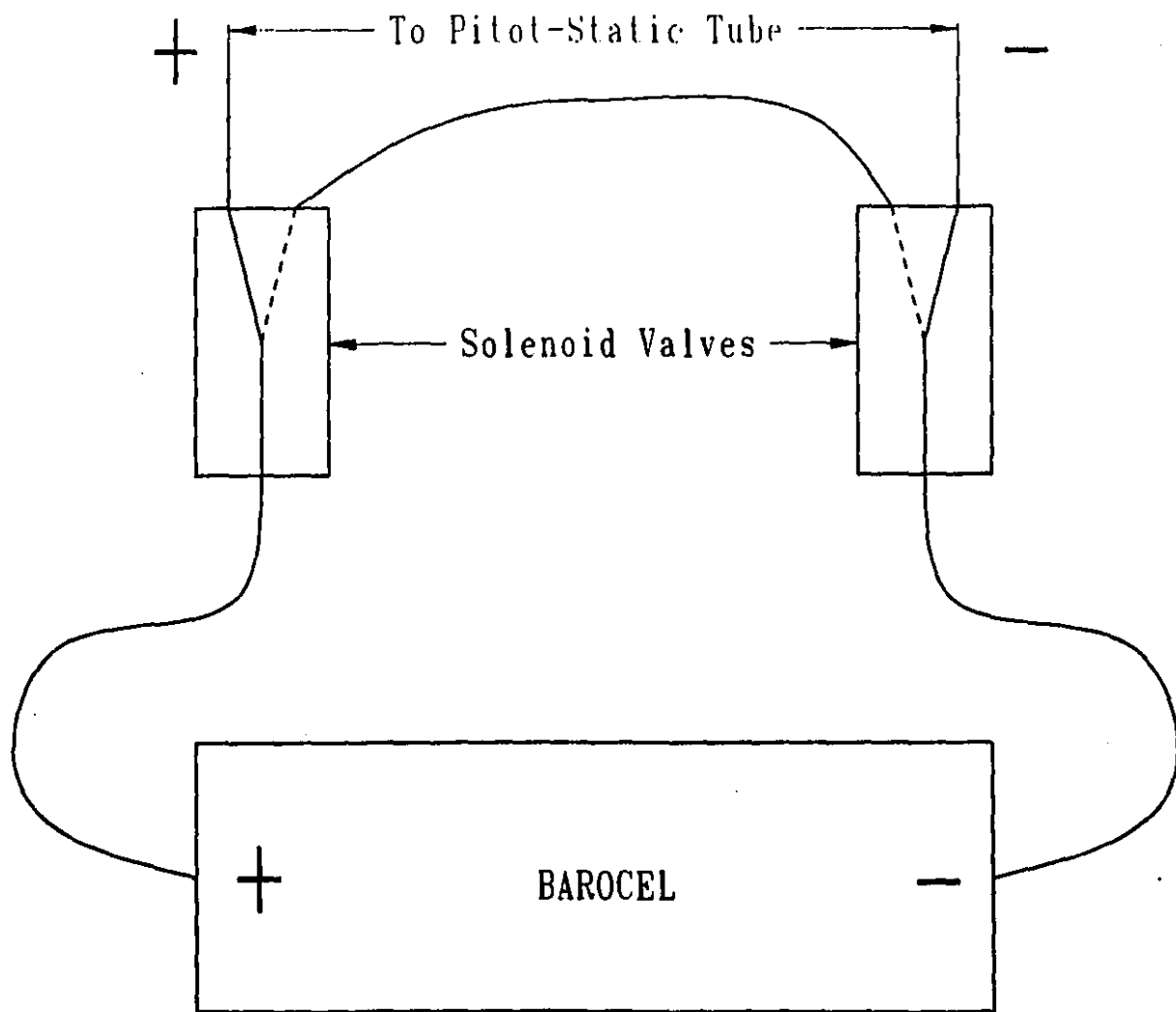


Fig. 12: Details of the differential pressure measuring apparatus

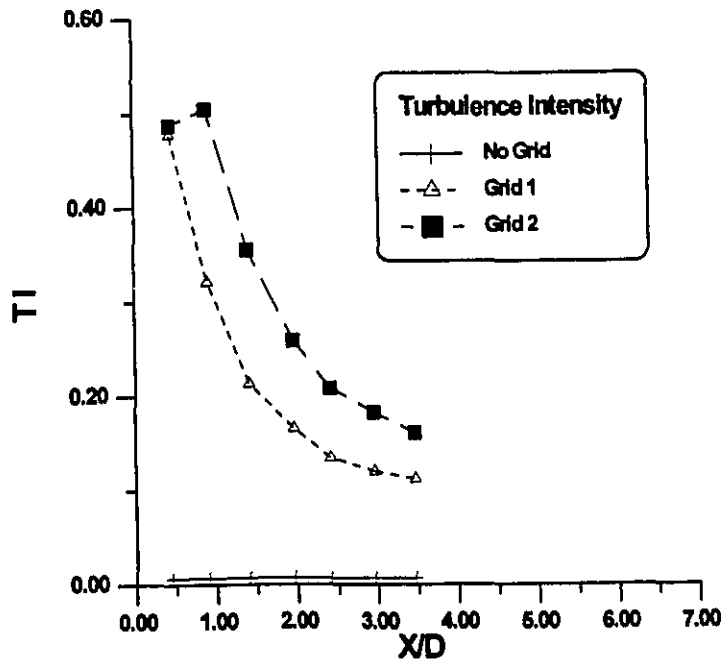


Fig. 13: Variation of turbulence intensity $\left(= \left\{ (u'^2 + v'^2 + w'^2) / U^2 \right\}^{1/2} \right)$ with nondimensional distance (X/D) from the location of the turbulence generating grid, along a line given by Z/D=0 and Y/D=0

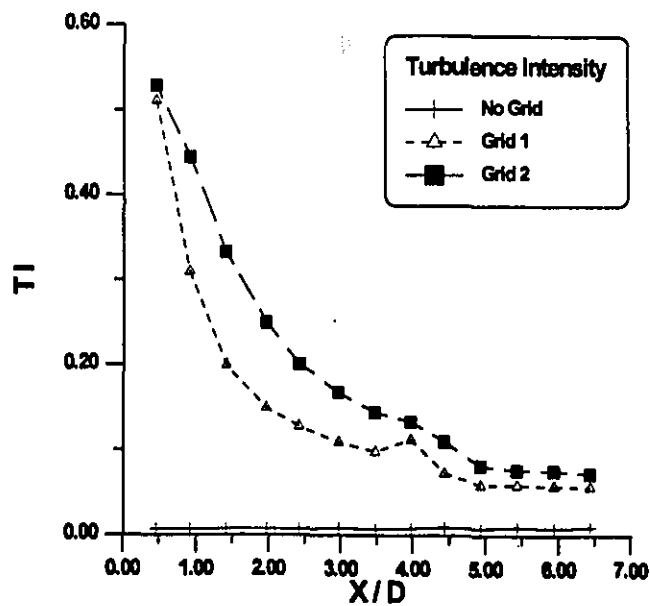


Fig. 14: Variation of turbulence intensity $\left(= \left\{ (u'^2 + v'^2 + w'^2) / U^2 \right\}^{1/2} \right)$ with nondimensional distance (X/D) from the location of the turbulence generating grid, along a line given by Z/D=0 and Y/D=1.7

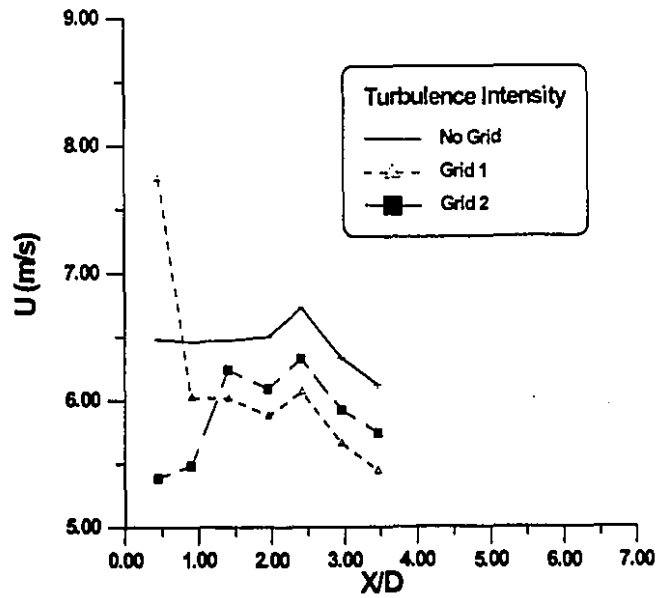


Fig. 15: Variation of mean velocity with nondimensional distance (X/D) from the location of the turbulence generating grid, along a line given by $Z/D=0$ and $Y/D=0$

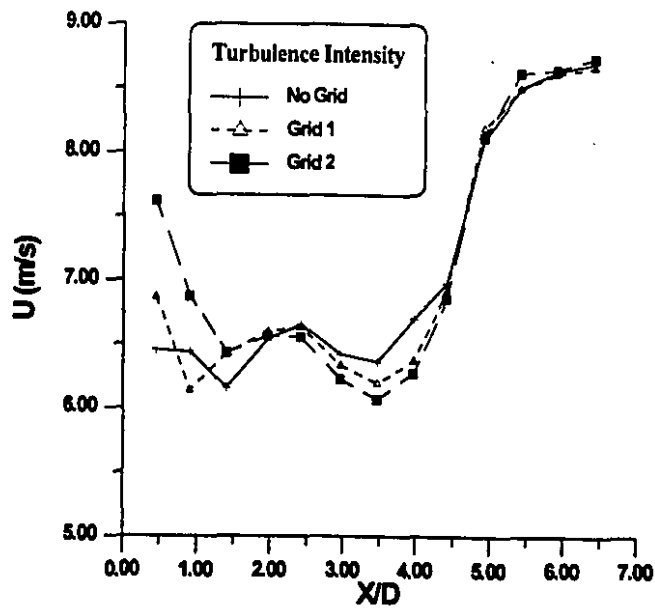


Fig. 16: Variation of mean velocity with nondimensional distance (X/D) from the location of the turbulence generating grid, along a line given by $Z/D=0$ and $Y/D=1.7$

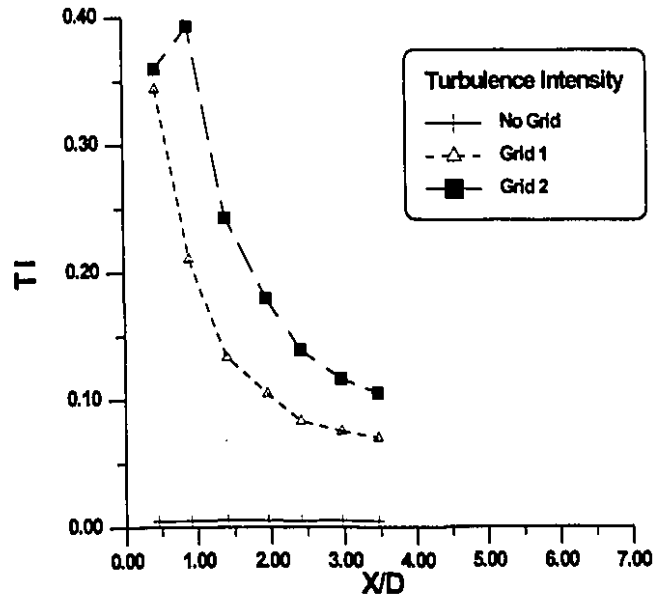


Fig. 17: Variation of turbulence intensity in the free stream direction only $\left(= \{u'^2/U^2\}^{1/2} \right)$ with nondimensional distance (X/D) from the location of the turbulence generating grid, along a line given by Z/D=0 and Y/D=0

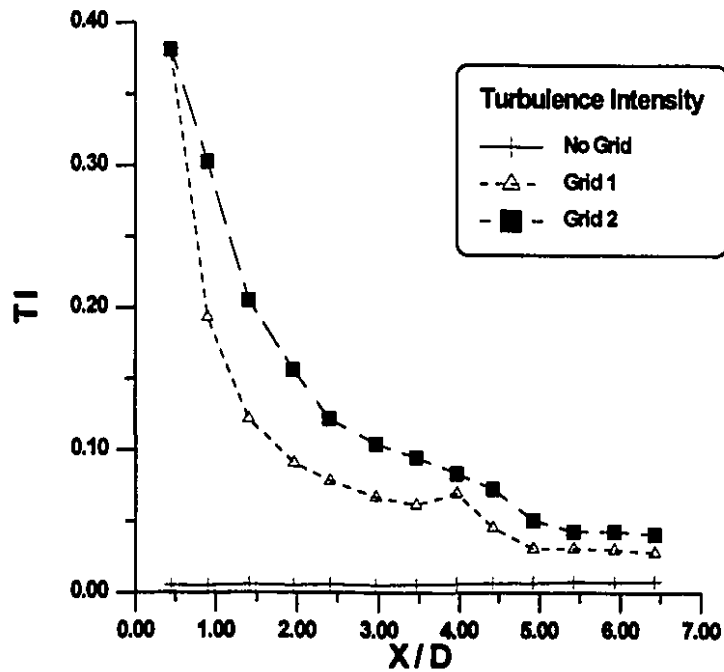


Fig. 18: Variation of turbulence intensity in the free stream direction only $\left(= \{u'^2/U^2\}^{1/2} \right)$ with nondimensional distance (X/D) from the location of the turbulence generating grid, along a line given by Z/D=0 and Y/D=1.7

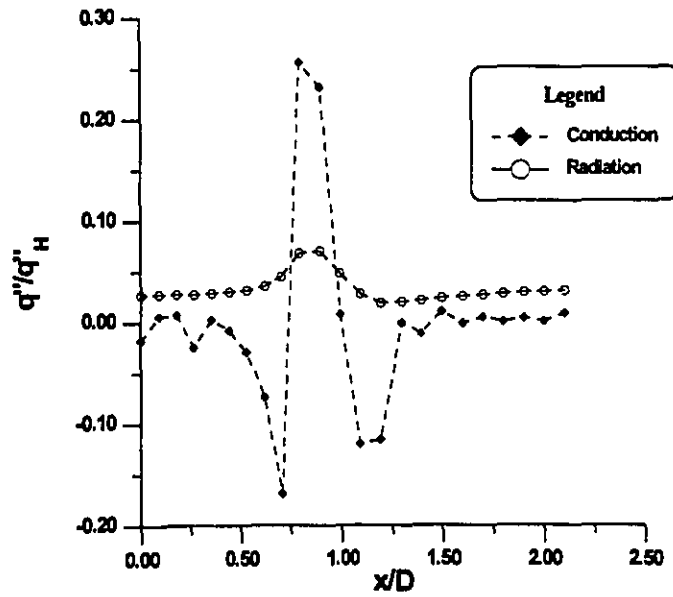


Fig. 19: Normalized local conduction and radiation heat transfer versus nondimensional distance (x/D) from the stagnation line on the model: $Re=51,000$; No Grid

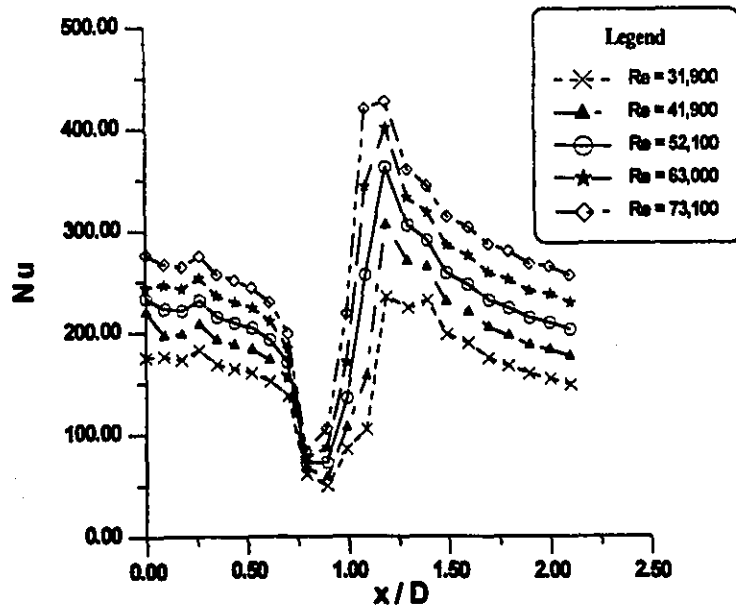


Fig. 20: Local Nusselt number versus nondimensional distance along the model: No grid

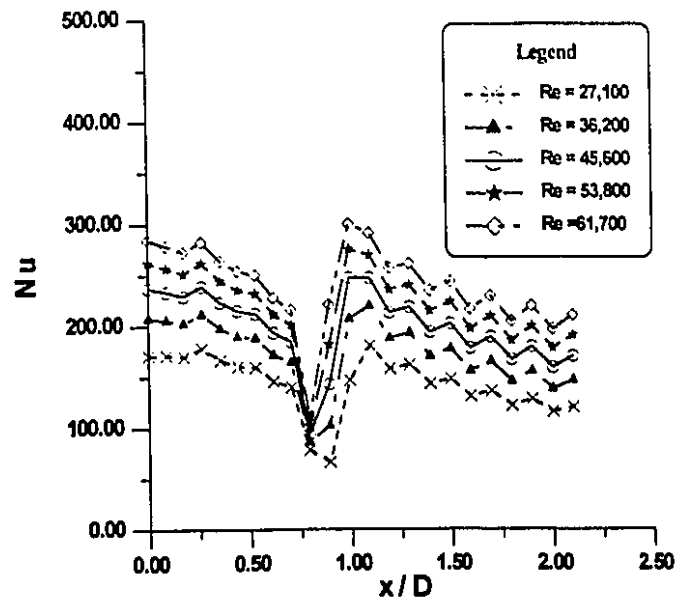


Fig. 21: Local Nusselt number versus nondimensional distance along the model: Grid 1

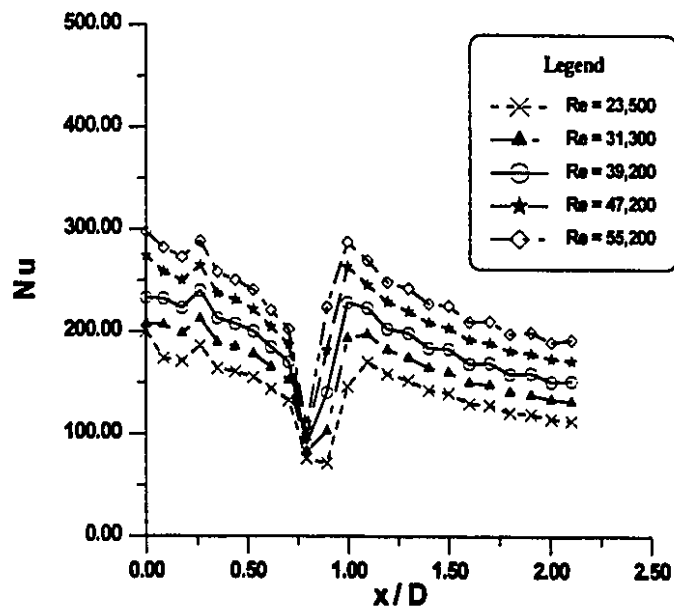


Fig. 22: Local Nusselt number versus nondimensional distance along the model: Grid 2

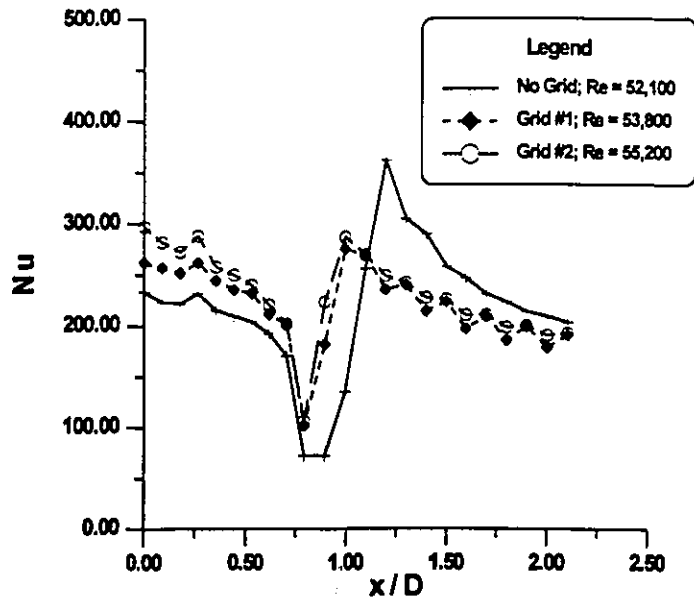


Fig 23: Comparison of local Nusselt numbers for low (No grid), medium (Grid 1), and high turbulence (Grid 2) intensities at a nominal Reynolds number of 54,000

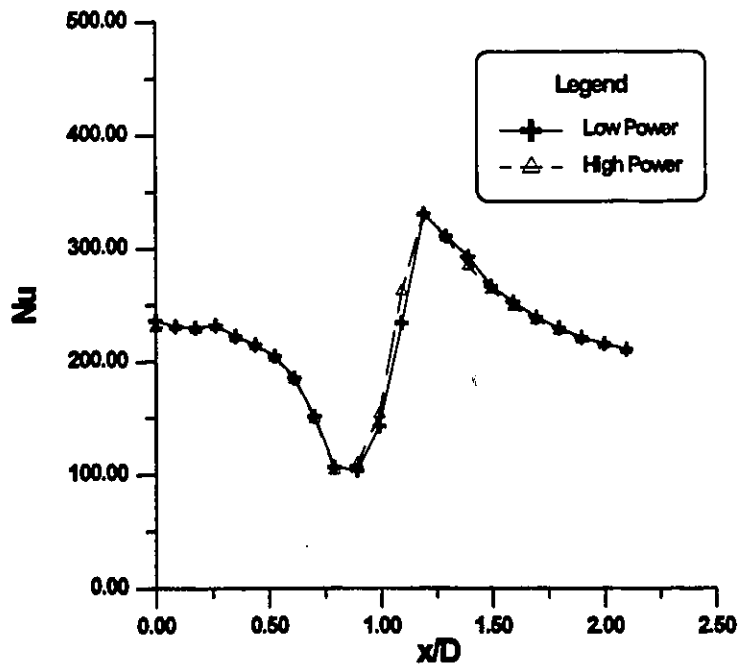


Fig 24: Comparison of local Nusselt numbers at Re=51,000 and at low turbulence (No grid) at two different heater power levels

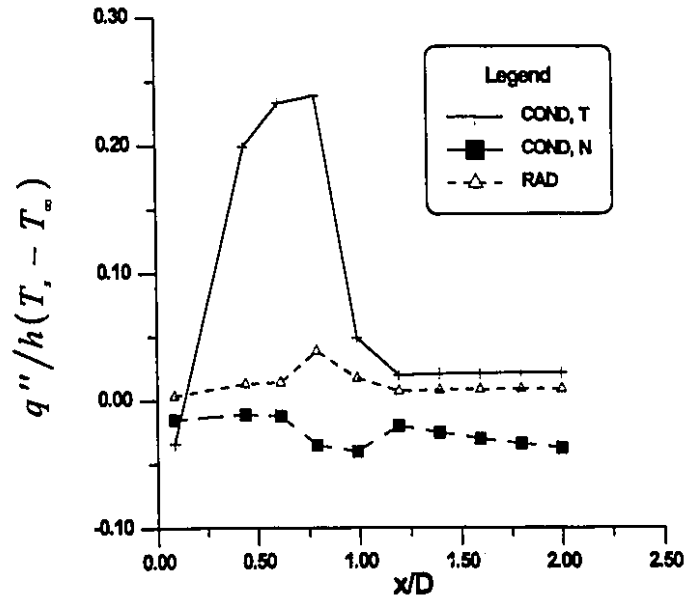


Fig. 25: Film cooling effectiveness correction contributions of conduction and radiation, at nodes along line D: Re=52,100; M=0.96; No Grid

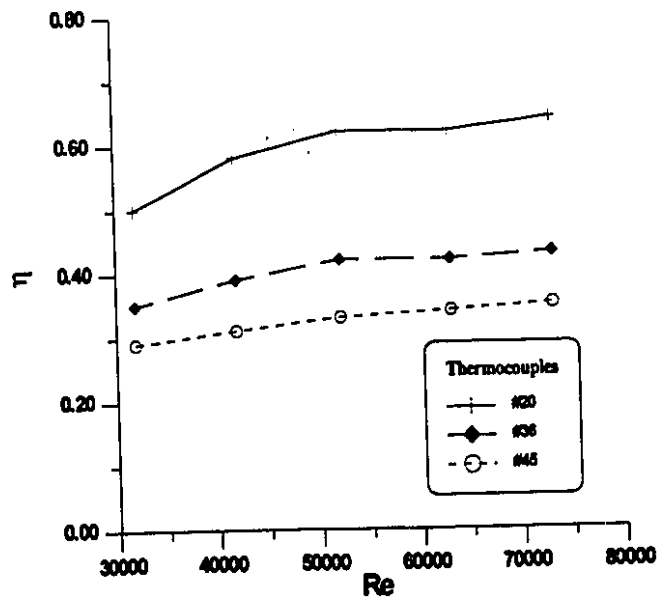


Fig. 26: Local film cooling effectiveness versus nondimensional distance along line D at different Reynolds numbers: No grid

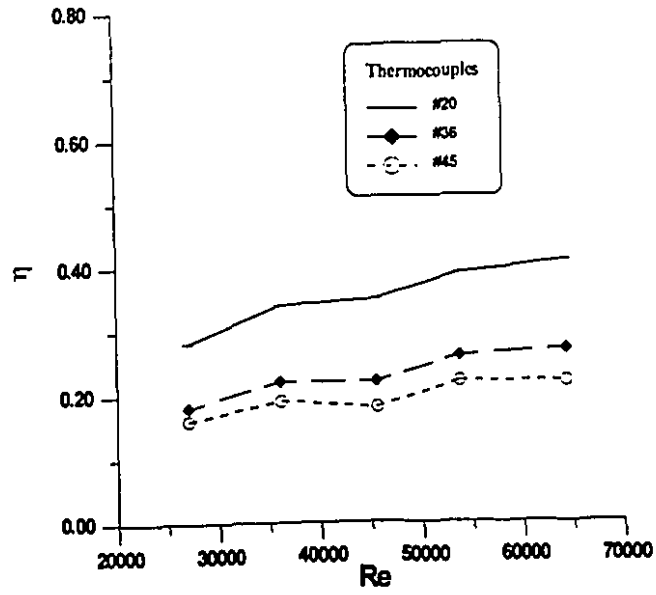


Fig. 27: Local film cooling effectiveness versus nondimensional distance along line D at different Reynolds numbers: Grid 1

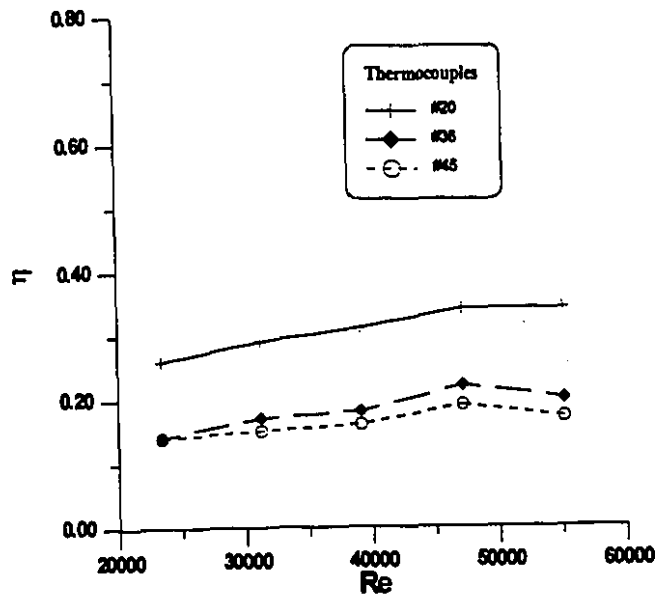


Fig. 28: Local film cooling effectiveness versus nondimensional distance along line D at different Reynolds numbers: Grid 2

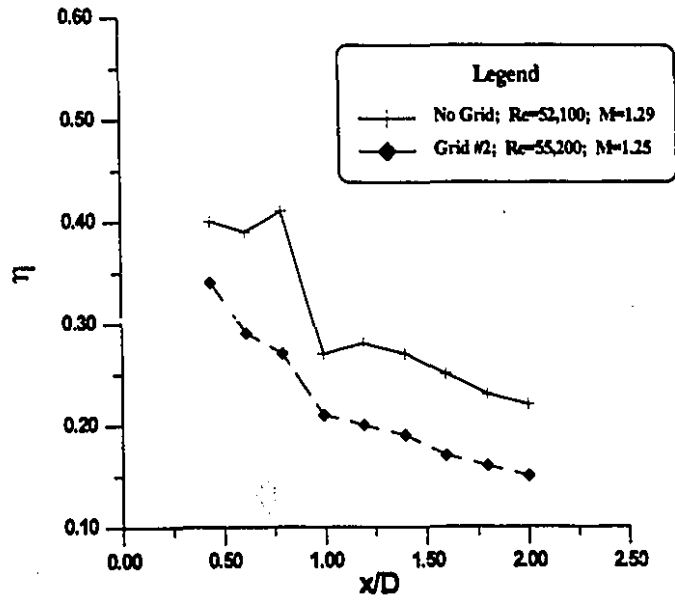


Fig. 29: Comparison of local film cooling effectiveness for the low (No grid) and high (Grid 2) turbulence intensities at a nominal Reynolds number of 53,500 and mass flux ratio of 1.27

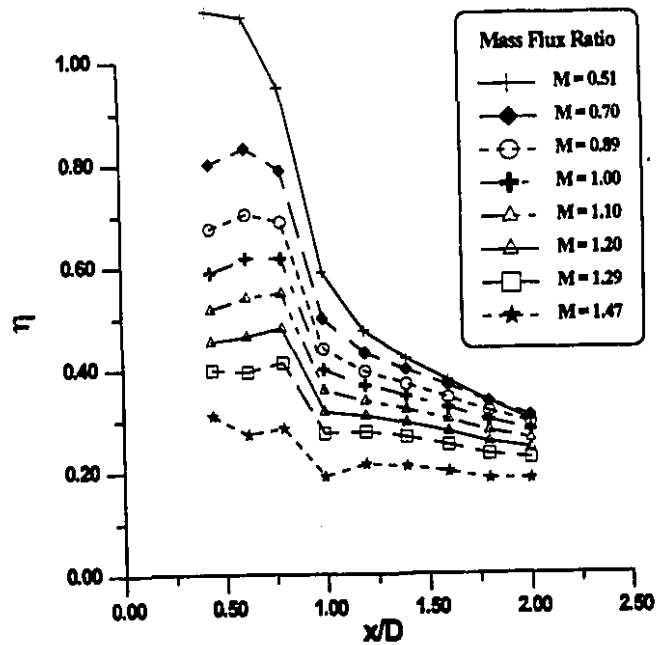


Fig. 30: Local film cooling effectiveness versus nondimensional distance along line D at different mass flux ratios: $Re=52,100$; No grid

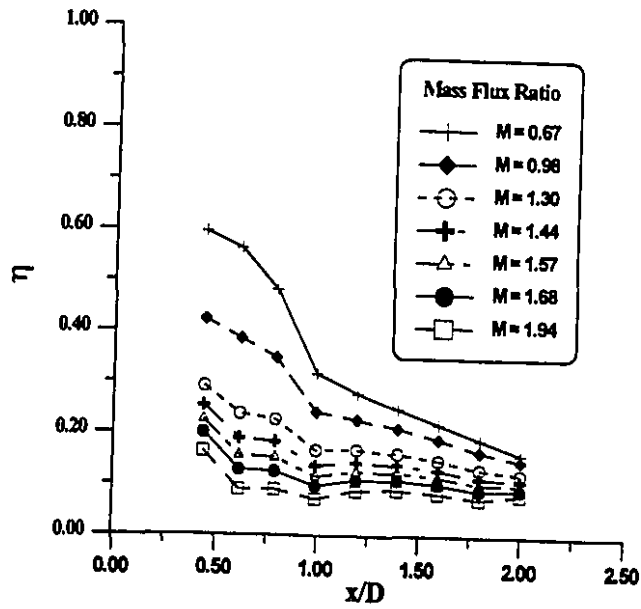


Fig. 31: Local film cooling effectiveness versus nondimensional distance along line D at different mass flux ratios: $Re=39,200$; Grid 2

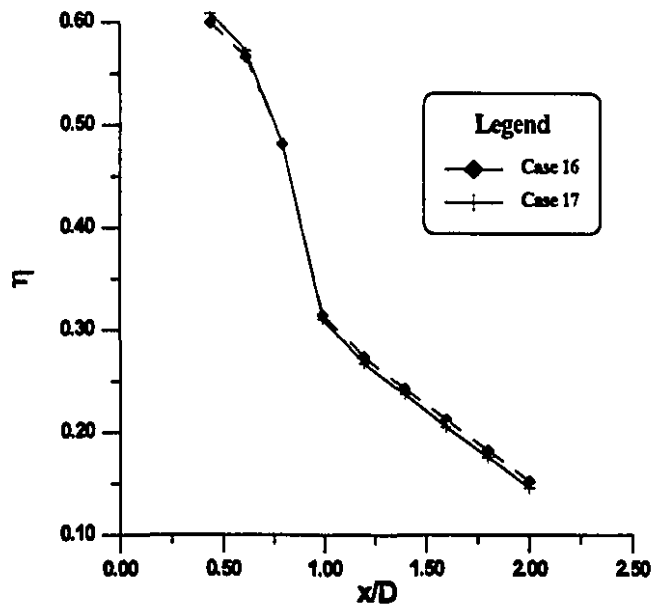


Fig. 32: Comparison of film cooling effectiveness for Cases 16 and 17: $Re=39,200$; $M=0.65$; Grid 2

Tables

Re =	31,900		41,900		52,100		63,000		73,100	
x/D	Φ	Nu								
0.00	1.00	175	1.00	220	1.00	234	1.00	245	1.00	276
0.09	1.00	177	1.05	197	1.02	223	1.00	247	1.02	267
0.18	1.01	173	1.05	198	1.03	222	1.00	243	1.02	264
0.26	0.99	183	1.04	208	1.02	231	0.99	253	1.01	275
0.35	1.04	168	1.09	193	1.06	215	1.04	236	1.06	257
0.44	1.08	164	1.13	188	1.10	210	1.07	230	1.09	250
0.53	1.13	160	1.18	183	1.15	204	1.12	224	1.15	243
0.62	1.25	152	1.31	173	1.27	192	1.24	211	1.26	229
0.70	1.52	137	1.60	154	1.56	170	1.53	184	1.55	198
0.79	2.12	60	2.27	66	2.22	72	2.18	76	2.21	83
0.89	2.34	50	2.44	58	2.27	72	2.13	87	2.06	105
0.99	1.95	85	1.90	106	1.65	135	1.45	170	1.31	218
1.09	1.52	104	1.35	156	1.01	256	0.83	343	0.75	419
1.19	0.92	234	0.83	305	0.71	362	0.67	400	0.68	426
1.30	0.82	224	0.80	270	0.76	305	0.74	332	0.76	360
1.40	0.80	231	0.82	264	0.81	290	0.79	317	0.80	343
1.50	0.88	198	0.91	229	0.88	257	0.86	285	0.87	313
1.60	0.94	189	0.96	219	0.93	246	0.90	275	0.91	303
1.70	1.00	174	1.03	204	0.99	231	0.95	258	0.95	286
1.80	1.05	167	1.07	196	1.03	223	0.98	251	0.98	279
1.90	1.10	159	1.12	187	1.07	214	1.02	240	1.02	267
2.00	1.13	154	1.15	182	1.09	209	1.04	237	1.03	264
2.10	1.16	148	1.18	176	1.12	202	1.06	229	1.06	255

Table 1: Local nondimensional temperatures and Nusselt numbers on the external surface of the model blade: No grid

Re =		27,100	36,200	45,600	53,800	61,700				
x/D	Φ	Nu	Φ	Nu	Φ	Nu	Φ	Nu	Φ	Nu
0.00	1.00	171	1.00	207	1.00	237	1.00	262	1.00	285
0.09	1.00	171	1.00	206	1.01	234	1.01	257	1.01	279
0.18	1.00	170	1.01	202	1.02	229	1.02	252	1.03	273
0.26	0.99	178	1.00	211	1.01	239	1.01	262	1.02	283
0.35	1.03	167	1.04	198	1.05	223	1.06	245	1.06	264
0.44	1.07	160	1.08	190	1.09	215	1.10	236	1.11	254
0.53	1.11	160	1.12	189	1.13	212	1.14	232	1.15	250
0.62	1.21	146	1.23	172	1.24	194	1.25	212	1.25	228
0.70	1.36	140	1.38	165	1.39	185	1.40	201	1.41	216
0.79	1.73	78	1.77	86	1.78	94	1.79	102	1.79	110
0.89	1.80	67	1.65	103	1.52	143	1.41	182	1.33	221
0.99	1.30	147	1.14	207	1.07	247	1.04	275	1.02	300
1.09	1.06	181	1.01	219	1.00	247	1.00	269	1.00	290
1.19	1.08	158	1.08	188	1.08	213	1.08	235	1.08	256
1.30	1.09	162	1.09	193	1.10	218	1.10	240	1.10	261
1.40	1.16	143	1.17	170	1.18	194	1.18	214	1.17	234
1.50	1.18	147	1.19	177	1.19	202	1.19	223	1.18	243
1.60	1.26	130	1.27	155	1.28	178	1.27	197	1.26	216
1.70	1.28	136	1.28	164	1.27	188	1.27	209	1.25	229
1.80	1.35	121	1.36	145	1.35	166	1.35	185	1.33	204
1.90	1.36	127	1.35	155	1.34	179	1.33	198	1.31	219
2.00	1.42	115	1.42	138	1.41	159	1.40	178	1.38	196
2.10	1.41	120	1.40	146	1.39	170	1.37	190	1.35	210

Table 2: Local nondimensional temperatures and Nusselt numbers on the external surface of the model blade: Grid 1

Re =		23,500	31,300	39,200	47,200	55,200				
x/D	Φ	Nu	Φ	Nu	Φ	Nu	Φ	Nu	Φ	Nu
0.00	1.00	200	1.00	208	1.00	233	1.00	274	1.00	297
0.09	1.06	174	1.01	206	1.01	232	1.03	258	1.03	282
0.18	1.08	171	1.02	198	1.02	223	1.05	250	1.05	272
0.26	1.06	186	1.01	213	1.00	240	1.04	265	1.04	288
0.35	1.13	164	1.08	190	1.08	213	1.11	237	1.11	258
0.44	1.17	161	1.12	185	1.12	207	1.16	231	1.16	250
0.53	1.24	155	1.18	178	1.18	200	1.23	221	1.23	240
0.62	1.35	144	1.29	165	1.29	184	1.34	204	1.34	220
0.70	1.54	132	1.47	152	1.47	170	1.52	187	1.52	202
0.79	1.92	76	1.84	82	1.83	90	1.90	98	1.90	106
0.89	1.95	71	1.70	102	1.55	140	1.48	182	1.38	224
0.99	1.43	146	1.22	193	1.14	228	1.12	263	1.09	287
1.09	1.20	170	1.10	197	1.08	223	1.11	246	1.10	269
1.19	1.20	159	1.13	182	1.13	203	1.16	229	1.16	249
1.30	1.24	153	1.18	175	1.17	199	1.21	220	1.20	242
1.40	1.30	142	1.24	165	1.24	184	1.27	209	1.26	227
1.50	1.34	140	1.28	161	1.27	183	1.31	204	1.29	225
1.60	1.41	130	1.34	151	1.34	169	1.37	193	1.36	210
1.70	1.45	128	1.38	148	1.37	170	1.40	189	1.38	210
1.80	1.51	121	1.43	141	1.42	159	1.45	181	1.44	198
1.90	1.55	119	1.47	138	1.45	159	1.48	179	1.45	200
2.00	1.59	115	1.50	134	1.49	151	1.51	174	1.50	190
2.10	1.61	113	1.52	132	1.50	152	1.53	172	1.50	192

Table 3: Local nondimensional temperatures and Nusselt numbers on the external surface of the model blade: Grid 2

CASE 1: Re=31,900 M=0.95
 No grid T_∞=23.7°C T_S=77.6°C

x/D	D	C/E	B/F	A/G
0.000		0.09		
0.087	0.11		0.06	
0.175		0.02		0.05
0.264			0.09	
0.352		0.09		0.06
0.440	0.50		0.05	
0.527		0.10		0.04
0.615	0.54		0.06	
0.703		0.14		0.03
0.791	0.52			
0.892				-0.01
0.993	0.35			
1.094				-0.01
1.195	0.33			
1.295				0.07
1.396	0.31			
1.497				0.09
1.598	0.29			
1.699				0.07
1.799	0.26			
1.900				0.05
2.001	0.24			
2.102				0.04

CASE 2: Re=41,900 M=0.95
 No grid T_∞=23.8°C T_S=75.3°C

x/D	D	C/E	B/F	A/G
0.000		0.08		
0.087	0.09		0.05	
0.175		-0.04		0.07
0.264			0.08	
0.352		0.04		0.06
0.440	0.58		0.05	
0.527		0.11		0.04
0.615	0.61		0.05	
0.703		0.17		0.04
0.791	0.60			
0.892				-0.01
0.993	0.39			
1.094				0.02
1.195	0.36			
1.295				0.07
1.396	0.34			
1.497				0.09
1.598	0.31			
1.699				0.07
1.799	0.29			
1.900				0.05
2.001	0.26			
2.102				0.04

CASE 3: Re=52,100 M=0.96
 No grid T_∞=24.0°C T_S=74.1°C

x/D	D	C/E	B/F	A/G
0.000		0.08		
0.087	0.09		0.05	
0.175		-0.06		0.07
0.264			0.07	
0.352		0.03		0.06
0.440	0.62		0.04	
0.527		0.11		0.04
0.615	0.64		0.04	
0.703		0.18		0.05
0.791	0.64			
0.892				-0.02
0.993	0.42			
1.094				0.04
1.195	0.38			
1.295				0.07
1.396	0.36			
1.497				0.09
1.598	0.33			
1.699				0.07
1.799	0.30			
1.900				0.05
2.001	0.28			
2.102				0.05

CASE 4: Re=63,000 M=0.96
 No grid T_∞=24.5°C T_S=82.4°C

x/D	D	C/E	B/F	A/G
0.000		0.08		
0.087	0.08		0.05	
0.175		-0.04		0.06
0.264			0.07	
0.352		0.04		0.06
0.440	0.62		0.04	
0.527		0.12		0.04
0.615	0.64		0.04	
0.703		0.19		0.05
0.791	0.65			
0.892				-0.02
0.993	0.42			
1.094				0.05
1.195	0.38			
1.295				0.07
1.396	0.36			
1.497				0.08
1.598	0.34			
1.699				0.07
1.799	0.31			
1.900				0.06
2.001	0.29			
2.102				0.05

Table 4: Local film cooling effectiveness on the external surface of the model blade:

Cases 1 to 4

CASE 5: Re=73,100 M=0.97
 No grid T_w=24.9°C Ts=82.0°C

x/D	D	C/E	B/F	A/G
0.000		0.08		
0.087	0.08		0.05	
0.175		- .04		0.06
0.264			0.07	
0.352		0.04		0.05
0.440	0.64		0.04	
0.527		0.12		0.04
0.615	0.66		0.03	
0.703		0.20		0.06
0.791	0.67			
0.892			- .02	
0.993	0.43			
1.094			0.06	
1.195	0.39			
1.295			0.07	
1.396	0.37			
1.497			0.08	
1.598	0.35			
1.699			0.07	
1.799	0.32			
1.900			0.06	
2.001	0.30			
2.102			0.05	

CASE 6: Re=27,100 M=1.20
 Grid 1 T_w=23.5°C Ts=76.5°C

x/D	D	C/E	B/F	A/G
0.000		0.09		
0.087	0.12		0.05	
0.175		0.17		0.06
0.264			0.08	
0.352		0.19		0.05
0.440	0.28		0.04	
0.527		0.12		0.03
0.615	0.23		0.06	
0.703		0.13		0.01
0.791	0.23			
0.892				0.05
0.993	0.17			
1.094				0.04
1.195	0.18			
1.295				0.06
1.396	0.17			
1.497				0.08
1.598	0.16			
1.699				0.06
1.799	0.14			
1.900				0.04
2.001	0.12			
2.102				0.02

CASE 7: Re=36,200 M=1.12
 Grid 1 T_w=23.3°C Ts=73.0°C

x/D	D	C/E	B/F	A/G
0.000		0.08		
0.087	0.10		0.05	
0.175		0.10		0.06
0.264			0.08	
0.352		0.14		0.05
0.440	0.34		0.04	
0.527		0.14		0.03
0.615	0.31		0.05	
0.703		0.15		0.02
0.791	0.30			
0.892				0.05
0.993	0.22			
1.094			0.04	
1.195	0.21			
1.295			0.06	
1.396	0.20			
1.497			0.08	
1.598	0.18			
1.699			0.06	
1.799	0.16			
1.900			0.04	
2.001	0.14			
2.102			0.03	

CASE 8: Re=45,600 M=1.12
 Grid 1 T_w=23.8°C Ts=77.9°C

x/D	D	C/E	B/F	A/G
0.000		0.08		
0.087	0.10		0.05	
0.175		0.10		0.06
0.264			0.07	
0.352		0.14		0.05
0.440	0.35		0.04	
0.527		0.15		0.03
0.615	0.31		0.05	
0.703		0.16		0.03
0.791	0.30			
0.892				0.05
0.993	0.22			
1.094				0.05
1.195	0.21			
1.295				0.07
1.396	0.19			
1.497				0.09
1.598	0.17			
1.699				0.07
1.799	0.15			
1.900				0.05
2.001	0.13			
2.102				0.04

Table 5: Local film cooling effectiveness on the external surface of the model blade:

Cases 5 to 8

CASE 9: Re=53,800 M=1.12
 Grid 1 T_∞=24.1°C Ts=81.7°C

x/D	D	C/E	B/F	A/G
0.000		0.08		
0.087	0.09		0.05	
0.175		0.08		0.06
0.264			0.07	
0.352		0.12		0.05
0.440	0.40		0.04	
0.527		0.15		0.03
0.615	0.37		0.05	
0.703		0.18		0.03
0.791	0.36			
0.892				0.05
0.993	0.26			
1.094				0.05
1.195	0.25			
1.295				0.06
1.396	0.23			
1.497				0.08
1.598	0.21			
1.699				0.07
1.799	0.19			
1.900				0.05
2.001	0.17			
2.102				0.04

CASE 10: Re=64,400 M=1.10
 Grid 1 T_∞=24.2°C Ts=81.4°C

x/D	D	C/E	B/F	A/G
0.000		0.08		
0.087	0.09		0.05	
0.175		0.07		0.06
0.264			0.07	
0.352		0.12		0.05
0.440	0.41		0.04	
0.527		0.15		0.03
0.615	0.39		0.05	
0.703		0.19		0.03
0.791	0.37			
0.892				0.05
0.993	0.27			
1.094				0.05
1.195	0.26			
1.295				0.06
1.396	0.24			
1.497				0.09
1.598	0.22			
1.699				0.07
1.799	0.20			
1.900				0.06
2.001	0.19			
2.102				0.05

CASE 11: Re=23,500 M=1.32
 Grid 2 T_∞=23.1°C Ts=75.3°C

x/D	D	C/E	B/F	A/G
0.000		0.09		
0.087	0.12		0.05	
0.175		0.19		0.07
0.264			0.08	
0.352		0.20		0.06
0.440	0.26		0.04	
0.527		0.11		0.04
0.615	0.20		0.06	
0.703		0.11		0.02
0.791	0.20			
0.892				0.05
0.993	0.14			
1.094				0.05
1.195	0.15			
1.295				0.07
1.396	0.15			
1.497				0.10
1.598	0.14			
1.699				0.08
1.799	0.12			
1.900				0.06
2.001	0.10			
2.102				0.04

CASE 12: Re=31,300 M=1.30
 Grid 2 T_∞=23.2°C Ts=74.7°C

x/D	D	C/E	B/F	A/G
0.000		0.08		
0.087	0.11		0.05	
0.175		0.14		0.06
0.264			0.08	
0.352		0.16		0.06
0.440	0.29		0.04	
0.527		0.11		0.04
0.615	0.24		0.05	
0.703		0.12		0.03
0.791	0.23			
0.892				0.05
0.993	0.17			
1.094				0.05
1.195	0.17			
1.295				0.08
1.396	0.16			
1.497				0.10
1.598	0.15			
1.699				0.08
1.799	0.13			
1.900				0.06
2.001	0.12			
2.102				0.05

Table 6: Local film cooling effectiveness on the external surface of the model blade:

Cases 9 to 12

CASE 13: Re=39,200 M=1.25
 Grid 2 T_∞=23.9°C Ts=80.0°C

x/D	D	C/E	B/F	A/G
0.000		0.08		
0.087	0.10		0.05	
0.175		0.13		0.06
0.264			0.08	
0.352		0.15		0.06
0.440	0.31		0.04	
0.527		0.12		0.04
0.615	0.26		0.05	
0.703		0.14		0.04
0.791	0.25			0.06
0.892				0.06
0.993	0.18			
1.094				0.06
1.195	0.18			
1.295			0.08	
1.396	0.17			
1.497			0.11	
1.598	0.16			
1.699			0.09	
1.799	0.14			
1.900			0.07	
2.001	0.13			
2.102			0.06	

CASE 14: Re=47,200 M=1.26
 Grid 2 T_∞=23.2°C Ts=81.6°C

x/D	D	C/E	B/F	A/G
0.000		0.08		
0.087	0.10		0.05	
0.175		0.11		0.07
0.264			0.08	
0.352		0.14		0.06
0.440	0.34		0.05	
0.527		0.14		0.04
0.615	0.30		0.05	
0.703		0.16		0.05
0.791	0.29			
0.892				0.07
0.993	0.22			
1.094				0.07
1.195	0.22			
1.295				0.09
1.396	0.21			
1.497				0.11
1.598	0.19			
1.699				0.10
1.799	0.17			
1.900				0.08
2.001	0.16			
2.102				0.08

CASE 15: Re=55,200 M=1.25
 Grid 2 T_∞=24.8°C Ts=81.1°C

x/D	D	C/E	B/F	A/G
0.000		0.07		
0.087	0.09		0.05	
0.175		0.10		0.06
0.264			0.07	
0.352		0.13		0.06
0.440	0.34		0.04	
0.527		0.13		0.04
0.615	0.29		0.05	
0.703		0.15		0.05
0.791	0.27			
0.892				0.06
0.993	0.21			
1.094				0.07
1.195	0.20			
1.295				0.09
1.396	0.19			
1.497				0.12
1.598	0.17			
1.699				0.11
1.799	0.16			
1.900				0.09
2.001	0.15			
2.102				0.09

Table 7: Local film cooling effectiveness on the external surface of the model blade:

Cases 13 to 15

CASE 16: Re=39,200 M=0.65
Grid 2 T_w=21.8°C Ts=73.3°C;

x/D	D	C/E	B/F	A/G
0.000		0.07		
0.087	0.07		0.04	
0.175		-0.07		0.06
0.264			0.06	
0.352		0.06		0.05
0.440	0.59		0.03	
0.527		0.16		0.03
0.615	0.56		0.03	
0.703		0.21		0.03
0.791	0.48			
0.892			0.07	
0.993	0.31			
1.094			0.06	
1.195	0.27			
1.295			0.09	
1.396	0.24			
1.497			0.12	
1.598	0.21			
1.699			0.11	
1.799	0.18			
1.900			0.09	
2.001	0.15			
2.102			0.08	

CASE 17: Re=39,200 M=0.65
Grid 2 T_w=21.8°C Ts=67.8°C;

x/D	D	C/E	B/F	A/G
0.000		0.06		
0.087	0.07		0.03	
0.175		-0.09		0.05
0.264			0.05	
0.352		0.05		0.04
0.440	0.60		0.02	
0.527		0.16		0.03
0.615	0.57		0.02	
0.703		0.20		0.03
0.791	0.48			
0.892				0.06
0.993	0.31			
1.094				0.05
1.195	0.27			
1.295				0.08
1.396	0.24			
1.497				0.11
1.598	0.21			
1.699				0.10
1.799	0.18			
1.900				0.08
2.001	0.15			
2.102				0.07

CASE 18: Re=39,200 M=1.94
Grid 2 T_w=21.9°C Ts=81.0°C;

x/D	D	C/E	B/F	A/G
0.000		0.07		
0.087	0.11		0.04	
0.175		0.22		0.06
0.264			0.06	
0.352		0.20		0.05
0.440	0.16		0.03	
0.527		0.07		0.03
0.615	0.09		0.04	
0.703		0.06		0.03
0.791	0.09			
0.892			0.04	
0.993	0.07			
1.094			0.04	
1.195	0.09			
1.295			0.06	
1.396	0.09			
1.497			0.08	
1.598	0.08			
1.699			0.06	
1.799	0.07			
1.900			0.04	
2.001	0.08			
2.102			0.04	

CASE 19: Re=39,200 M=1.94
Grid 2 T_w=22.2°C Ts=76.6°C;

x/D	D	C/E	B/F	A/G
0.000		0.07		
0.087	0.10		0.04	
0.175		0.21		0.06
0.264			0.06	
0.352		0.19		0.04
0.440	0.16		0.03	
0.527		0.07		0.03
0.615	0.09		0.04	
0.703		0.06		0.03
0.791	0.09			
0.892				0.04
0.993	0.07			
1.094				0.04
1.195	0.09			
1.295				0.06
1.396	0.09			
1.497				0.08
1.598	0.08			
1.699				0.06
1.799	0.07			
1.900				0.04
2.001	0.08			
2.102				0.04

Table 8: Local film cooling effectiveness on the external surface of the model blade:

Cases 16 to 19

CASE 20: Re=52,100 M=0.51
no grid $T_{\infty}=22.3^{\circ}\text{C}$ $T_s=74.4^{\circ}\text{C}$;

x/D	D	C/E	B/F	A/G
0.000		0.07		
0.087	0.05		0.04	
0.175		-.33		0.06
0.264			0.05	
0.352		-.05		0.05
0.440	1.10		0.02	
0.527		0.17		0.03
0.615	1.09		0.02	
0.703		0.25		0.03
0.791	0.95			
0.892			-.02	
0.993	0.59			
1.094			0.02	
1.195	0.47			
1.295			0.06	
1.396	0.42			
1.497			0.07	
1.598	0.38			
1.699			0.06	
1.799	0.34			
1.900			0.04	
2.001	0.30			
2.102			0.03	

CASE 21: Re=52,100 M=0.70
no grid $T_{\infty}=22.5^{\circ}\text{C}$ $T_s=76.8^{\circ}\text{C}$;

x/D	D	C/E	B/F	A/G
0.000		0.07		
0.087	0.07		0.04	
0.175		-.17		0.06
0.264			0.06	
0.352		-.01		0.05
0.440	0.80		0.03	
0.527		0.12		0.03
0.615	0.83		0.03	
0.703		0.19		0.04
0.791	0.79			
0.892			-.02	
0.993	0.50			
1.094			0.02	
1.195	0.43			
1.295			0.06	
1.396	0.40			
1.497			0.08	
1.598	0.37			
1.699			0.06	
1.799	0.34			
1.900			0.05	
2.001	0.31			
2.102			0.04	

CASE 22: Re=52,100 M=0.89
no grid $T_{\infty}=22.5^{\circ}\text{C}$ $T_s=79.5^{\circ}\text{C}$;

x/D	D	C/E	B/F	A/G
0.000		0.08		
0.087	0.08		0.04	
0.175		-.09		0.07
0.264			0.06	
0.352		0.02		0.05
0.440	0.68		0.04	
0.527		0.11		0.03
0.615	0.70		0.03	
0.703		0.19		0.04
0.791	0.69			
0.892			-.03	
0.993	0.44			
1.094			0.03	
1.195	0.39			
1.295			0.06	
1.396	0.37			
1.497			0.08	
1.598	0.34			
1.699			0.07	
1.799	0.32			
1.900			0.05	
2.001	0.29			
2.102			0.05	

CASE 23: Re=52,100 M=1.00
no grid $T_{\infty}=22.5^{\circ}\text{C}$ $T_s=82.3^{\circ}\text{C}$;

x/D	D	C/E	B/F	A/G
0.000		0.08		
0.087	0.08		0.04	
0.175		-.03		0.07
0.264			0.07	
0.352		0.04		0.05
0.440	0.59		0.04	
0.527		0.11		0.03
0.615	0.62		0.04	
0.703		0.17		0.05
0.791	0.62			
0.892			-.03	
0.993	0.40			
1.094			0.03	
1.195	0.37			
1.295			0.06	
1.396	0.35			
1.497			0.08	
1.598	0.32			
1.699			0.07	
1.799	0.30			
1.900			0.05	
2.001	0.28			
2.102			0.05	

Table 9: Local film cooling effectiveness on the external surface of the model blade:
Cases 20 to 23

CASE 24: Re=52,100 M=1.10
no grid T_w=22.1°C Ts=82.2°C;

x/D	D	C/E	B/F	A/G
0.000		0.07		
0.087	0.09		0.04	
0.175		0.01		0.06
0.264			0.07	
0.352		0.06		0.05
0.440	0.52		0.04	
0.527		0.10		0.03
0.615	0.54		0.04	
0.703		0.16		0.05
0.791	0.55			
0.892				-.03
0.993	0.36			
1.094				0.03
1.195	0.34			
1.295				0.06
1.396	0.32			
1.497				0.08
1.598	0.30			
1.699				0.06
1.799	0.28			
1.900				0.05
2.001	0.26			
2.102				0.05

CASE 25: Re=52,100 M=1.20
no grid T_w=22.3°C Ts=81.8°C;

x/D	D	C/E	B/F	A/G
0.000		0.08		
0.087	0.09		0.04	
0.175		0.05		0.07
0.264			0.07	
0.352		0.08		0.05
0.440	0.45		0.04	
0.527		0.10		0.03
0.615	0.46		0.04	
0.703		0.15		0.05
0.791	0.48			
0.892				-.03
0.993	0.32			
1.094				0.03
1.195	0.31			
1.295				0.06
1.396	0.29			
1.497				0.08
1.598	0.28			
1.699				0.06
1.799	0.26			
1.900				0.05
2.001	0.24			
2.102				0.05

CASE 26: Re=52,100 M=1.29
no grid T_w=22.6°C Ts=81.5°C;

x/D	D	C/E	B/F	A/G
0.000		0.08		
0.087	0.09		0.04	
0.175		0.08		0.06
0.264			0.07	
0.352		0.10		0.05
0.440	0.40		0.04	
0.527		0.09		0.03
0.615	0.39		0.04	
0.703		0.13		0.05
0.791	0.41			
0.892				-.03
0.993	0.27			
1.094				0.03
1.195	0.28			
1.295				0.06
1.396	0.27			
1.497				0.08
1.598	0.25			
1.699				0.06
1.799	0.23			
1.900				0.05
2.001	0.22			
2.102				0.05

CASE 27: Re=52,100 M=1.47
no grid T_w=22.9°C Ts=82.6°C;

x/D	D	C/E	B/F	A/G
0.000		0.08		
0.087	0.10		0.04	
0.175		0.14		0.07
0.264			0.07	
0.352		0.14		0.05
0.440	0.31		0.04	
0.527		0.08		0.04
0.615	0.27		0.04	
0.703		0.10		0.05
0.791	0.28			
0.892				-.02
0.993	0.19			
1.094				0.04
1.195	0.21			
1.295				0.06
1.396	0.21			
1.497				0.08
1.598	0.20			
1.699				0.06
1.799	0.19			
1.900				0.05
2.001	0.18			
2.102				0.05

Table 10: Local film cooling effectiveness on the external surface of the model blade:

Cases 24 to 27

CASE 28: Re=39,200 M=0.67
Grid 2 T ∞ =22.6°C Ts=76.3°C;

x/D	D	C/E	B/F	A/G
0.000		0.07		
0.087	0.08		0.05	
0.175		-0.06		0.07
0.264			0.07	
0.352		0.07		0.06
0.440	0.59		0.03	
0.527		0.17		0.04
0.615	0.56		0.04	
0.703		0.21		0.04
0.791	0.48			
0.892			0.07	
0.993	0.32			
1.094			0.07	
1.195	0.28			
1.295			0.10	
1.396	0.25			
1.497			0.13	
1.598	0.22			
1.699			0.11	
1.799	0.19			
1.900			0.10	
2.001	0.16			
2.102			0.09	

CASE 29: Re=39,200 M=0.98
Grid 2 T ∞ =22.8°C Ts=79.3°C;

x/D	D	C/E	B/F	A/G
0.000		0.07		
0.087	0.09		0.04	
0.175		0.05		0.07
0.264			0.07	
0.352		0.12		0.05
0.440	0.42		0.04	
0.527		0.14		0.04
0.615	0.38		0.04	
0.703		0.17		0.04
0.791	0.35			
0.892				0.06
0.993	0.24			
1.094				0.06
1.195	0.23			
1.295				0.09
1.396	0.21			
1.497				0.12
1.598	0.19			
1.699				0.11
1.799	0.17			
1.900				0.09
2.001	0.15			
2.102				0.08

CASE 30: Re=39,200 M=1.30
Grid 2 T ∞ =22.7°C Ts=82.2°C;

x/D	D	C/E	B/F	A/G
0.000		0.08		
0.087	0.10		0.04	
0.175		0.14		0.07
0.264			0.07	
0.352		0.16		0.05
0.440	0.29		0.04	
0.527		0.11		0.03
0.615	0.24		0.05	
0.703		0.13		0.04
0.791	0.23			
0.892			0.05	
0.993	0.17			
1.094			0.06	
1.195	0.17			
1.295			0.08	
1.396	0.16			
1.497			0.11	
1.598	0.15			
1.699			0.09	
1.799	0.13			
1.900			0.07	
2.001	0.12			
2.102			0.06	

CASE 31: Re=39,200 M=1.44
Grid 2 T ∞ =22.8°C Ts=80.9°C;

x/D	D	C/E	B/F	A/G
0.000		0.08		
0.087	0.10		0.04	
0.175		0.16		0.07
0.264			0.07	
0.352		0.17		0.05
0.440	0.25		0.04	
0.527		0.10		0.03
0.615	0.19		0.05	
0.703		0.11		0.04
0.791	0.18			
0.892				0.05
0.993	0.14			
1.094				0.05
1.195	0.14			
1.295				0.07
1.396	0.14			
1.497				0.10
1.598	0.13			
1.699				0.08
1.799	0.12			
1.900				0.06
2.001	0.11			
2.102				0.06

Table 11: Local film cooling effectiveness on the external surface of the model blade:

Cases 28 to 31

CASE 32: Re=39,200 M=1.57
 Grid 2 T_w=22.9°C Ts=78.3°C;

x/D	D	C/E	B/F	A/G
0.000		0.08		
0.087	0.11		0.04	
0.175		0.18		0.07
0.264			0.07	
0.352		0.17		0.05
0.440	0.22		0.04	
0.527		0.09		0.03
0.615	0.16		0.05	
0.703		0.09		0.04
0.791	0.15			
0.892				0.05
0.993	0.12			
1.094				0.05
1.195	0.13			
1.295				0.07
1.396	0.12			
1.497				0.10
1.598	0.12			
1.699				0.08
1.799	0.10			
1.900				0.06
2.001	0.10			
2.102				0.06

CASE 33: Re=39,200 M=1.68
 Grid 2 T_w=23.1°C Ts=81.4°C;

x/D	D	C/E	B/F	A/G
0.000		0.08		
0.087	0.11		0.04	
0.175		0.20		0.07
0.264			0.07	
0.352		0.19		0.05
0.440	0.20		0.04	
0.527		0.08		0.03
0.615	0.13		0.05	
0.703		0.08		0.04
0.791	0.13			
0.892				0.05
0.993	0.10			
1.094				0.05
1.195	0.11			
1.295				0.07
1.396	0.11			
1.497				0.09
1.598	0.10			
1.699				0.07
1.799	0.09			
1.900				0.05
2.001	0.09			
2.102				0.05

CASE 34: Re=39,200 M=1.94
 Grid 2 T_w=23.5°C Ts=82.6°C;

x/D	D	C/E	B/F	A/G
0.000		0.08		
0.087	0.11		0.05	
0.175		0.23		0.07
0.264			0.07	
0.352		0.20		0.05
0.440	0.16		0.04	
0.527		0.08		0.03
0.615	0.09		0.05	
0.703		0.07		0.04
0.791	0.09			
0.892				0.04
0.993	0.07			
1.094				0.05
1.195	0.09			
1.295				0.07
1.396	0.09			
1.497				0.09
1.598	0.09			
1.699				0.07
1.799	0.08			
1.900				0.05
2.001	0.08			
2.102				0.05

Table 12: Local film cooling effectiveness on the external surface of the model blade:

Cases 32 to 34